TÉCNICO LISBOA

Motion compensation in high frame rate contrast enhanced ultrasound imaging

João Miguel Gomes Ribeiro

Thesis to obtain the Master of Science Degree in

Biomedical Engineering

Supervisors: Prof. Meng-Xing Tang
Prof. Rita Homem de Gouveia Constanzo Nunes

Examination Committee

Chairperson: Prof. João Miguel Raposo Sanches
Supervisor: Prof. Rita Homem de Gouveia Constanzo Nunes
Member of the Committee: Prof. Raquel Cruz Conceição

December 2020

Preface

The work presented in this thesis was performed at the Ultrasound Lab for Imaging and Sensing (ULIS) of Imperial College London (London, United Kingdom), during the period February-December 2020, under the supervision of Professor Mengxing Tang and Professor Rita Nunes.

Declaration

I declare that this document is an original work of my own authorship and that it fulfils all the requirements of the Code of Conduct and Good Practices of the Universidade de Lisboa.

Acknowledgments

First and foremost, I would like to acknowledge Professor Mengxing and Matthieu for the support, guidance and knowledge they provided during the research project which culminated in this thesis.

I would also like to show my appreciation toward the entirety of the ULIS group for welcoming me among them, and for always providing valuable suggestions to guide my work.

In addition, I would like to acknowledge my supervisor Professor Rita Nunes for always being available to help with anything I needed and for providing precious feedback regarding the writing of this thesis.

Finally, I would like to acknowledge my family and closest friends for always supporting me, and for being a constant source of motivation and inspiration.

Resumo

Imagiologia com ultrassons com elevada resolução temporal usando somas coerentes de transmissões não focadas adquiridas em diferentes ângulos permite adquirir imagens de qualidade muito superior e muito mais rapidamente do que usando métodos convencionais. Usando microbolhas como agentes de contraste e transmissões codificadas (como PI ou AM), esta metodologia pode ser utilizada para visualizar vasos sanguíneos e o coração e respetiva dinâmica de fluídos com alto contraste. Porém, o método de somas coerentes é muito suscetível a artefactos de movimento. Apesar de métodos de compensação de movimento já terem sido desenvolvidos e integrados com somas coerentes, ainda não foi desenvolvido um método de compensação de movimento específico para ultrassons com agentes de contraste usando a mesmo metodologia. Neste contexto, um método de compensação de movimento baseado em Doppler foi investigado com o propósito de o otimizar para ultrassons com agentes de contraste de alto *frame rate*. Duas sequências de transmissão incorporadas com PI/AM foram investigadas: aquisição anfulada com contraste de múltiplos impulsos, que consiste na aquisição dos impulsos de transmissão codificada sempre segundo o mesmo ângulo, e aquisição com contraste alternado, onde a transmissão codificada é integrada diretamente na sequência de ângulos de transmissão. Foram desenvolvidos métodos para compensar movimento para cada uma das sequências de transmissão propostas para determinar o método ótimo para compensar movimento quando utlizando o modo de contraste.

Palavras-chave: ultrassons de elevada resolução temporal, compensação de movimento, imagiologia com agentes de contraste, somas coerentes, sequências de transmissão

Abstract

High frame rate ultrasound imaging using coherent compounding of unfocused transmissions acquired at different angles has been shown to greatly improve image quality and frame rate when compared to conventional methods. By using microbubble contrast agents and coded transmissions (such as PI or AM), this technique can be used to image blood vessels and the heart and its flow dynamics. However, the coherent compounding method suffers greatly from motion artefacts. While motion compensation methods have been developed and successfully integrated with coherent compounding, a motion compensation scheme specific for contrast enhanced ultrasound imaging has not yet been developed. Within this scope, this work investigated a Doppler-based motion compensation scheme with the purpose of optimizing it for high frame rate contrast enhanced ultrasound imaging. Two distinct transmit sequences were investigated and incorporated with PI/AM: angled multipulse contrast, where all coded transmission pulses are acquired at the same angle, and alternated contrast, where the coded transmission is integrated directly in the angle sequence. Motion compensation schemes were developed for both types of transmission sequences to determine the optimal method to compensate motion in contrast mode.

Keywords: high frame rate ultrasound, motion compensation, contrast imaging, coherent compounding, transmission sequences

Contents

List of Figures

Nomenclature

Acronyms

AM	Amplitude Modulation
CANR	Contrast-to-Acoustic-Noise Ratio
CEUS	Contrast Enhanced Ultrasound Imaging
CNR	Contrast-to-Noise Ratio
CTR	Contrast-to-Tissue Ratio
FOV	Field of View
GPU	Graphics Processing Unit
HFR	High Frame Rate
HRI	High Resolution Image
LRI	Low Resolution Image
MI	Mechanical Index
MoCo	Motion Compensation
PBRT	Point-Based Registration Technique
PI	Pulse Inversion
PSF	Point-Spread Function
SNR	Signal-to-Noise Ratio
TDI	Tissue Doppler Imaging
US	Ultrasound

Greek symbols

α	Unfocused wave tilt angle.
β	Coefficient of nonlinearity.

ω Angular frequency.

ϕ Phase of wave.

ρ Density.

σ Normalized distance nonlinearity parameter.

τ Time delay.

θ Wave angular width.

Roman symbols

c Speed of sound.

f Frequency.

p Pressure.

u Displacement.

v Velocity.

x Lateral direction.

Z Acosutic impedance.

z Depth direction.

Chapter 1

Introduction

1.1 Motivation

Ultrasound (US) imaging is a noninvasive, easily portable, and relatively inexpensive diagnostic modality which finds extensive use in the clinic [1]. Operating typically at frequencies between 1 and 10 MHz, it produces images via the backscattering of mechanical energy - sound - from boundaries between tissues and from small structures within tissue.

Conventionally, images in US are acquired "line-by-line" by transmitting a narrow focused beam per image line. Using this conventional method, ultrasound has the capability of real-time imaging at up to 30 frames per second. There are many phenomenons in the human body that benefit from being imaged in real-time and for which frame rates at the order of 30 frames per second is insufficient. One such example is the heart, where the imaging of contractions and blood flows are greatly benefited by increasing the temporal resolution, while the very fast opening and closing of the mitral leaflets is simply not possible to observe using such low frame rates.

Nowadays, there exist methods to acquire US images at the order of up 10 000 frames per second by using unfocused transmissions as opposed to focused ones. These high frame rate (HFR) methods rely on coherent compounding of multiple transmissions acquired in slightly different directions to achieve sufficiently high signal-to-noise ratio (SNR) [2, 3]. Apart from the massive increase in frame rate, image quality in coherent compounding US imaging is in many aspects better than conventional US.

The one disadvantage of compounding to improve image quality is that it requires that the locations of the scatterers present in the imaged medium remain static during acquisition. Whenever that is not the case, significant motion artefacts are observed [4].

Motion compensation (MoCo) is often employed in HFR US imaging to eliminate motion artefacts, especially in echocardiography, where large motions are observed [5].

Despite the improved image quality obtained in HFR US imaging, there are many situations in which coherent compounding is not enough to achieve sufficiently high signal of the imaged medium. That occurs more notably in the presence of small blood vessels since erythrocytes are weak ultrasound scatterers and their signal is masked by the surrounding tissue signal [6]. To improve the level of signal

from blood flows, gas-filled microbubble contrast agents are often used. The scattering cross-section of microbubbles is extremely high due to the gas-liquid boundary. Additionally, scattering through microbubbles is largely nonlinear and thus these produce high harmonic content [7], contrary to tissue which produces mostly linear signal.

Contrast-enhanced ultrasound imaging (CEUS) with microbubbles is commonly combined with multipulse methods. The purpose of multipulse methods is to subtract consecutive transmissions, eliminating the linear tissue signal while retaining the nonlinear microbubble signal. Pulse Inversion (PI) and Amplitude Modulation (AM) are the most widely used multipulse coded transmission sequences in ultrasound imaging and both provide high-contrast images of blood vessels.

CEUS has been integrated with coherent compounding to achieve HFR high-contrast images [8, 9]. However, research on the optimal way of integrating coded transmission with coherent compounding is lacking. Furthermore, motion compensation schemes specific for HFR CEUS are extremely under investigated.

Motion compensation in ultrasound imaging can be subdivided in two major classes: Doppler methods and image registration methods. The latter have been previously investigated in HFR CEUS with generally positive results [5, 10]. Doppler-based methods, despite being quite developed for general HFR imaging, are yet to be optimized for HFR CEUS.

1.2 Objectives

This dissertation intends to investigate Doppler-based motion compensation schemes in HFR CEUS using coded transmission - PI and AM. The main objective is to adapt the Doppler autocorrelator approach developed for HFR imaging [11] to CEUS in both PI and AM sequences, as well as optimizing the pulse sequences in terms of the accuracy of the motion compensation method.

As an initial evaluation of Doppler motion compensation methods in HFR CEUS, developing a framework where the results are reproducible and the ground truths are known is key. With that in mind, a study fully on simulation data was developed. The findings on simulation data, for which the parameters of the medium and the acquisition are known fully, are able to be translated to real acquisitions, taking potential limitations into account.

1.3 Thesis Outline

The dissertation is organized as follows:

- Chapter 2 (Background) provides an overview of the history of high frame rate US imaging, the main theoretical concepts underlying the framwork of the dissertation and a review of the state of the art of motion compensation methods;
- Chapter 3 (Methods) first summarizes the simulation framework that was used and then goes into detail on coded transmission, beamforming and Doppler motion compensation. Finally, the

evaluation metrics to asses the work are presented;

- Chapter 4 (Results) presents the ultrasound simulation results after motion compensation as well as their static and uncompensated versions, which serve as positive and negative controls, respectively. The evaluation metrics are then presented in a comparative manner;
- Chapter 5 (Discussion) discusses the results presented in the prior chapter and compares them with the existing literature on motion compensation;
- Chapter 6 (Conclusions) summarizes the main conclusions gathered from the results and outlines possible paths that can be followed to further improve the studied motion compensation methods as well as validating them.

Chapter 2

Background

The foundations of echolocation, which later enabled ultrasound imaging, can be traced back to the sinking of the Titanic in 1912. It became clear that detecting underwater objects was a necessity for overseas navigation. However, by that time, the technology necessary for echo-location had not been developed yet. It wasn't until the end of World War I that the first echolocation systems were realized. They were enabled by the usage of piezoelectric materials to both transmit sounds of very high frequencies and receive their echoes. Computing the time between the transmission and reception of these sounds made it possible to locate objects underwater. This technology was named Sonar (Sound Navigation and Ranging), and the sounds of very high frequencies ranging from a few to several Megahertz that were frequently used for this purpose were named *ultrasounds*.

Continuous-wave Sonar systems became useful to locate submarines during World War I. But it wasn't until World War II that pulsed-echo ranging applied to electromagnetic waves became radar (radio detection and ranging). Pulsed-echo, as opposed to continuous echo, was later realized in Sonar too. Antenna and beamforming theory later highlighted the benefits of using arrays, rather than single-crystals to transmit and receive pulses. And after World War II, with sonar and radar as models, clinicians and researchers saw the possibilities of using pulse-echo techniques to probe the human body for medical purposes.

In the 1950s, the first ultrasound imaging modes were developed. By the 1960s, B-mode scanners had been realized. In the 1970s, linear and phased-array ultrasound transducers enabled real-time imaging. From there, the first commercial systems were developed, and several technologies emerged from it such as pulsed-wave Doppler and colour flow imaging. In the 1990s, digital systems were first developed, and by the 2000s handheld arrays for real-time 2D and 3D imaging had already been fully implemented, as well as harmonic and contrast imaging.

During the late 2000s and the early 2010s, it became clear that increasing the frame-rate in real-time systems was necessary, and from there high frame rate and ultra-high frame rate systems were investigated.

This chapter begins with a mathematical description of acoustic wave linear propagation and scattering. We then advance to formulate non-linear scattering mathematically. After the description of the

physics principles, the conventional line-by-line ultrasonography pipeline using phased array transducers is summarized. The history and percursors of high frame rate imaging are then reviewed until the genesis of ultrafast imaging with coherent compounding, where motion estimation and compensation becomes key. Degradation due to motion in high frame rate imaging is illustrated through a simple example and then methods for motion artefacts correction in ultrafast imaging are reviewed. Finally, ultrasound imaging with contrast agents is reviewed.

2.1 Physics of acoustic waves

Acoustic waves, also named sound or pressure waves are the information carriers in ultrasound imaging. The amplitude, frequency and phase of the waves, as well as how they change in time contain all the necessary information to reconstruct an image in ultrasonography.

Sound waves are of the longitudinal type, meaning that they create a sinusoidal back-and-forth motion of particles as they travel along in their direction of propagation. Given an initial propagation of a physical medium, sound waves propagate by transferring energy by collision to neighbouring particles in the direction of propagation. As molecules transfer energy to other neighbouring molecules, the former experience a velocity decrease. This leads to zones of rarefaction - low density of medium particles - and compression - high density of medium particles - as illustrated by Figure 2.1.

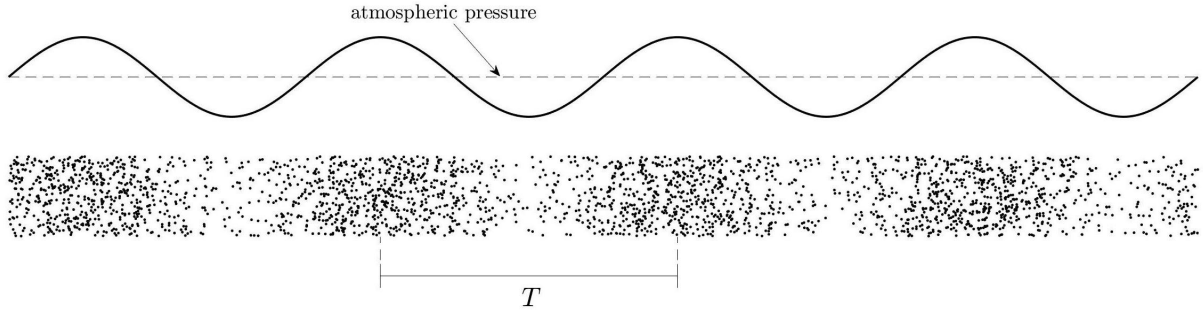

Figure 2.1: Analogy between a transverse wave and a longitudinal pressure wave in a gas.

The amplitude of a longitudinal pressure wave is regarded as the difference in density between the zones of highest compression and lowest rarefaction. The period T is defined as the time difference between two consecutive maximum compression or minimum rarefaction zones. All other properties of waves, such as frequency and phase, can also be determined using time relationships between compression and/or rarefaction zones.

An acoustic wave is a function of time and space, $p = p(t, \mathbf{x})$. For an acoustic wave to be physically realisable, it must abide by the wave equation. The wave equation, which is a partial differential equation, is presented in equation 2.1 in Cartesian coordinates:

$$\nabla^2\phi - \frac{1}{c_0^2}\frac{\partial^2\phi}{\partial t^2} = 0 \tag{2.1}$$

where c_0 is the speed of sound and ϕ is a velocity potential. That is, the velocity of the acoustic wave is

given by:

$$v = \nabla\phi \tag{2.2}$$

When defined like this, the pressure field can also be given in terms of this velocity potential [12]:

$$p = -\rho\frac{\partial\phi}{\partial t} \tag{2.3}$$

where ρ is the density of the medium where the wave propagates. It is possible to prove that a pressure field given by equation 2.3 also solves the wave equation (2.1). The proof can be found in Appendix A.1.

Using pressure fields to describe interactions of ultrasounds and their propagation mediums is more straightforward than using their corresponding velocity potentials.

2.1.1 Wave propagation

Wave propagation can be fully understood by setting different initial conditions and boundary conditions in the wave equation to discover specific solutions.

The general solution to the wave equation is a complex exponential oscillating on both time and space. For the one-dimensional case, the pressure and velocity of the wave can be written in the following way:

$$\begin{aligned} p(t,z) &= p_0 e^{j(\omega t - kz)} \\ v(t,z) &= v_0 e^{j(\omega t - kz)} \end{aligned} \tag{2.4}$$

where p_0 is the pressure at equilibrium, ω is the angular frequency of the wave and $k = \omega/c_0$ is the wave number. An identity which relates velocity and pressure can be found by making use of the velocity potential since both quantities are related to it through equations 2.2 and 2.3, respectively. By combining these two, a new equation can be written that directly translates velocity into pressure. That relation, in 1D, is:

$$\frac{\partial v}{\partial t} = -\frac{1}{\rho_0}\frac{\partial p}{\partial z} \tag{2.5}$$

Substituting p and v by the corresponding general solutions in 2.4, we obtain:

$$\begin{aligned} \frac{\partial v(t,z)}{\partial t} &= -\frac{1}{\rho_0}\frac{\partial p(t,z)}{\partial z} \\ j\omega v_0 e^{j(\omega t - kz)} &= \frac{jk}{\rho_0} p_0 e^{j(\omega t - kz)} \\ j\omega v(t,z) &= \frac{j\omega}{c_0\rho_0} p(t,z) \\ \frac{p}{v} &= \rho_0 c_0 \end{aligned} \tag{2.6}$$

The last ratio of pressure and velocity is named the acoustic impedance, and is normally written as:

$$Z = \frac{p}{v} = \rho_0 c_0 \tag{2.7}$$

The acoustic impedance is oftentimes sufficient knowledge to fully characterize ultrasound propagation in heterogeneous mediums. Notice that the velocity in equation 2.7 can be negative, indicating that it is propagating in the opposite direction of our reference frame. The sign of the acoustic impedance, Z, is thus dependant on the direction of propagation.

To illustrate how ultrasound propagation between mediums with different acoustic impedances affects reflection and transmission, consider a one-dimensional plane wave traveling from a medium with acoustic impedance $Z_1 = \rho_1 c_1$ through a boundary ($z = 0$) to a second medium with acoustic impedance $Z_2 = \rho_2 c_2$. If the incident wave has amplitude p_0, then the reflected and transmitted waves' amplitudes will be a fraction of p_0. The reflection and transmission factors are R and T, respectively. The equations for the incident, reflected and transmitted pressure waves are presented in the next equation as p_i, p_r and p_t, respectively:

$$\begin{aligned} p_i &= p_0 e^{j(\omega t - k_1 z)} \\ p_r &= R p_0 e^{j(\omega t + k_1 z)} \\ p_t &= T p_0 e^{j(\omega t - k_2 z)} \end{aligned} \tag{2.8}$$

and for the velocities, using $v = p/Z$:

$$\begin{aligned} v_i &= \frac{p_0}{Z_1} e^{j(\omega t - k_1 z)} \\ v_r &= -\frac{R p_0}{Z_1} e^{j(\omega t + k_1 z)} \\ v_t &= \frac{T p_0}{Z_2} e^{j(\omega t - k_2 z)} \end{aligned} \tag{2.9}$$

Notice that the sign of the reflected wave is the inverse of the incident wave, as they are propagating in opposite directions. At the boundary, to ensure continuity, the pressures in both mediums must be the same. Since the incident and reflected wave are propagating in the first medium and the transmitted wave in the second one, the relation is:

$$\begin{aligned} p_i(z=0) + p_r(z=0) &= p_t(z=0) \\ p_0 e^{j\omega t} + R p_0 e^{j\omega t} &= T p_0 e^{j\omega t} \\ 1 + R &= T \end{aligned} \tag{2.10}$$

and for the velocities:

$$\begin{aligned} v_i(z=0) + v_r(z=0) &= v_t(z=0) \\ \frac{p_0}{Z_1} e^{j\omega t} - \frac{R p_0}{Z_1} e^{j\omega t} &= \frac{T p_0}{z_2} e^{j\omega t} \\ \frac{1}{Z_1} - \frac{R}{Z_1} &= \frac{T}{Z_2} \end{aligned} \tag{2.11}$$

Relations 2.10 and 2.11 can be solved for the reflection and transmission factors. After some algebra,

those yield:

$$R = \frac{Z_2 - Z_1}{Z_2 + Z_1} \tag{2.12}$$

$$T = \frac{2Z_2}{Z_2 + Z_1} \tag{2.13}$$

We see that reflection of ultrasound is largest when the acoustic impedances between the mediums are largely different, and is null when $Z_2 = Z_1$. This means that in order to have reflections, the mediums must have heterogeneities in terms of acoustic impedances. This is crucial for ultrasound imaging, since images are reconstructed using the backscattered echoes from the emitted waves. The analysis was carried out for a plane wave in 1D but similar relations can be determined for all types of waves and boundaries in 3D. More factors play a role in the most complex 3D situations. However, acoustic impedance is still the main factor affecting the reflection and transmission factors.

2.1.2 Nonlinear acoustics

When a medium with certain density, ρ is insonified with an acoustic pressure wave, p the linear equation of state that describes how the pressure and density of the medium change, in adiabatic conditions - absence of heat transfer - is given by [12]:

$$p - p_0 = A\left(\frac{\rho - \rho_0}{\rho_0}\right) \tag{2.14}$$

Where p_0 and ρ_0 are the pressure and density at equilibrium in a fluid. The constant A is the proportionality constant taken for $\rho = \rho_0$ and at a specific entropy is given by:

$$A = \left[\rho_0 \left(\frac{\partial p}{\partial \rho}\right)_{S,\rho=\rho_0}\right] = \rho_0 c_0^2 \tag{2.15}$$

A better approximation is to include the next terms in a Taylor expansion series for the pressure as a function of density [13]:

$$p - p_0 = A\left(\frac{\rho - \rho_0}{\rho_0}\right) + \frac{B}{2}\left(\frac{\rho - \rho_0}{\rho_0}\right)^2 + ... \tag{2.16}$$

Where B is defined in the same way as A:

$$B = \left[\rho_0^2 \left(\frac{\partial^2 p}{\partial \rho^2}\right)_{S,\rho=\rho_0}\right] \tag{2.17}$$

A simple measure of the nonlinearity of a medium is the ratio B/A. The larger the ratio, the larger the nonlinear effects in the scattered echoes. Another way to quantify the nonlinearity of the medium is by using the nonlinear coefficient, written as:

$$\beta = 1 + \frac{B}{2A} \tag{2.18}$$

But what exactly are these nonlinear effects? The three major consequences of nonlinearity are:

1. Cumulative pulse distortion;
2. Harmonic generation;
3. Saturation.

All of these consequences arise from the quadratic dependence of pressure on density. For a one-dimensional sinusoidal plane wave in a lossless medium, the speed of sound for a displacement amplitude u is given by:

$$\frac{\mathrm{d}z}{\mathrm{d}t} = c_0 + \beta u \tag{2.19}$$

The previous equation states that positive half cycles are sped up by a factor of βu and negative half cycles slow down by the same factor. The wave begins to distort into a "sawtooth" shape because of this effect. As the wave propagates, the more distorted it will become, verifying the cumulative pulse distortion. Figure 2.2 illustrates the distortion an initially sinusoidal wave suffers due to propagation in a nonlinear medium.

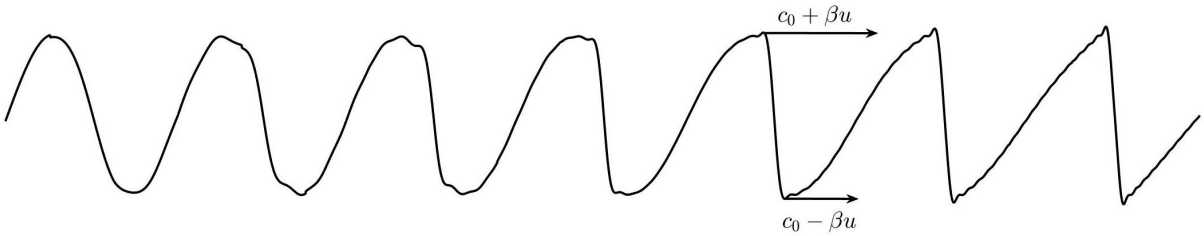

Figure 2.2: Distortion of an acoustic sine wave as it propagates through a nonlinear medium. The compressional zones propagate faster than the rarefactional ones, creating a sawtooth shape.

The sawtooth waveform can be decomposed into its harmonics using Fourier series. The harmonics composing the sawtooth waveform reduce in amplitude with a factor of $1/n$, where n is the integer corresponding to the n^{th} harmonic frequency. Harmonic generation is thus verified. The full equation of the generated harmonics is presented next [12]:

$$p\left(z,t\right) = p_0 \sum_{n=1}^{\infty} \frac{2}{n\left(1+\sigma\right)} \sin\left(n\omega\left(t - z/c_0\right)\right) \tag{2.20}$$

Where z is the direction of propagation, $\omega = 2\pi f$ is the angular frequency and σ is the normalized distance nonlinearity parameter. The latter constant is useful in predicting distortion as the wave propagates. For a plane wave, this constant is given by:

$$\sigma\left(z\right) = \frac{\beta p_0 2\pi f z}{\rho_0 c_0^3} \tag{2.21}$$

For example, when $\sigma = 1$ shock formation[1] ensues and when $\sigma = 3$ the sawtooth begins [14]. The distance, z, where these phenomena occur can be determined from the previous equation.

[1] A wave is said to have reached shock formation when the distance between the positive peaks and the negative peaks is zero. In other words, the slope of the line that crosses zero is infinite.

The third major effect is saturation, which refers to how proportionality between the transmitted waveform and the corresponding echoes no longer hold in nonlinear mediums. In linear mediums, the amplitude of the echo produced from backscattering is always proportional to the emitted sound, no matter how high the pressure amplitude of the initial sound is. This linear relationship is lost in nonlinear mediums, and the amplitude of the echo is smaller than the proportionality constant for linear conditions, reaching a plateau. The maximum pressure amplitude an echo can have is called the saturation pressure, and is given by:

$$p_{sat}(z) = \frac{\pi}{\sigma(z)} p_0 = \frac{\rho_0 c_0^3}{2\beta f z} \tag{2.22}$$

These relations only hold for plane waves in fluids, but similar ones can be determined for other beam shapes in all types of media.

2.2 Conventional ultrasound imaging

Conventional ultrasound imaging, also referred to as line-by-line imaging, is the most used imaging modality in the clinic [1]. Its safety, low cost and the ability of real-time imaging are the greatest advantages of ultrasound imaging when compared to other imaging modalities [15, 16]. The operation of acquiring US images with conventional methods is summarized during this section.

2.2.1 Array transducers

In diagnostic ultrasound imaging, the component that translates information between the body and the imaging system is named a transducer. The word "transducer" is used to name any device that performs transduction, which is a conversion of information of one type to information of another type. In ultrasound imaging, electric signals are converted into acoustic waves, and the backscattered echoes are converted back to electric signals in reception.

The types of material that can transduce electricity into mechanical vibrations to produce sounds and vice-versa are piezoelectric crystals. Piezoelectricity is the hability of certain materials to accumulate charge in response to mechanical stress and vice-versa, making them ideal for ultrasound signal transduction.

In modern systems, several thin piezoelectric crystals called the elements, are used in an array to both transmit and receive the relevant signals. Arrays allow manipulation of focusing of the transmitted pulse in a way that single-crystal transducers coupled with acoustic lens can't achieve. In reception, by acquiring a signal per element and applying the appropriate reconstruction techniques, full images of a field of view (FOV) can be obtained. Figure 2.3 shows a schematic of transducer dimensions.

The pitch is the distance between the center of two piezoelectric crystals and is a quantity that must be known to correctly compute the time delays for beamforming.

Between each of the elements there is an acoustically and electrically isolating material to ensure there is no interference between the signals emitted and received from each element [17].

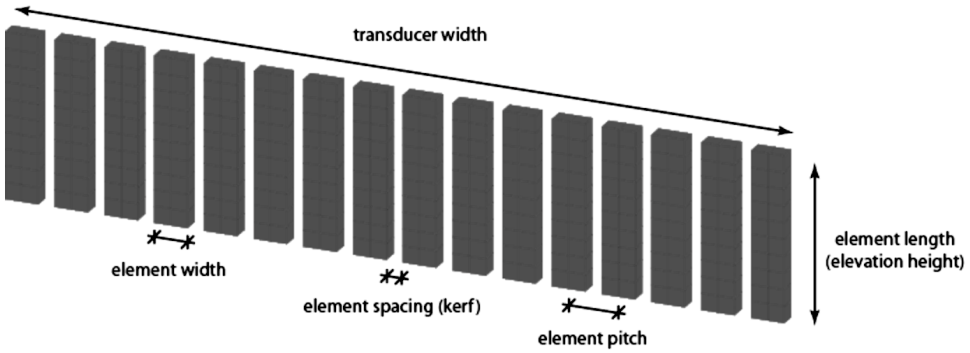

Figure 2.3: Dimensions of array transducer composed of many thin piezoelectric crystals (adapted from Treeby et al., 2016, p.45).

When the transducer array is capable of focusing and steering at any point and direction, they are called phased arrays. Phased arrays are the most commonly used transducers because of their versatility. Thus, they are the only type of transducers that will be analysed in this dissertation.

2.2.2 Image formation

The principal modality in US imaging is Brightness mode or B-mode for short. B-mode using phased-array transducers consists of sequentially transmitting narrow ultrasound beams in the direction of the aperture. These beams are transmitted by exciting the piezoelectric crystals with electric signals with different delays. To scan a line, the array elements are excited and the same ones are active for reception. Figure 2.4 exemplifies the described procedure.

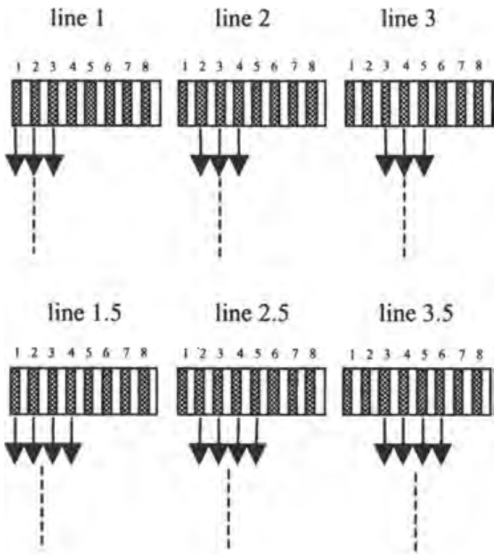

Figure 2.4: Formation of scan-lines by excitation of a few transducer elements in the aperture. The dashed line represents the center of the beam. The least elements used for transmission, the narrower the beam. The number of lines in the image can be almost double the number of array elements (adapted from Webb, 2002, p. 126).

The beams used in conventional US imaging are focused beams, i.e., beams shaped such that the energy of the beam is maximized at a certain depth. The process of shaping the beam is named

beamforming. Each of the elements in the transducer array generates a spherical wave - a wave that propagates equally in all directions. The wavefronts of all the spherical waves sum in space as they propagate, generating a combined acoustic wave field at each point in space and a combined wavefront as it propagates in time. If the combined wavefront converges to a point in depth as it propagates, then the beam is said to be focused.

To focus a beam, different delays must be applied to the input signals fed to the array elements. An example of a focused beam generated with 8 array elements is displayed in Figure 2.5.

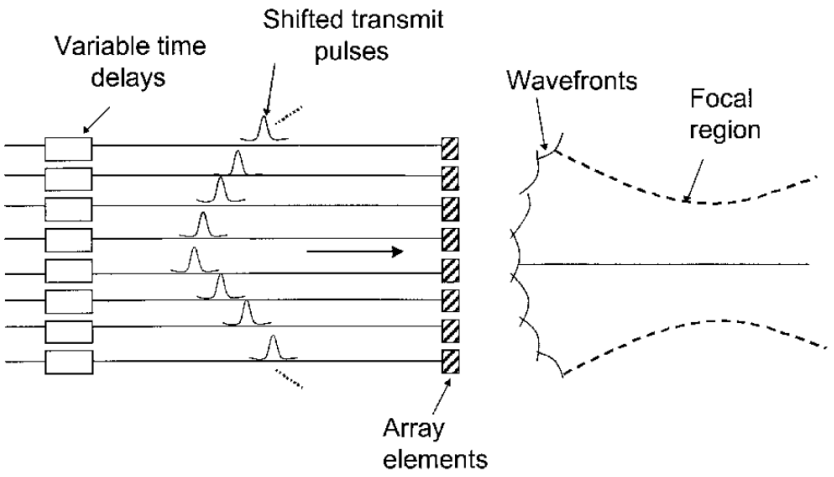

Figure 2.5: Transmit beamforming of a focused beam. Different delays applied to the input signals of the array elements lead to convergence of the ultrasound energy onto a single point in space. The beam diverges from that point onwards, comparatively to how a convex lens focuses an electromagnetic beam (from Szabo, 2004, p. 190).

Additionally, a feature of array transducers of piezoelectric crystals, as opposed to their single-element counterparts, is their ability to electronically steer the beam. Similarly to focusing the beam, steering can be accomplished by applying different time delays to each element. Figure 2.6 exemplifies electronic steering in an array transducer.

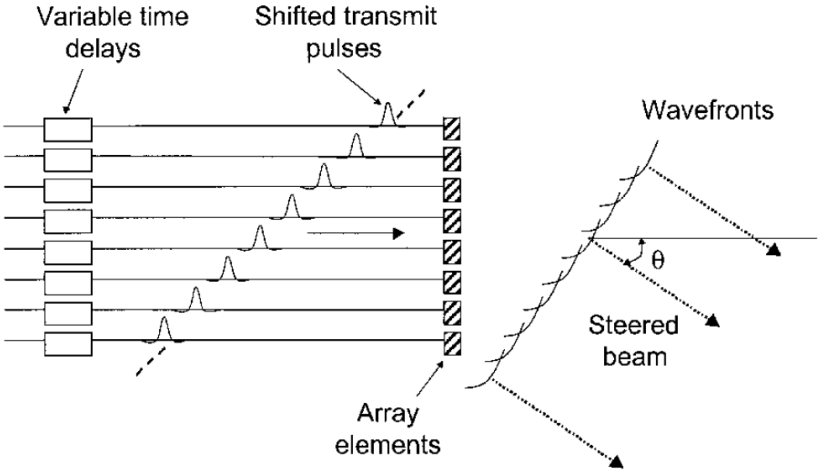

Figure 2.6: Ultrasound beam-steering at an angle θ, accomplished by feeding the elements of the array with electric signals with different time delays (from Szabo, 2004, p. 187).

Finally, steering and focusing can be combined to achieve focusing at any single point in (x, z) space, where x denotes the lateral axis and z denotes the depth axis.

The delays for transmit beamforming can be determined given the positions of the elements in the array and their distance to the focus point. Consider an array of N elements and a Cartesian coordinate system whose origin is located at the center of the first element, the x-axis is parallel to the transducer and the z-axis perpendicular to the transducer. Every single element is considered as a point source. Consider also the focus center, which is the point at which we wish to focus our beam, $P_f = (x_f, z_f)$. Figure 2.7 illustrates this setup.

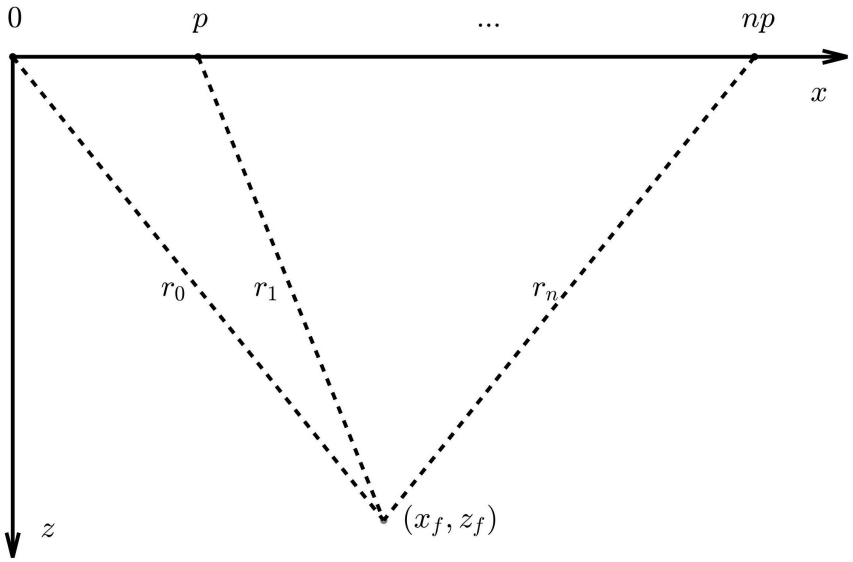

Figure 2.7: Coordinate system for computation of transmit delays. The points in the x-axis represent the centers of each array element, the point of coordinates (x_f, z_f) is the focus center and r_0, r_1 and r_n represent the distances between the first, second and n^{th} elements and the focus center, respectively.

Using this coordinate-system, the position of the n^{th} element is given by $P_n = (np, 0)$, where p denotes the pitch of the transducer, and its distance to the focus center is given by $r_n = \|P_n - P_f\|$, which can also be expanded to be written as:

$$r_n = \sqrt{(np - x_f)^2 + z_f^2} \tag{2.23}$$

Equation 2.23 represents the distance the spherical wave produced by each element must travel before it reaches P_f. The time it takes for sound waves to travel such distance is given by:

$$t_n = \frac{\sqrt{(np - x_f)^2 + z_f^2}}{c_0} \tag{2.24}$$

Where c_0 denotes the speed of sound in the medium in which the waves are propagating. Then, the time delay that must be applied to the RF pulse fed to the n^{th} element, τ_n, such that the wavefronts converge at P_f is the difference in travel times between the closest element to the RF pulse, k, and the n^{th} one:

$$\tau_n = t_n - t_k, \quad k = \arg\min_n \left\{ (np - x_f)^2 \right\} \tag{2.25}$$

The k^{th} element is thus the element whose distance vector to $\mathbf{x_f}$ is the closest to orthogonal with the x-axis, and from equation 2.25 it is the element for which the time delay, τ_k, applied to the RF pulse is null.

By performing several focused transmissions (usually the same number of transducer elements, 64-128) according to Figure 2.4, one ultrasound image focused at a certain depth can be reconstructed. One scan-line is formed from each transmission. Reconstruction of the scan-line consists in delaying and summing the received echoes from each element, in a process named receive-beamforming.

Upon reception by the transducer elements, delays are re-applied to the incoming electric signals (converted from echoes by the piezoelectric crystal elements). These delays account for the differences in reception times of the incoming echoes from the focus center. The receive time delays account for the differences between arrival times of the echoes coming from the focus center to each array element. Since transmit and receive delays fulfill the exact same purpose, these delays are precisely the same ones used for transmit-beamforming given by equations 2.24 and 2.25. After receive-beamforming, the signals are summed to form one scan-line, as illustrated by Figure 2.8.

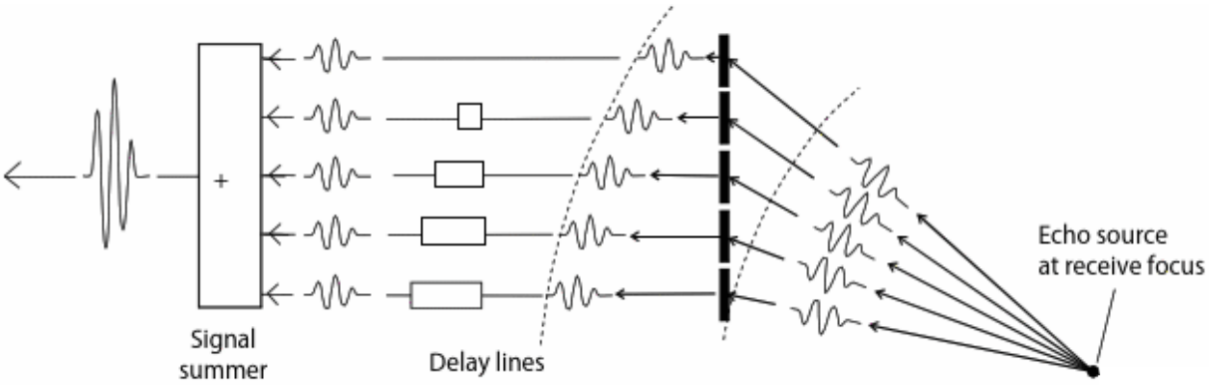

Figure 2.8: Receive-beamforming in phased-array transducer. The received echoes are delayed to account for differences in arrival times and summed to form one scan-line (adapted from Hoskins et al., 2019, p. 56).

Consider x to be the depth at which we wish to image and that our transducer has N elements. With a typical focused beam framework, N transmission and receive events are necessary to form an image. For an image depth of d, the waiting time between each transmission is given by:

$$t_{\text{waiting}} = \frac{2d}{c_0} \tag{2.26}$$

This waiting time is twice the time sound takes to propagate through the field of view: once to cross the full depth, and the same amount of time for echoes to return. If we consider processing time to be negligible compared to the waiting times, the total time it takes to form an ultrasound image using this configuration is given by:

Table 2.1: Frame rates of conventional ultrasound imaging given different imaging depths, number of transducer elements, and number of depths used for focusing.

		Focusing	N_{elements}		
			64	96	128
Imaged depth	5 cm	1 depth	240	160	120
		4 depths	60	40	30
	10 cm	1 depth	120	80	60
		4 depths	30	20	15
	15 cm	1 depth	80	53	40
		4 depths	20	13	10
	20 cm	1 depth	60	40	30
		4 depths	15	10	7

$$t_{\text{total}} = \frac{2d}{c_0} N_{\text{elements}} \tag{2.27}$$

The achieved frame rate is thus the inverse of the previous expression:

$$\text{frame rate} = \frac{1}{N_{\text{elements}}} \frac{c_0}{2d} \tag{2.28}$$

Table 2.1 displays different frame rate values achieved in ultrasound imaging in function of the number of elements and the imaged depth according to equation 2.28. The reference speed of sound used to compute the values in the table was 1540 m/s, which is the speed of sound in soft issue [18]. Frame rate values are displayed in units of Hertz. Up until now, only single depth focusing has been mentioned. In practice, since the resolution is poor at depths that are not the depth of focus, multiple transmissions at different depths are acquired and compounded to produce images of higher resolution at all depths. Images at three or four different depths of focus are acquired and compounded, so the frame rate is reduced by a factor of three or four, respectively. Table 2.1 presents frame rates for both single-depth and multiple-depth focusing - four depths, in this case.

Even when only 64 transducer elements are used and we image at a depth of 10 cm, the maximum achieved frame rate is no larger than 30 Hz. From the Nyquist sampling theorem, any phenomenon whose duration is less than 1/15 seconds = 67 milliseconds cannot be correctly represented by imaging at this frame rate. Elastography and echocardiography are two of the fields that are most limited by the frame rates of conventional ultrasound. While echocardiography is possible in conventional ultrasound, B-mode images are of very poor quality and have very limited uses in terms of characterisation of myocardium contraction and blood flow analysis. Elastography is simply not realizable with conventional ultrasound.

2.3 High frame rate ultrasound imaging

2.3.1 Percursors of high frame rate ultrasound imaging

The idea of increasing the frame rate of sonography to the kilohertz range can be dated back to more than forty years ago. In 1977, Bruneel et al. demonstrated the ability to image at such frame rates by making use of opto-acoustic interactions and optical processing of ultrasonic signals [19]. While the apparatus was unpractical for the clinic, the authors used 20 transducers to image the human heart with sufficiently good image quality. While the display that they used to view the images was limited to 50 Hz refresh rate - it was a television - the apparatus they built enabled the acquisition of videos of up to 1000 frames per second. The authors were the first to use the term "ultrafast" in reference to ultrasound imaging at frame rates in the kilohertz range.

The same group of researchers moved on to a different approach to ultrafast imaging by using analog electronic parallel processing [20]. The term "parallel processing" simply means performing multiple processing tasks at the same time, or *in parallel*. In the field of ultrasound imaging, parallel processing generally refers to parallel receive-beamforming: reconstruction of multiple scan-lines simultaneously, instead of one at a time. The approach devised by Delannoy et al. permitted the acquisition of ultrasound images with 70 lines with a frame rate of 1 kHz. The system they developed had the ultimate goal of imaging the heart at the ultrasonic speed limit. For an imaging depth of 15 cm, this limit is approximately 200 µs, which consequently allows a maximum frame rate of 5 kHz. The technology at the time was not sufficiently developed to image at the rate of the ultrasonic limit, and it wasn't until more than 30 years later that the heart was finally imaged at 5000 frames per second [8].

In 1984, parallel processing for linear phased arrays was developed by Shattuck and Weinshenker [21]. The method, named "Explososcan", permitted the acquisition of four B-mode lines from a single transmitted pulse. The slightly unfocused pulse essentially increased the lateral range of energy deposition, making it possible to reconstruct image lines from points where the energy wasn't as maximum, despite the overall energy of the pulse being the same. The four lines were reconstructed from the echoes of the same transmitted pulse by applying different receive beamforming delays. The receive beamforming delays were chosen such that the focus points were in the lateral direction of the maximum energy point of the slightly unfocused beam. While it would be expected that resolution would be poorer than conventional methods, explososcan's resolution was on-par with existing conventional methods but with four times the frame rate. Since conventional ultrasound consisted in optimizing the receive delays such that the receive focus would match the transmit focus, explosocan was a truly different approach from convention by unfocusing the transmit pulse. Shattuck and Weinshenker envisioned that, at least conceptually, their method could be used to generate all B-mode lines using a single pulse, but also that that would necessitate the insonification of the entire FOV with a single pulse.

Image quality of B-mode US imaging kept improving throughout the 1980s and 1990s with the development of commercial array systems, wideband and specialized transducers and the transition into digital systems. Doppler modes also surfaced in commercial systems with pulsed wave Doppler and colour flow, which saw heavy use in the clinic for blood flow assessment.

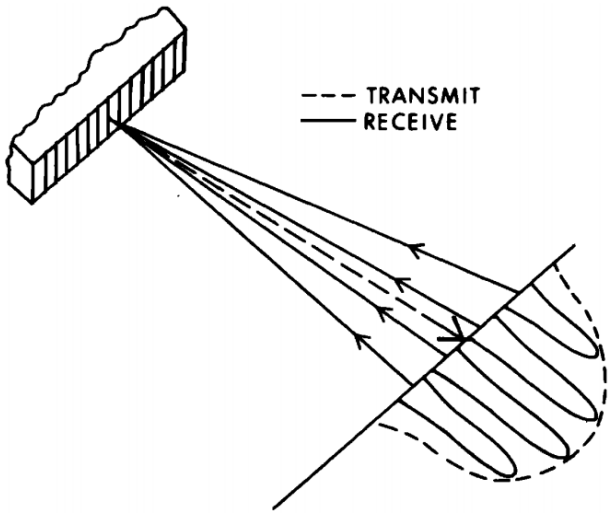

Figure 2.9: The explosocan concept developed by Shattuck and Weinshenker. A slightly unfocused beam (dotted line) is used to generate four scan lines (solid lines) with a single transmission, effectively quadrupling the frame rate (from Shattuck and Weinshenker, 1984, The Journal of the ASoA, 75(4), p. 1274.

It was in the field of ultrasound elastography that the next step in achieving ultrafast imaging was being taken, pioneered by Fink and co-authors. Elastography is an imaging modality that maps the elastic properties and stiffness of soft tissue. Knowing the stiffness or elasticity of certain tissues has great diagnostic potential. For instance, tumour masses in breast tissue can be identified by measuring the velocity of shear wave propagation relatively to the surrounding medium. Tumours are more elastic than soft tissue and thus shear waves propagate faster through them [22]. But the clinical applications of elastography extend far beyond identification of tumour masses [23–25]. Stiffness and elasticity measurements can be performed using ultrasounds by inducing a mechanical perturbation in the form of a shear wave and then measuring the velocity of propagation of said wave through tissues. Because shear waves travel through tissue with velocities of a few meters per second, following the evolution of the displacements induced in the medium on a millimeter scale requires imaging at frame rates on the kilohertz range.

In 1999, with the purpose of achieving this goal, Sandrin et al. transmitted acoustic waves through a phased array transducer with no transmit or receive focusing [26]. The data was instead stored during the acquisition to later perform parallel numerical beamforming. What this allowed was to image at the ultrasonic limit. At an imaging depth of 7.5 cm, they were able to acquire images at a rate of 10 000 frames per second. Because no transmit delays were applied, all elements of the array emitted their pulses at the same time. This leads to all of the emitted wavefronts to add constructively in lines parallel to the aperture. In other words, the transmitted waves were plane waves. This type of transmission was very uncommon at the time because it did not focus at any single point in the imaging medium, so the energy of the wave was spread out through the whole field of view. This results in the backscattered echoes to have lower power as well, reducing the SNR. Nevertheless, the purpose was not to acquire B-mode images, but elastography images. That purpose was fulfilled, as the authors managed to measure axial displacements in tissue-mimicking phantoms congruent with their elasticity and stiffness properties.

Resolution was also comparable with conventional ultrasound.

The same group of researchers expanded on their previous approach in 2002, by estimating both axial and lateral displacements in transient elastography with ultrafast imaging [27]. Their method consisted of transmitting an untitled plane wave using a 128-element array. In reception, the left half of the aperture was beamformed as a slightly tilted plane wave in the clockwise direction, and the right half of the aperture was beamformed as a slightly tilted plane wave in the counter-clockwise direction, effectively generating two images per transmission. The half-apertures are normally called sub-apertures, and the overall method of reconstructing images by dividing the aperture into multiple sub-apertures in reception is called synthetic aperture beamforming, and had been explored before in other ultrasound imaging contexts [28–30]. Lateral displacements were computed from the 1-D cross-correlation between consecutive left and right images and then averaged. The purpose was to reduce the variance of the estimation so as to increase confidence. While the concept of compounding was not new for focused transmissions [31–33], this was the first time compounding of unfocused waves had been proposed.

2.3.2 Ultrafast imaging: coherent compounding

Before the pioneering work of Montaldo et al., the purposes of compounding in US imaging were to cancel out random variations (specifically, speckle), reduce the effects of clutter and shadowing and achieve higher contrast and signal-to-noise ratio [32, 33]. Because this summation was carried out on the intensity images, the terminology "incoherent" compounding was used.

Coherent compounding of multiple acquisitions instead consists in the summation of the RF data directly, guaranteeing that receive-beamforming aligns RF data of each acquisition such the summed points in the image represent the same points in the imaging medium. In other words, the sum is "coherent". This is performed before any other processing is applied, such as envelope detection or log-compression to ensure coherence. Additionally, the original approach by Montaldo et al. used transmissions of tilted plane waves at different angles [2]. Using transmissions at different angles further decorrelates speckle and clutter during compounding, helping improve the signal-to-noise ratio.

Just like in transient elastography, where the same group of researchers had already used plane wave transmissions, the contrast and signal-to-noise ratio are poor when no compounding is performed. Because high-power ultrasounds may have hazardous biological effects when transmitted into the body, low-power transmissions must be used [34]. For plane waves, that power is spread onto a broad sector to insonify the entire field of view in one transmission. That comes with the trade-off of all generated echoes having lower amplitudes than the ones generated from standard focused transmissions. The resulting image is a low-resolution image (LRI) and generally poor contrast-to-noise ratio (CNR). To reduce the power of random noise, multiple coherently compounded LRIs must be used to form a high-resolution image (HRI). Since more than one transmission is necessary to generate one frame, the frame rate is reduced by a factor equal to the number of compounded plane waves. There is then a trade-off between image quality and frame rate. While compounding may initially seem more like a necessity to circumvent a limitation rather than a feature, the improvements in image quality provided by coherent compounding

with unfocused waves far exceed anything achievable with standard focused transmission at a (still) very high frame rate.

The geometry of unfocused wave transmission and dynamic receive-beamforming at different angles inherently makes coherent compounding a superior method for US imaging in terms of focusing. This is because synthetic focusing is achieved laterally and at all depths. This can be illustrated by considering, first, the case of coherently compounding two plane waves. As the first wave propagates through the medium, all points in the FOV will be interrogated by one wave. As the next wave propagates, the same points will be interrogated by the next wave. During coherent compounding, the backscattering contributions of each of the points will sum coherently, effectively combining the power of the backscattered echoes of both transmissions to generate a stronger combined backscattered echo. This is equivalent to doubling the amount of power used in a single transmission. If more waves are used, this effect is multiplied. Because the combined amount of power provided to each point in the FOV is large, this methodology is equivalent to performing one focused transmission per point in the FOV, which would necessitate an enormous number of transmissions. Focusing is thus superior to anything achievable with standard focused transmissions, but at a much greater frame rate. Figure 2.10 illustrates this concept.

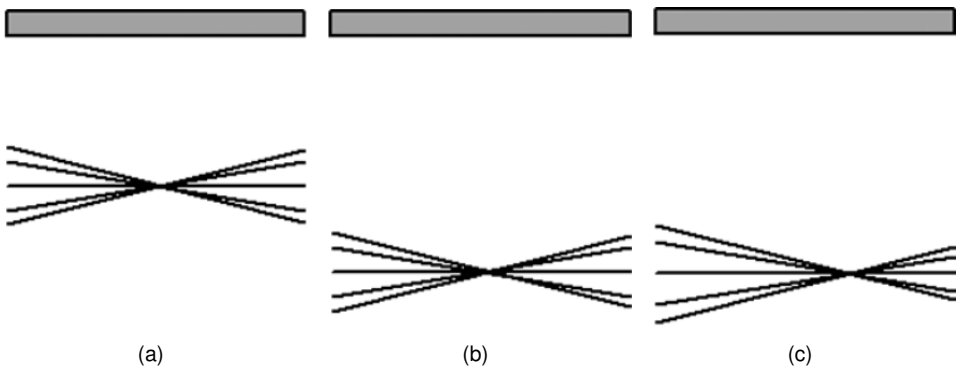

Figure 2.10: Multiple-point focusing in plane wave coherent compounding (a) As the plane waves propagate through the FOV, all waves sum coherently in one point. (b) As they continue to propagate, more points along depth are coherently summed. This is true for all points along the depth. (c) If each wave is considered at a different time, there will be an intersection of all waves in points lateral to the center (adapted from Montaldo et al., 2009, IEEE Transactions on UFFC, 56(3), p. 494).

The coherent compounding technique poses a trade-off: image quality *versus* frame rate. However, this is a trade-off which provides a lot of room for experimentation for the best possible combination of parameters. If a minimum frame rate is necessary to image certain phenomena, such as shear wave propagation or mitral valve opening and closing, the number of compounded plane waves can be chosen such that at least the minimum frame rate is achieved, maximizing image quality for that frame rate. When frame rate is not as important, a larger number of compounded LRIs can be used to achieve the best possible image quality. The maximum frame rate is achieved when one single plane wave is used, and is given by the double the time sound takes to reach the required depth, d. Frame rate reduces by a factor equal to the number of plane waves used, N_{waves}:

$$\text{frame rate (CC)} = \frac{1}{N_{\text{waves}}} \frac{2d}{c_0} \tag{2.29}$$

Where CC stands for "Coherent Compounding" and c_0 is the speed of sound.

Since the works of Montaldo et al., many research groups have experimented with coherent compounding in a multitude of fields outside of B-mode, including colour flow with Doppler [35, 36], super resolution [37, 38], contrast and harmonic imaging [9, 39, 40] and elastography [41, 42] with generally positive results. Echocardiography is one of the fields where coherent compounding may bring the most improvements. Because the myocardium contracts very rapidly, conventional ultrasound frame rates do not provide sufficient temporal resolution to accurately assess the full range of motion. Moreover, to image the mitral valve's opening and closing with sufficient temporal resolution, frame rates of around 200-300 Hz are needed [19].

To image a full heart, however, a very wide FOV is necessary. Plane waves are not optimal to image wide areas, since a plane wave can only be as wide as the width of the aperture. To circumvent this limitation, a different kind of unfocused transmission can be utilized: diverging waves.

Diverging waves, also named circular waves, are waves that have the virtual focus center outside the FOV. As they propagate through the medium the wave continuously diverges, effectively increasing the width of the insonified area as the depth increases. Figure 2.11 illustrates the transmission of a diverging wave.

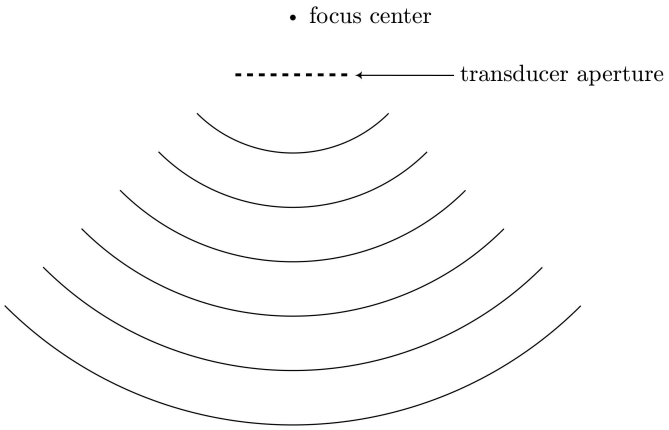

Figure 2.11: Diverging wave propagation from the aperture of a phased array transducer. As the wave propagates, the wider the beam becomes. This transmission is similar to fan beams used in CT.

The first in-vivo demonstration of coherent compounding with diverging waves for echocardiography was published by Couade et al. (a collaborative work between many researchers, including Fink and Tanter, both co-authors of the original plane wave coherent compounding approach) [8]. The authors were capable of imaging the sheep heart with the transducer placed directly in the epicardium of the left ventricle (the heart was exposed with lateral thoracotomy while the animal was under general anesthesia). The acquired data had sufficient quality to evaluate the heart motion, such as left ventricular wall tracking and measurement of tissue velocities with tissue Doppler imaging (TDI).

In a study that compared the usage of plane waves, diverging waves and conventional sector scanners for echocardiography with parallel receive beamforming, Hasegawa and Kanai highlighted the superiority of coherent compounding with diverging waves for cardiac applications [43]. The authors state

that the diverging transmission is more versatile than plane waves, as the beam can be as wide as necessary, since the virtual focus center can be set at different distances from the aperture. The researchers were able to image the human heart at a frame rate of 316 Hz using coherent compounding, while only at 39 Hz with conventional sector scans - an 8-fold improvement. Image quality was similar for all tested methods.

Papadacci et al. evaluated the influence of the number of compounded LRIs in image quality [3]. As the number of compounded LRIs increases, so does the contrast and the signal-to-noise ratio, and clutter is reduced.

Coherent compounding with unfocused waves has become the standard transmission in the state of the art of research in high frame rate ultrasound imaging. However, despite the high frame rate, it suffers from motion artefacts since it requires coherence during compounding. The next section explains how degradation occurs and summarizes the existing methods to compensate for the effects of motion.

2.4 Motion compensation in ultrafast ultrasound imaging

Since the works of Montaldo et al., the "creators" of coherent compounding with plane waves, that many authors have realised motion can have devastating effects in B-mode images [4, 5, 10, 11]. Coherent compounding, as a spatial compounding method, requires that the positions of the scatterers in the imaged medium remain the same between multiple transmissions. Whenever that is not the case, the sum is no longer spatially coherent, and it typically results in motion artefacts with loss of intensity where coherence was not verified - the image brightness is much lower than expected.

Motion is not problematic in all fields. For instance, elastography extracts the displacements from each of the frames to build overall elasticity and stiffness maps. Motion is the actual parameter being imaged with ultrasounds, and the anatomy image has little to no importance. When imaging regions where no motion is present - for example, soft tissues in the absence of blood vessels in the FOV - the effects of motion can be minor. But in the fields of echocardiography, where large motions occur constantly, or in ultrasound super resolution[2], where very small motions can result in large incoherence between frames, motion compensation is almost mandatory.

2.4.1 The burden of motion in coherent compounding

To illustrate the effects of motion in coherent compounding consider a disc with two distinct regions - half of the disc is hyperechoic, appearing as bright in the image, and the other half is anechoic, appearing as dark in the image. Now consider that the disc is rotating in the clockwise direction. As each of the images is acquired, the positions of the scatterers that compose it move to a different location. If between the two transmissions a weak scatterer is in a position where a strong scatterer used to be, during coherent compounding the contributions from two different scatterers will sum to produce

[2]Ultrasound super resolution is an imaging modality where the achieved resolution is higher than the ultrasound diffraction limit. This can be achieved by localization and tracking of microbubble contrast agents, and is used to image very thin blood vessels [44]. Since very small structures are imaged, small motions can influence the images tremendously.

brightness equivalent to the "average scatterer" of those two. Figure 2.12 illustrates this. The disc on the left represents the first acquisition and the disc on the center represents the second one. As the disc rotates, the black and white regions change positions. When the images are compounded, the regions of the two discs where the black and white regions don't match exactly, the intensity will be the average of the two.

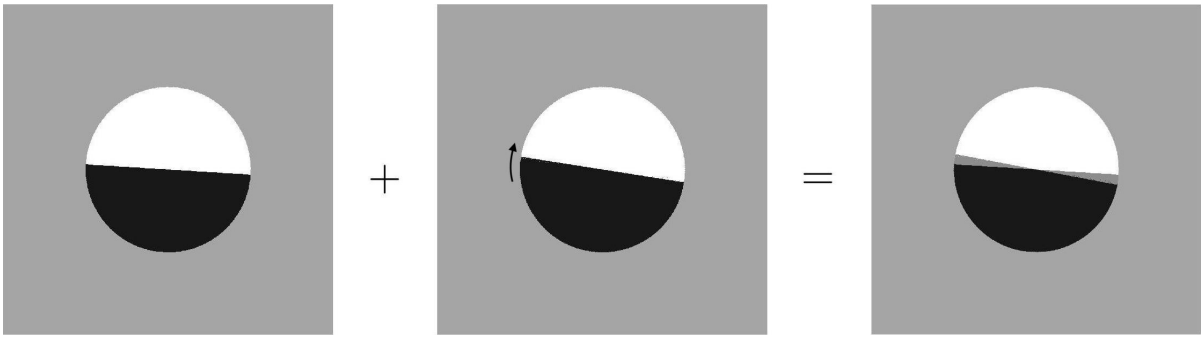

Figure 2.12: Loss of intensity during coherent compounding of two frames due to motion incoherence in a clockwise rotating disc with two distinct scattering regions.

This over-simplified example demonstrates the effects of motion degradation in coherent compounding. However, only two compounded transmissions were considered. In practice, many more compounded LRIs are used to achieve sufficient signal-to-noise ratio. As the object in the FOV moves throughout the acquisition, the more motion incoherence accumulates between each compounding angle, further reducing the intensity of the original object. Figure 2.13 shows the effect of compounding more frames, in this case, 32. The imaged object is now very different from what it truly looks like (Figure 2.12, left or center).

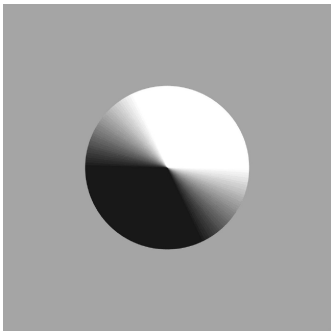

Figure 2.13: Compounding of 32 frames of a rotating disc phantom. The larger the number of compounded frames, the more degradation due to motion ensues in the final image.

Note that these examples are merely illustrative and do not fully translate to ultrasound imaging, especially because compounding in ultrafast imaging is carried directly on RF data and not the image intensities. Because the RF frequency functions as a carrier wave to the actual scattering data, data is oscillatory and zero-mean. So incoherent sums lead to approximation of the mean of the signal, resulting in loss of signal, which translates to loss of intensity in the finalized image (after envelope detection and log-compression). So, in practice, intensity loss due to motion incoherence is even more drastic in diagnostic ultrasound imaging. Additionally, the imaged mediums are largely heterogeneous,

making perfect coherence during compounding a challenge by itself. Speckle and clutter noise further decorrelate the LRIs.

2.4.2 Doppler motion compensation: correlation-based methods

When an acoustic source countinously emits a wave with certain frequency, and an ultrasound scatterer is moving in reference to the source, the scattered wave's frequency will be shifted by an amount proportional to the velocity of the scatterer. This phenomenon was first described by Christian Doppler in 1842 and is known as the Doppler effect. Since ultrasound naturally needs acoustic wave emissions to produce images, and motion of tissues shifts the frequency of the emitted wave, the velocity of tissues can be determined from the frequency shift using the Doppler equation.

In practice, pulsed transmissions are used instead of continuous ones. This makes the determination of the frequency shift more challenging because of the short duration of the scattered pulse. However, in pulsed methods, a phase shift also occurs due to motion, which is more easily quantifiable. While this approach does not directly estimate the frequency shift, it is not exactly an employment of the Doppler effect. Despite this, methods relying on estimation of phase shifts due to motion are generally referred to as Doppler methods in ultrasound scientific literature.

To estimate motion between the transmissions of coherent compounding, cross-correlations can be used to determine the phase-shifts between them. Between each LRI acquisition the motions are bound to be very small and so the LRIs are highly correlated with each other. The cross-correlation is computed between pairs of consecutive images from which the necessary phase shifts for motion correction can be computed. After the LRIs have been appropriately shifted, these are compounded. Using these phase-shifts, the velocities of the tissues can be computed with the Doppler equation. In a sense, this method is equivalent to TDI. For this reason, correlation-based methods are often called Doppler-based methods as well.

The main advantage of a correlation-based method is its low computational load. Correlations can be computed quite fast, maintaining the real-time capability of ultrasonography.

Despite the simplicity of the approach, there are ways in which this methodology can be optimized, specifically the ordering of acquisition of the imaging sequence, the correlation operation to be performed, the number of compounded LRIs and the angular range of tilted images.

Denarie et al. tested the influence of the angle-sequence ordering and the number of transmit directions, using a cross-correlation method to determine the velocities of the moving structures in the image (the heart, in their case) [4]. In particular, the authors tested linear angle sequences and alternating ones. To exemplify, a linear sequence of angles between -9° and 9° with an angle increment of 2° would be $[-9, -7, -5, ..., 7, 9]$, while an alternating sequence would be $[-9, 9, -7, 7, ..., -1, 1]$. Linear sequences, when combined with correlation-based motion compensation methods rephase sidelobes, degrading image quality. This effect was expected to be reduced with the alternating angle sequence. However, the alternating sequence leads to lower correlations of the IQ signals and thus motion estimation is compromised. The authors rejected nonsensical estimated velocities by thresholding. Using a

smaller number of angle increments was also expected to decrease sensitivity to motion, but in fact this leads to the formation of additional grating lobes. Added to the fact that a smaller number of compounded images is being used, images become very low-resolution.

A different angle sequence was investigated by Porée et al. [11]. A "triangle sequence"[3], as the authors called it, has the effect of removing coherent summation of sidelobes while getting accurate Doppler velocities. A different correlation method is also used, the Doppler autocorrelator. This different approach allows the computation of the phase shifts during beamforming, decreasing the computation times. The main disadvantage of this approach is that it can only correct axial motion. Lateral motions cannot be estimated and therefore remain uncompensated. While these movements affect the image quality much less than axial movements, these may still affect the quality of the images negatively. Another limitation is that it is prone to aliasing. With the chosen parameters, the maximum achievable velocity was 30 cm/s, which is enough to estimate motion in the myocardium, but not enough to image the mitral leaflets, inducing destructive interference during motion compensation.

The MoCo method proposed by Porée was adapted for velocity vector tracking in echocardiography in-vitro [45]. While nothing new was performed in terms of motion correction, this work highlighted the capabilities of the proposed MoCo approach, as the authors accurately determined the velocity vector field of a spinning tissue-mimicking disc. Furthermore, when no MoCo was used, the quality of the images degraded significantly, to a point where it is very difficult to resolve structures qualitatively. MoCo is thus essential for any application where motion is present. With the proposed method, higher velocity estimation errors occurred when the velocities of the spinning disc were higher due to aliasing, a problem that remains to be dealt with.

All the previous methods were investigated for non-contrast imaging; that is, without the use of contrast agents. Since the most precise ways of performing contrast-enhanced ultrasound imaging require the transmission of multiple pulses to eliminate the fundamental component, the consequences of motion compensation is even more catastrophic, as deficient elimination of the fundamental component due to dephasing occur. Toulemonde and Tang (2020) adapted the MoCo approach developed by Poreé et al. to contrast enhanced ultrasound. To eliminate the fundamental component, two successive pulses in opposing phases were transmitted for each angle to perform pulse inversion. A high-pass 5th order Butterworth filter was also applied in case imperfect cancellation occurred. To improve SNR, 7 consecutive compounded images were incoherently averaged. Their adapted MoCo approach is able to correct some of the motion artefacts, but due to Doppler aliasing some other artefacts are created. The greatest advantage of this MoCo approach is its speed, as processing times below one second are achieved for each frame. While not quite capable for real-time imaging, it is two orders of magnitude faster than the most common image registration methods. The results can potentially be improved if a triangular angle sequence is used instead of a linear one. [46]

Correlation-based motion correction methods have been proven successful in ultrasound localization microscopy using contrast agents, specifically to correct sub-wavelength motion [47]. Rigid motions are accurately corrected with phase delays computed from cross-correlation in the frequency domain.

[3]The triangle sequence is explained in section 3.5.3.

Correction of these sort of simple motions are enough for microscopy, but may not necessarily be the case when imaging larger structures, as non-rigid and out of plane motions are not accurately described using rigid parametrization. Nevertheless, it is a stepping-stone for future developments in correlation-based methods.

With the purpose of keeping the frame rate high, Brekke et al. (2013) investigated the use of only a few transducer elements in both transmission and reception for TDI [48]. While all lines are acquired for B-mode, for a cardiac application, only the necessary elements to image the myocardium were used for tissue Doppler. Phase delays are computed from the cross-correlations of pairs of consecutive complex IQ signals, which are used to estimate the velocity of the tissues using the Doppler equation. Results were in accordance with traditional TDI.

One of the largest problems in motion compensation is sidelobe realignemnt during motion-corrected beamforming. Dual aperture motion compensation (DAMoCo) can partially solve this problem by only tracking motion of the mainlobe signal [49]. As with coherent compounding, several LRIs are acquired at different angles. At each of these LRIs, a random rectangular window apodization is applied, from which the motion is estimated. Motion compensation is performed on a fixed smaller-aperture such that only the mainlobe is compensated. The LRIs are then compounded to achieve a motion compensated frame. While sidelobe suppression and motion estimation was accurate in-vitro, the same cannot be said for in-vivo, but the acquisitions were not performed with optimal parameters. Firstly, the frame rate for in-vivo acquistions was 60 Hz, much lower than the 2000 Hz for in-vitro. Larger inter-frame decorrelations occur at slower frame rates. Also, the angle increments were 11.25°. This also decreases correlation due to large rotations of the point-spread function (PSF) patterns, and thus sidelobe suppression wasn't as noticeable.

Correlation-based methods have also been demonstrated for motion compensation in STA imaging [50]. Motion compensation is necessary because information from multiple transmit events is combined to produce an image. In STA, it is possible to not only estimate the magnitude of velocity but also the direction of movement, which is not possible with typical correlation methods and coherent compounding. It can be done during beamforming. Unfortunately, this methodology is not feasible for high-frame-rate visualization by the pulse sequences necessary for STA.

Nie et al. developed a two-stage motion compensation for CEUS [51]. The first stage of the approach was to perform rigid block matching. The second stage refines the window iteratively to improve resolution. Both stages are based on cross-correlation of beamformed image pairs. Accurate measurements were achieved with capability for left ventricle velocity vector imaging. It has advantages over Doppler as it can estimate 2D velocities and does not suffer from aliasing. However, it is much slower than Doppler, since the mean processing time per frame was 130 s. It can possibly be improved in the future by implementing the algorithm on a GPU, but it is still far away from being ready for real-time imaging.

2.4.3 Point-based registration methods

Image registration methods are closer to the classical image processing and computer vision approaches to motion problems. The main idea is to devise a model for the motion to be estimated. A set of images is fitted into the model, such that one of them serves as the reference. Motion is estimated according to this reference image. After motion estimation, the inverse transformation is applied to each of the LRIs and then these are compounded. This class of methods is usually very accurate and can determine velocities in both axes. Despite this, these methods are not preferred over correlation-based methods when real-time imaging is necessary, as they can be extremely computationally expensive. There is a trade-off then between speed and accuracy.

Harput el al. adapted an image registration method to correct motion in MRI to work on super resolution imaging [52]. During acquisitions, several sources of motion exist - US probe, respiratory, cardiac and other patients' movements. There may then be global rigid motion and local non-rigid and out-of-plane motion. To correct for both types of motion, a two-stage motion estimation algorithm was investigated. It is able to model rigid, affine and non-rigid motions using a "B-spline-based free form deformation that can estimate the local compression and rarefaction of tissue". The first stage consists in finding a global affine transformation as an initial rough estimate. This estimate is refined in the second stage where non-rigid motion is assumed. The approach is iterative and many iterations are necessary to model more complex motions. Very small errors are achieved with this algorithm, no matter the amplitude of motion. The only disadvantage is the computation time, as it can take more than one minute to process a single frame.

The previous image registration algorithm initially developed for MRI was then investigated for CEUS of the heart by Stanziola and Toulemonde et al. (2019) [10]. For compounding, 11 angles were used (acquiring 2 images per angle for pulse inversion) and after compounding, 7 consecutive frames were incoherently averaged to achieve higher SNR. Motion correction was evaluated by determining the contrast to tissue ratio (CTR) as well as the contrast-to-acoutisc noise ratio (CANR). Great improvements were achieved in both metrics, with the CANR being especially high when the average of 7 frames is considered. The achieved processing time was 71 ± 10 s, which is far from being feasible for real-time imaging. Despite this, the authors state the method has not been fully optimized for contrast echocardiography, so potential improvements can emerge with further research. Their simulations studies also show that this framework is only possible for dense clouds of microbubbles and not sparse distributions, making it difficult to image smaller vessels.

Bakas et al. published a review on point-based registration techniques (PBRTs) for motion correction in CEUS, specifically for evaluation of focal liver lesions [53]. Nineteen different implementations of PBRTs are evaluated - HOG, Harris, SIFT, SURF, FAST and CARD. The idea is to find keypoints in common between pairs of images and determine a parametrizable transformation between the two to perform registration. The best performing registration technique was 128-bit CARD, as it is consistently very accurate and capable of processing 5 frames per second. It is undoubtedly promising, especially because all the algorithms were implemented on single-core CPUs. Processing can be potentially sped-up if any of the algorithms are parallelizable. Since this study was undertaken on liver data, a rigid

description of motion was sufficient. However, this is certainly not true for cardiac applications. Thus, it is difficult to extend the reasoning for other applications where motions are non-rigid. It is expected that motion correction becomes more challenging for complex motions, such as the ones observable in the heart. Performance of PBRTs is expected to worsen, both in speed and accuracy, but a more comprehensive study of these techniques for cardiac applications is still necessary to fully evaluate feasibility.

Nie et al. compared their developed correlation-based method with the most commonly used image registration algorithm [54], which has been evaluated on a number of papers ([10], [52]). The comparison was undertaken on tissue-mimicking rotating disc phantoms, and also in-vivo, while imaging the heart of a healthy volunteer. While improved CTR and CNR were achieved with the correlation-based method, both methods are highly dependent on the reference image to perform registration [55]. It would have been interesting to evaluate the influence of reference image to register. Both methods are not feasible for real-time imaging, so simpler crosscorrelation and autocorrelation approaches are preferred if temporal resolution is important.

2.5 Contrast imaging in ultrasound

Contrast agents are substances used in all imaging modalities to increase the sensitivity of the imaging technique by altering the image contrast between different structures. The general idea is to increase signal in the region where the contrast agent is in comparison to the amount of signal generated from regions where the contrast agent is not present, increasing image contrast between structures. Contrast agents in ultrasound imaging are composed of a solution of gas-filled microbubbles. The dramatic increase in ultrasound scattering by microbubbles has made them useful to image vessels and organs for which the ultrasound signal to noise ratio is inadequate to make a clinical diagnosis.

Microbubbles contrast agents are administered intravenously and thus are mostly used to generate contrast between blood and surrounding tissues. Contrast imaging shines brightest in perfusion or blood flow diagnostic imaging, such as echocardiography. Additionally, it can increase the sensitivity of flow Doppler [56]. Given sufficiently high pressure, microbubbles generate strong harmonic signal due to their high nonlinearity parameter, B/A [57, 58]. It is through the harmonic signals that contrast is generated between surrounding tissue and blood vessels in contrast ultrasound imaging.

2.5.1 Microbubble scattering, nonlinearity and harmonic generation

Because the wavelengths used in diagnostic ultrasound are 2-3 orders of magnitude larger than the diameters of microbubbles, we are led to believe these behave like a Rayleigh scatterer. However, because of its high compressibility and expandibility, the scattering cross-section of a micro-bubble can be up to 10^8 times greater than a rigid spherical scatterer of the same size [59].

An air microbubble has a flexible boundary surrounded by a fluid (water or blood). In the presence of an acoustic pressure field, the microbubble contracts and expands with the rhythm of the compressional

and rarefactional half-cycles of the wave. The motion of the microbubble is mechanically controlled by the springlike stiffness of the inner gas and the inertia of the surrounding fluid [12]. Both factors combine to result in a resonant frequency given by:

$$f_r = \frac{1}{2\pi r}\sqrt{\frac{3\gamma_c P_0}{\rho}} \tag{2.30}$$

Where r is the equilibrium bubble radius, γ_c is the ratio of heat capacities at constant pressure and constant volume, ρ is the density of the surrounding medium and P_0 is the static pressure at the surface of the bubble.

This linear model of a bubble in a fluid is equivalent to a damped harmonic oscillator. The scattering cross-section of a gas-filled microbubble increases with the frequency of the incident wave until it reaches a maximum at its resonance frequency, f_r, and drops to around 1000 times afterwards, remaining constant after that frequency [14].

This linear approximation only holds for small amplitudes of the incident pressure wave. As the pressure amplitude increases, so does the density of particles in the compressional zones and the sparsity in rarefactional zones. A microbubble can expand in response to highly rarefacted pressures, but there's a limit to how much the gas inside the bubble can compress. The pressure response of a gas-filled microbubble thus becomes asymmetric in response to high-amplitude acoustic waves. This asymmetric response generates harmonics in accordance with the Rayleigh-Plesset equation, which has multiple nonlinear terms on the bubble radius. For more details on microbubble motion models, see any of the following publications [60–62].

The effects of nonlinear scattering through microbubbles are most easily understood by considering the amplitude response. A scatterer is said to be linear if the amplitude of the echo produced from wave scattering is a set fraction of the amplitude of the incident wave, no matter the incident amplitude. Because this condition applies across time, it follows that the waveform of the echo is equal to the incident waveform. Since microbubbles are a type of media where nonlinear scattering occurs, this linear condition does not hold. The waveform of the echo produced from microbubble scattering is very different from the transmitted waveform, as shown in Figure 2.14.

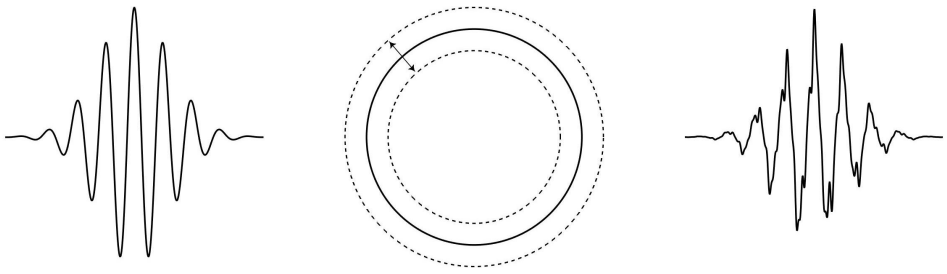

Figure 2.14: Nonlinear scattering in a microbubble. The incident waveform (left) is scattered by a continuously contracting and expanding microbubble (center), generating an echo (right) that is a distorted version of the original waveform.

Upon nonlinear scattering, the distorted echo waveform is not only composed of a spectrum centred at the transmitted frequency, f_0, also called the fundamental, but also of harmonic frequencies (usually

simply named 'harmonics'), which are multiples of the transmitted frequency, $2f_0$, $3f_0$, $4f_0$, etc. The generation of these harmonics is key for contrast imaging, since harmonic signal generated from microbubbles is much stronger than harmonic signal generated from tissues, generating high contrasts. The general objective is contrast imaging is to eliminate linear tissue signal composed of fundamental frequency such that the harmonic signal generated by microbubbles is the source of contrast in the image.

Generally, eliminating the fundamental signal requires the usage of multi-pulse techniques, such as pulse inversion or amplitude modulation.

2.5.2 Ultrafast contrast enhanced ultrasound

Contrast enhanced ultrasound has been paired with ultrafast imaging using coherent compounding to image several human tissues and organs, such as kidney, liver and the heart. To image certain organs where blood flow is key to understand its function or presence of disease, using ultrasound contrast agents greatly benefits the diagnostic power of the imaging method.

Couture et al. were the first to demonstrate ultrafast contrast-enhanced ultrasound using coherent compounding of plane waves [63]. The authors tested both pulse PI and AM methods[4] for elimination of linear tissue signal using plane waves, both before and after bubble disruption in a tube phantom in-vitro. The achieved contrast using microbubbles was very high after around 20 milliseconds after bubble disruption.

The same authors compared sensitivity of microbubbles when excited with conventional focused beams and unfocused waves [39]. Before bubble disruption, the sensitivity of microbubbles was shown to be higher with plane waves, evaluated from the increase in CTR when using multi-pulse sequences such as PI and AM. The authors state that there is still a lot of room for optimization of parameters for contrast enhanced ultrafast ultrasound in terms of the preferred frequencies, pressures and mechanical indexes (MI), postulating that keeping the microbubbles intact for the whole duration of the imaging sequence could drastically improve the accuracy of perfusion studies.

A similar study was carried out by Viti et al. in 2016 [64]. The author investigated the effects of the number of compounded LRIs in coherent compounding and the transmit pressure in both coherent compounding and conventional line-by-line amplitude modulation, in conditions of non-disruption of the contrast agents. The high-frame-rte approach achieved drastically better contrast than the conventional method. Additionally, the authors noticed that contrast between the flow and the tissue was higher when a smaller number of LRIs are used. The proposed explanation was that the concentration of microbubbles decreases during the acquisition, decorrelating the LRIs and resulting in some incoherence during compounding. The tested pressures (70 kPa - 140 kPa peak negative pressure) did not result in significant difference in microbubble response.

The influence of flow velocity and ultrasound pressure in plane wave coherent compounding PI CEUS were further investigated by Zhu et al. in a lymphatic vessel phantom [65]. The researchers found that

[4]The theoretical concepts behind pulse inversion and amplitude modulation and their respective methodologies will be explained in detail in section 3.2.1.

in conditions of slow flows, mechanical indices play a big role in the achieved contrast. Under slow flow, higher MIs generate higher contrast but at the cost of bubble persistence, and the opposite happens for lower MIs. For fast flows, MI does not play as big of a role in the image contrast.

Toulemonde et al. have investigated contrast enhanced echocardiography in a series of papers [5, 9, 66, 67]. The authors have demonstrated high frame rate contrast enhanced echocardiography using coherent compounding of diverging waves in vivo. Additionally, they also described the types of motion artefacts created from motion incoherence between LRIs in contrast mode and stated that a computationally inexpensive motion compensation scheme would greatly benefit ultrafast contrast echocardiography.

Chapter 3

Methods

With the objective of investigating motion compensation schemes for multipulse CEUS a simulation study was developed. The steps taken to achieve a comprehensive study were the following:

1. Choose an ultrasound simulation software;
2. Create a motion phantom;
3. Simulate unfocused insonification of the medium phantom using multipulse contrast techniques;
4. Reconstruct the ultrasound data using appropriate delay and sum beamforming;
5. Apply motion compensation scheme;
6. Evaluate motion-compensated data and compare with static data and uncompensated motion data;

The ordering of this chapter follows precisely the ordering of the acquisition and processing pipeline.

3.1 Simulations of diagnostic ultrasound using k-Wave

The data that was used to estimate and compensate motion on was simulation-generated. There are several open-source software packages capable of simulating ultrasound propagation for diagnostic imaging purposes, but only a few can simulate nonlinear propagation. Since this dissertation focuses on contrast imaging, which is inherently linked with nonlinear scattering, the ability to simulate nonlinearity is key. For this reason, the software simulation of choice was k-Wave, which is a MATLAB toolbox [68]. The three main reasons the k-Wave toolbox was chosen are the following:

1. Ability to simulate nonlinearity;
2. Can be GPU-accelerated;
3. Has a comprehensive user manual and great community support through the k-Wave forum.

No other simulation software unites these three characteristics.

For a given medium, computational grid and pressure sources, the measured pressure at the acoustic sensors is computed using a k-space pseudospectral method [68]. Coupled with the wave equation (2.1), momentum conservation, mass conservation and nonlinear pressure-density relation equations are used to solve for the pressure field and velocities at each point in space and time. All the equations are directly written in the Fourier domain, or k-space, and solved directly for the spatial Fourier transforms of pressure and velocity.

In this section, an overview of the inputs fed to k-Wave's first order numerical solver will be presented. For more details on k-Wave's k-space pseudospectral method for acoustic wave propagation, nonlinear interactions or general functioning of the toolbox see any of the following publications [68–70].

3.1.1 Computational grid

The computational grid defines the positions at which the properties of the medium are known. These serve as the key-points for computation of the pressure field. For a grid size $N_x \times N_z$ and imaged depth d, to generate a uniformly spaced grid the grid spacing in the x direction, dx and in the z direction dz are given by:

$$dx = \frac{d}{N_x} = \frac{d}{N_z} = dz \tag{3.1}$$

One grid is formed for the x coordinates and another one for the z coordinates, and each is given by a matrix X_{ij} or Z_{ij}, respectively. The grid matrix entries are given by the following relation:

$$X_{ij} = jdx - dx\frac{N_x - 1}{2} \tag{3.2}$$

$$Z_{ij} = idz - dz\frac{N_z - 1}{2} \tag{3.3}$$

From equations 3.2 and 3.3 it is clear to see that the origins of the grids are located at their center. For the upcoming analysis it will also be useful to denote the set of all points in the grid by $\mathbf{p}$. This array $\mathbf{p}$ is a $(N_x N_z) \times 2$ matrix, where each row contains a point in the grid and the columns the corresponding x and z coordinates given by equations 3.2 and 3.3.

With the grid defined, the time step and number of steps to finish the simulation can be computed. For the simulation to be stable and accurate the time step is chosen according to equation 3.4:

$$dt = \frac{\mathrm{CFL}dx}{c_{max}} \tag{3.4}$$

where CFL is the one-dimensional Courant-Friedrichs-Lewy number and is a measure of stability of the numerical method. The software developers recommend a CFL number of 0.3 for a stable yet accurate simulation [68]. c_{max} is the maximum speed of sound found in the medium. For an unfocused transmission at an imaging depth of d, the final time step for computation, given a reference speed of

sound c_0 is given by:

$$t_{end} = \frac{2d}{c_0} \tag{3.5}$$

The time points at which acoustic propagation is simulated are the ones given by the following values:

$$t = 0,\ dt,\ 2dt,\ ...,\ dt\left\lceil \frac{t_{end}}{dt} \right\rceil \tag{3.6}$$

where $\lceil \cdot \rceil$ represents the ceiling operator (equivalent to rounding to the nearest integer above the argument). It is used to ensure each time step is an integer multiple of dt and that the desired imaging depth is always reached.

3.1.2 Medium

The medium of insonification is where the properties of an ultrasound propagation phantom are set. The variables that can be set as properties of the medium are:

- Sound speed, c_{ij} in m/s
- Density, ρ_{ij} in kg/m^3
- Nonlinearity parameter B/A, b_{ij}, unitless
- Attenuation coefficient, α in dB/(MHz^y cm)
- Attenuation exponent, y, unitless

All matrices in the list above are $N_x \times N_z$, so each entry in the matrix coincides with an (x, z) position in the computational grid. For diagnostic ultrasound, the sound speed and density maps are the parameters that define the anatomy. The attenuation parameters α and y can be set according to the tissue that one wishes to emulate. For contrast imaging with multipulse techniques, the nonlinearity parameter map will ensure the generation of harmonics according to B/A values given.

Phantom design

Since the motion compensation scheme that is going to be evaluated is the Doppler autocorrelator, the only types of motion that are susceptible to being compensated for are axial ones. Having a wide range of axial velocities is hence valuable. Rotation motions in circular objects are ideal for axial velocity evaluation for two reasons:

1. The magnitude of the velocity increases linearly radially from the center;
2. The direction of the velocity is always perpendicular to the distance vector from the center;

These two properties combined create an axial velocity profile that linearly increases in the lateral direction from the maximum negative velocity to the maximum positive velocity, passing by zero at the center.

On another note, because loss of contrast is common in motion degraded images due to coherent compounding, having both anechoic and hyperechoic regions will provide a way to compare contrast recovery in motion compensated images.

The phantom that was modeled to evaluate a wide range of velocities and contrast recovery was a rotating disc with anechoic inclusions. This type of phantom has been previously evaluated in other motion estimation and compensation studies, albeit in-vitro and not in simulation [11, 45, 51]. The chosen radius of the disc was 2.5 cm, while the cysts had a radius of 0.375 cm, with a distance from the center of the disc of 1.75 cm. The size of the entire medium was 10 cm $\times$ 10 cm and the disc was placed at its center.

The phantom was generated by creating a map of sound speeds. The reference sound speed was chosen to be $c_0 =$ 1540 m/s as it is the mean sound speed of soft tissue [18]. For the highly scattering region - the disc itself - random variations about the mean value of c_0 were introduced with standard deviation $\sigma_{disc} =$ 15.4 m/s, or 1% of c_0. For the anechoic inclusions, since those are poorly scattering, the standard deviation of random variations was much lower with standard deviation $\sigma_{cyst} =$ 0.77 m/s or 0.05%. From the analysis in section 2.1.1, we know that scattering occurs when the differences between acoustic impedances are large. By introducing sufficiently large random variations, hyperechoic regions can be simulated. Inversely, by guaranteeing the variations across the mean are small, anechoic regions can be simulated.

Additionally, to simulate the effects of speckle, random noise was introduced across the entire sound speed map with standard deviation $\sigma_{noise} =$ 0.77 m/s or 0.05%. The standard deviation of noise σ_{noise} was maximized without surpassing σ_{cyst} so as to guarantee the desired level of echogenicity. A higher power of noise would result in a lower level of anechoicity in the cysts.

The attenuation parameters were chosen according to the ones measured in the human heart, as echocardiography is one of the modalities where motion compensation is most important. The attenuation coefficient of the heart and the corresponding attenuation power are given by $\alpha =$ 0.56 dB/(MHz^y cm) and $y = 1$, respectively [12].

The nonlinearity parameter was chosen to be $B/A =$1000 in the hyperechoic region and $B/A =$ 6 in the anechoic regions. The nonlinearity parameter map was chosen according to nonlinearity measurements in commercially distributed microbubbles [57, 58] and the heart [12, 71], respectively.

A maximum velocity of 30 cm/s was used for the rotating disc, which corresponds to an angular velocity of 12 rad/s, which corresponds to the peak velocities in the myocardium [72].

Table 3.1 summarizes the properties of the disc phantom.

Table 3.1: Summary of properties of the rotating disc phantom.

	Disc	Cysts / Background
Radius	2.5 cm	0.375 cm
B/A [12, 57, 58, 71]	1000	6
Sound speed [12]	1540 $\pm$ 15.4 m/s	1540 $\pm$ 0.77 m/s
Attenuation coefficient [12]	0.56 dB/(MHz cm)	
Angular velocity	12 rad/s	
Medium size	10 $\times$ 10 cm	

With the described parameters, the rotating disc phantom looks like the one presented in Figure 3.1.

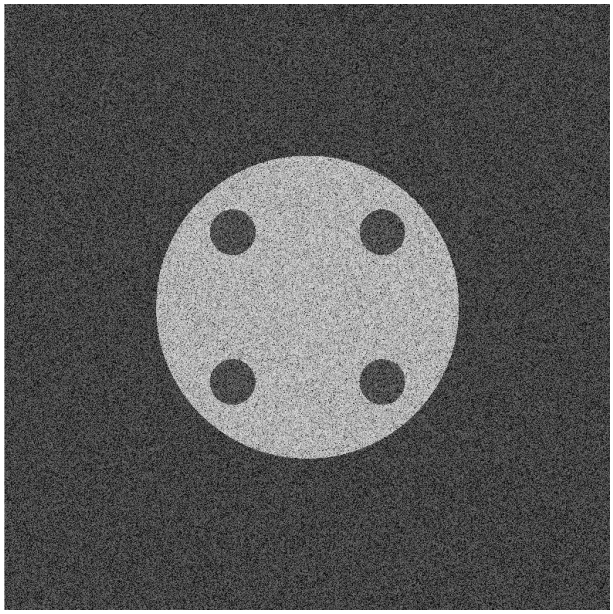

Figure 3.1: Rotating disc phantom as a sound speed map. Higher variations from the reference sound speed c_0 result in increased brightness. This figure was generated in reference to deviations from the mean acoording to $|c_{ij} - c_0|$.

The method for employing rotation in the disc is now explained. Consider the sound speed map c_{ij}. Instead of mapping c according to the indices (i, j), we use the corresponding coordinates in the grid, $\mathbf{p}$, and use the form $c(x, z)$ instead of c_{ij}. Consider also the subset of points in the grid that belong to the disc, $\mathbf{p_d}$. The positions of the grid coinciding with the disc were rotated an angle $d\theta$ using a rotation matrix R:

$$R(d\theta) = \begin{bmatrix} \cos d\theta & -\sin d\theta \\ \sin d\theta & \cos d\theta \end{bmatrix} \tag{3.7}$$

Rotation is employed in the following way:

$$\mathbf{p_d^{rot}} = R(d\theta)\mathbf{p_d} \tag{3.8}$$

and the rotated sound speed map is computed with:

$$c^{rot}(\mathbf{p_d^{rot}}) = c(\mathbf{p_d}) \tag{3.9}$$

For each grid point in $\mathbf{p}$, there is a corresponding pair of indices (i, j) in the sound speed map c_{ij}. Since the rotated set of points $\mathbf{p_d^{rot}}$ may not coincide with points on the original grid, they may not map to indices in the sound speed map. To ensure the closest possible mapping, the rotated points are approximated to the closest points in the original grid $\mathbf{p_d}$. For each point in $\mathbf{p_d^{rot}}$ the closest point in $\mathbf{p_d}$ is computed using a nearest neighbour approach. If the motions are very small, then the nearest neighbor in $\mathbf{p_d}$ might be the same point before rotation, so some errors are introduced using this methodology. Let $\mathcal{C}_{nn}\{\mathbf{x_1}, \mathbf{x_2}\}$ be the nearest-neighbour operator, whose output is the nearest neighbour of $\mathbf{x_1}$ in $\mathbf{x_2}$.

The nearest neighbours approximation of $\mathbf{p_d^{rot}}$ is given by:

$$\widehat{\mathbf{p_d^{rot}}} = \mathcal{C}_{nn}\{\mathbf{p_d^{rot}}, \mathbf{p_d}\} \tag{3.10}$$

The hat accent above $\mathbf{p_d^{rot}}$ is used to denote its nearest neighbours approximation to $\mathbf{p_d}$. The only parameter left to determine is the angle step size. Assuming the disc is approximately static during each acquisition, the rotation angle step size is given by:

$$d\theta = \frac{\omega}{\mathrm{PRF}} \tag{3.11}$$

where PRF is the pulse repetition frequency. New pulses can be sent anytime the echoes from the maximum depth, d, at which we wish to image arrive and is given by:

$$\mathrm{PRF} = \frac{c_0}{2d} \tag{3.12}$$

Now that every parameter is known, the sound speed map can be computed iteratively using the following expression, where t is the iteration number:

$$c^{t+1}\left(\widehat{R(d\theta)\mathbf{p_d}^t}\right) = c^t\left(\mathbf{p_d}^t\right) \tag{3.13}$$

All steps of the rotation can be computed from c^0 and $\mathbf{p_d}^0$, which are the non-rotated sound speed map and grid points belonging to the disc, respectively. Since the step size is uniform, each rotated sound speed map can also be computed directly from the first one ($t = 0$):

$$c^t\left(\widehat{R(td\theta)\mathbf{p_d}^0}\right) = c^0\left(\mathbf{p_d}^0\right) \tag{3.14}$$

This last expression was the one that was implemented as it suffers less from the nearest neighbor small motion approximation to the original point as t increases.

The errors induced by rotation can be minimized by using sufficiently fine grids for simulation. A grid size of 2048 $\times$ 2048 was chosen, as that is the minimum size for which the rotation errors are at most the length of the diagonal of a grid point. Larger grid sizes produce smaller errors, but also require a much larger amount of computational memory and time to run. k-Wave runs exclusively on the available memory of the graphics processing unit (GPU). The available GPU for simulations was a NVIDIAGeForce GTX 980 Ti GPU, which has 6 GB of memory. While this amount is enough for a 2048 $\times$ 2048, an estimated 16 GB of dedicated GPU memory would be necessary for a 4096 $\times$ 4096[1].

3.1.3 Sources and sensors

After the computational grid and mediums have been defined, certain points in the grid can be used as pressure sources - emitting pressure fields - or pressure sensors - recording pressure.

[1] k-Wave solves the wave equation directly in k-space, which requires many computations of the Fast Fourier Transform (FFT). The FFT is much more efficiently computed if the inputs are powers of two, hence why only grid sizes which are powers of two are considered.

Sources and sensors are defined in binary mask in k-Wave. Each point in the computational grid can be used as a source or a sensor, depending on whether the binary mask is set to 1 - logical true - or 0 - logical false - in that point. A binary mask is created for the source, M_{src} and another one for the sensor, M_{sns}, both of sizes $N_x \times N_z$.

The locations of point sources is set by placing 1s in the desired locations in the binary masks M_{src}. Consider a flat-faced phased array transducer with N elements, element length l and kerf k. Because the grid spacing is dx, to determine the number of grid points that compose the transducer dimensions we use the subscript N:

$$l_N = \left[\frac{l}{dx}\right], \; k_N = \left[\frac{k}{dx}\right], \tag{3.15}$$

Where the operator $[\cdot]$ is used to signify rounding to the nearest integer[2]. The transducer should be placed at the top of the medium that is to be imaged, which would be the first row of the binary mask M_{src}. Then, given a column index position for the first element, r, the first row of the source binary mask is filled with l_N consecutive 1s after the position r, followed by k_N 0s, followed again by l_N 1s and so on, until N sets of 1s in the first row have been filled. All the other entries in the mask are set to 0. Since the transducer should be placed in the exact same position in emission and reception, the places where the pressure signals are recorded, should be the exact same ones used for emission, and thus $M_{sns} = M_{src}$. Figure 3.2 shows an example of a source/sensor binary mask emulating a transducer. In

Figure 3.2: Source and sensor binary masks emulating a phased array transducer, where the yellow points represent the active sensor mask. In this case, $l_N = 5$, $k_N = 1$ and $N_x = N_z = 128$

practice, having a large number of emitters and receptors considerably slows down the simulations, so instead of using l_N 1s for each element, we use only one source point per element corresponding to the

[2]There is no convention on the symbol for "rounding to the nearest integer". The symbol $[\cdot]$ was chosen as it is a combination of the symbols for the floor and ceiling operators ($\lfloor\cdot\rfloor$ and $\lceil\cdot\rceil$, respectively), and it seemed fitting given that the function of round is also a middle-ground between floor and ceiling.

middle one, and the same for the sensor.

The input signal fed to each of the source points is an RF pulse of frequency f_0 and number of cycles N_{cycles}. The RF pulse bandwidth follows a Gaussian distribution with mean equal to f_0 and standard deviation proportional to N_{cycles}.

To generate unfocused transmissions, the input signals fed to each element in the array must be delayed by specific times to achieve the desired beamforming. Beamforming is explored in detail later in this chapter, section 3.3.

The transducer that was simulated was a Philips ATL P4-1 transducer, which has 96 elements and an aperture width of 2.8 cm.

3.2 Contrast Imaging

High-contrast images can be formed using multipulse methods. The greatest advantages of multipulse methods is their ability to eliminate linear tissue signal, maintaining the contrast-agents signal. Multipulse methods involve transmitting multiple pulses in succession and summing their echoes. Elimination of tissue signal occurs during the sum of the echoes due to linearity, and the nonlinear signal remains.

3.2.1 Pulse Inversion

The pulse inversion technique consists in transmitting two opposing-phase pulses in succession [73]. The first pulse is called the positive pulse and the second pulse, which is an inverted version of the first, is called the negative pulse. If the pulses only undergo linear scattering, the corresponding echoes are also inverted versions of each other. However, if nonlinear scattering occurs, harmonics are generated and the returning echoes are no longer inverted versions of each other.

Let $s(t)$ be an RF pulse of central frequency f_0. Let $x_+(t) = s(t)$ be the positive transmitted pulse and $x_-(t) = -s(t)$ be the negative transmitted pulse. Because the pulses undergo nonlinear scattering, the returning echoes are given by the following expression, where powers larger than 3 were omitted for simplicity:

$$\begin{aligned} y_+(t) &= a_1 x_+(t) + a_2 x_+(t)^2 + a_3 x_+(t)^3 \\ y_-(t) &= a_1 x_-(t) + a_2 x_-(t)^2 + a_3 x_-(t)^3 \end{aligned} \tag{3.16}$$

From power-reduction identities for sinusoidal waves, we know that powers of sines are composed of harmonic frequencies of the order of the power [74] In other words, the following can be written:

$$\sin(2\pi f_0 t)^n = \sin(2\pi n f_0 + \phi) + h(t) \tag{3.17}$$

Where ϕ represents a phase term and $h(t)$ is a function of time that includes other lower harmonics.

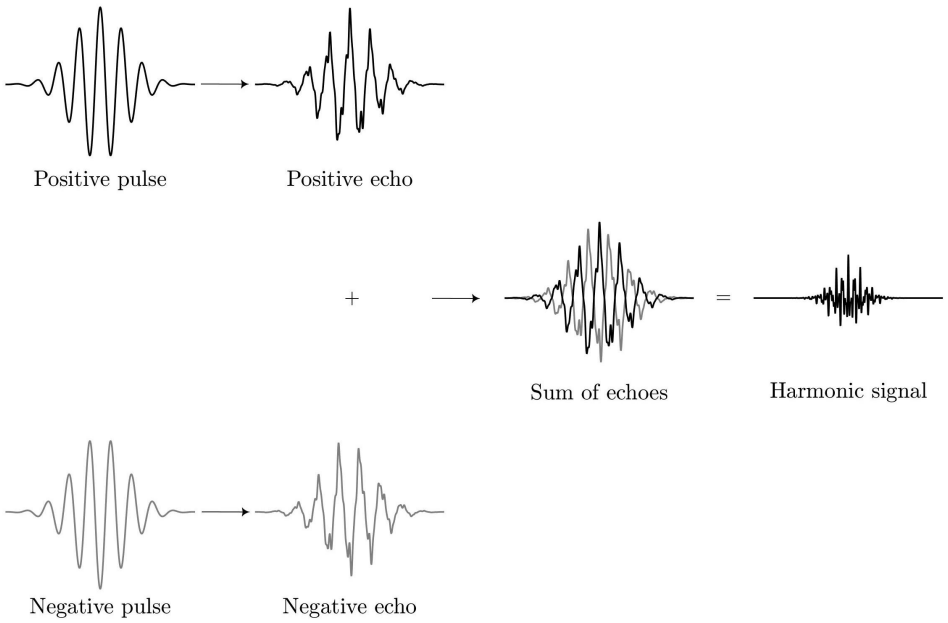

Figure 3.3: Summary of the pulse inversion technique: two pulses, inverted in phase, are transmitted and their echoes are received. The received echoes are summed to eliminate the linear component of the signal, remaining only the harmonic components.

Because of these identities, it is common to refer to powers of sines as harmonics, directly. Thus, we refer to the power terms in equation 3.16 as harmonics. Replacing $x_{\pm}(t)$ by $\pm s(t)$ in the previous equation:

$$\begin{aligned} y_{+}(t) &= a_1 s(t) + a_2 s(t)^2 + a_3 s(t)^3 \\ y_{-}(t) &= -a_1 s(t) + a_2 s(t)^2 - a_3 s(t)^3 \end{aligned} \tag{3.18}$$

If the positive and negative pulses are summed, we get:

$$y_{+}(t) + y_{-}(t) = 2a_2 s(t)^2 \tag{3.19}$$

All the odd harmonics are eliminated, while the even harmonics are doubled in amplitude. More generally, the sum of consecutive positive and negative pulses that underwent nonlinear scattering can be written as:

$$y_{+}(t) + y_{-}(t) = \sum_{n=1}^{\infty} 2a_{2n} s(t)^{2n} \tag{3.20}$$

Because tissue is a weak nonlinear scatterer, the harmonic signal that remains after pulse inversion is mainly generated from microbubbles [71, 73]. This technique then ensures that microbubbles act as the main source of contrast in the ultrasound image since tissue signal is eliminated. A summary of the PI technique is shown in Figure 3.3.

3.2.2 Amplitude Modulation

Amplitude Modulation consists of transmitting two or more pulses with the same waveform but with different amplitudes [75]. The simplest case would be to consider the transmission of two consecutive pulses, the second with half the amplitude of the first. If only linear scattering occurs, the second echo would also have half the amplitude of the first echo. But in the presence of microbubbles, due to their asymmetric contraction and expansion, the amplitudes of the echoes share a nonlinear relationship with the amplitudes of transmitted pulses, and thus the second received echo is no longer simply half of the first. If the first echo is summed with the second echo doubled, then the linear component of the images are eliminated, leaving only harmonic signal.

While in both amplitude and phase modulation (such as PI) methods the linear component of tissue is eliminated, a unique characteristic of amplitude modulation methods is that the fundamental component of microbubbles is retained in the image. There are several advantages to using fundamental microbubble signal in contrast imaging, rather than the harmonic signal:

- The fundamental signal is of much higher power;
- The fundamental frequency can be set as the center frequency of the probe such that it lies in a region of the transducer's bandwidth where reception is most efficient.
- The lower frequency echoes suffer less attenuation while returning to the transducer.

In practice, two-pulse Amplitude Modulation is challenging. Array transducers are not capable of precise beam-shaping such that pulses are half or twice the amplitude with enough accuracy, resulting in deficient elimination of linear tissue signal. Alternatively, alternated elements in the array can be used to transmit the beam with half the amplitude, but this also results in more pronounced grating lobes for that beam.

To solve both of these problems, three-pulse AM has been proposed. The first pulse is generated by only using the odd elements of the array, the second pulse uses all the elements, and the third pulse uses only the even elements, as illustrated by Figure 3.4. Processing consists of summing the half-element pulses and subtracting the full-element pulse, as illustrated by Figure 3.5.

While the three-pulse AM method seems to be superior to PI in every way, it is worth noting that incoherence between pulsed acquisitions accumulates with the number of pulses. The fewer the pulses, the less degraded by motion the images will become. Especially when combined with other sum or compounding methods, such as coherent compounding, using a lower number of pulses can reduce motion artefacts.

3.3 Beamforming

To perform high frame rate acquisitions, the chosen unfocused transmissions were diverging waves.

Diverging waves can be thought of as focused waves where the focus point lies behind the transducer, and consequently behind the imaged medium. Therefore, the equations that are used are the

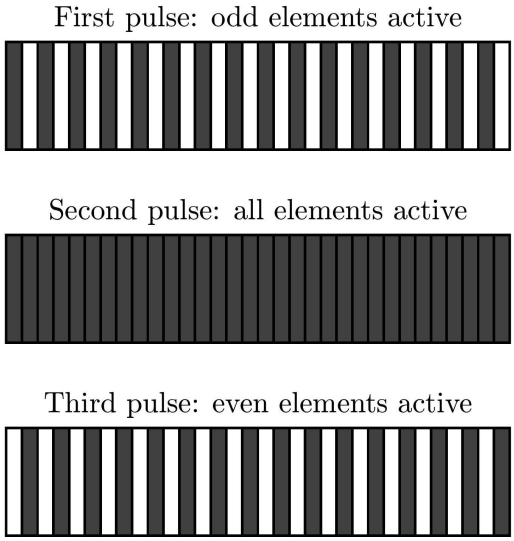

Figure 3.4: Amplitude modulation with three pulses. Only half the transmit aperture is used for the first and third pulses, while the full transmit aperture is used in the second pulse. In reception, the full aperture is always used.

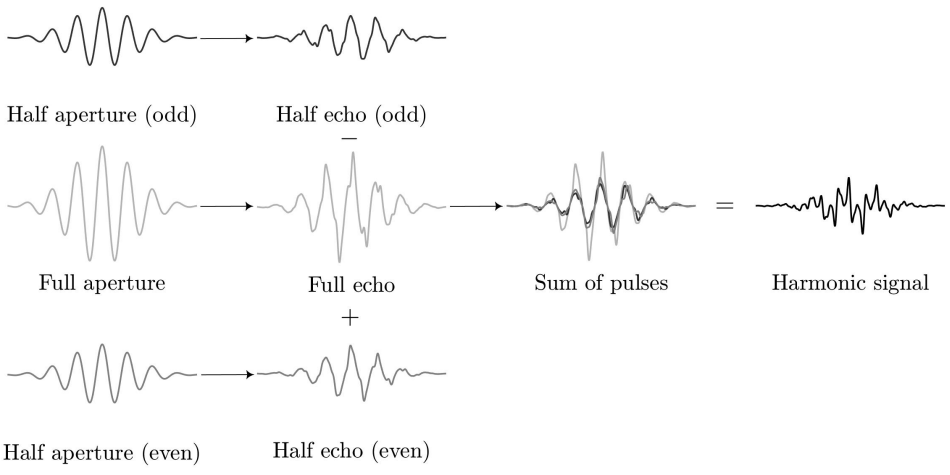

Figure 3.5: Summary of the amplitude modulation technique. Three consecutive pulses are transmitted: the first is generated by driving only the even half of the elements, the second using the full aperture, and the third using the odd half. The first and third echoes are summed and the second echo is subtracted to achieve a harmonic signal.

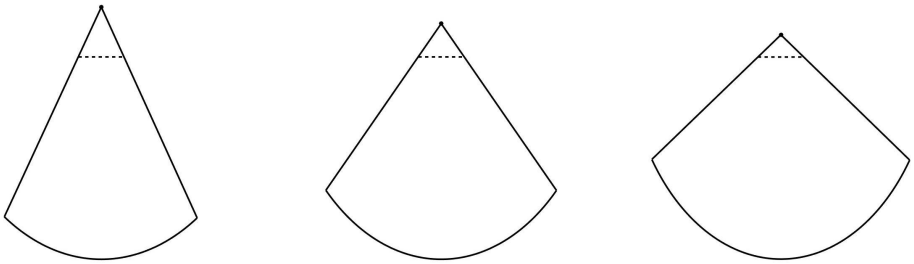

Figure 3.6: Effect of virtual focus distance on the width of the diverging beam. As the distance decreases the beam becomes wider. The dotted line represents the transmit aperture

same ones that are used for focused transmissions - equations 2.24 and 2.25, which are reminded here:

$$\tau_n = t_n - t_k, \;\; t_n = \frac{\sqrt{(np - x_f)^2 + z_f^2}}{c_0}, \;\; k = \arg\min_n \left\{ (np - x_f)^2 \right\}$$

A few more adjustments are necessary to correctly shape a diverging wave. The scan width and the steering angle of the diverging wave are factors which depend on the focus point.

For a desired angular width θ and aperture size L, the location of the focus center of a non-tilted diverging wave is given by equation 3.21.

$$(x_f, z_f) = \left(\frac{L}{2}, -\frac{L}{2\tan(\theta/2)} \right) \tag{3.21}$$

If the focus center is further from the aperture, the angular width is lower. Conversely, if the focus center is closer to the aperture then the beam will become wider. Figure 3.6 illustrates this effect.

In order to steer a diverging wave by an angle α, the position of the focus point must shift in both the x- and z-directions. Consider Figure 3.7 which will aid in determining the coordinates of the focus point (x_f, z_f) in function of the angular width, the tilt angle and the width of the aperture.

For the left right triangle in Figure 3.7, we can write the identity:

$$\frac{x_f}{-z_f} = \tan(\theta/2) \tag{3.22}$$

And for the right triangle on the right side, we can write the following expression:

$$\frac{L - x_f}{-z_f} = \tan(\theta/2 - \alpha) \tag{3.23}$$

If equations 3.22 and 3.23 are used in conjunction to solve for x_f and z_f we obtain:

$$\begin{aligned} x_f &= \frac{L\tan(\theta/2 + \alpha)}{\tan(\theta/2 + \alpha) + \tan(\theta/2 - \alpha)} \\ z_f &= -\frac{L}{\tan(\theta/2 + \alpha) + \tan(\theta/2 - \alpha)} \end{aligned} \tag{3.24}$$

After transmission and reception, the RF data is in the form $RF(n, t)$, where the first coordinate represents the elements, and the second the time. For example, $RF(n = 0, t)$ is the pressure data received by the first element in the array. For any given array element, n and a point in the medium

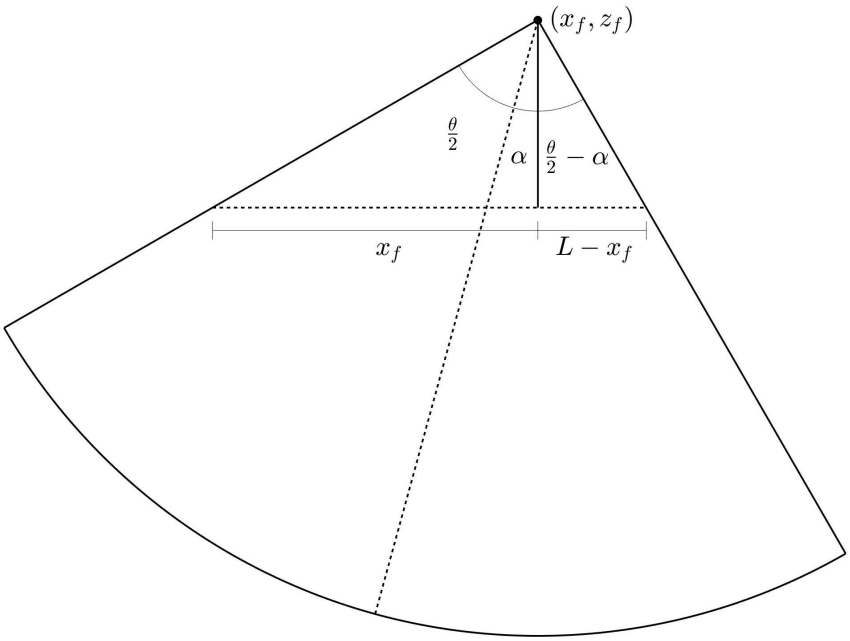

Figure 3.7: Diverging wave of width θ steered at an angle α from a transducer with aperture width L. The point (x_f, z_f) is the virtual focus point of the diverging wave whose coordinates need to be determined.

(x, z), the traveling time of an α-tilted diverging wave to the point is given by:

$$\tau_{em}(\alpha, x, z) = \frac{z\cos\alpha + x\sin\alpha}{c_0} \tag{3.25}$$

The time τ_{em} is specific for the diverging wave geometry. The time the echo takes to return to the same element is simply given by the distance from the point (x, z) to the element:

$$\tau_{rec}(n, x, z) = \frac{\sqrt{z^2 + (x - np)^2}}{c_0} \tag{3.26}$$

The two way travel time is the sum of the forward and backward times:

$$\tau(\alpha, n, x, z) = \tau_{em}^{p} + \tau_{rec} = \frac{z\cos\alpha + x\sin\alpha + \sqrt{z^2 + (x - np)^2}}{c_0} \tag{3.27}$$

For each point (x, z) the contributions from each element signal can be combined to reconstruct the image, $s(x, z)$:

$$s(x, z) = \sum_{n=0}^{N-1} RF(n, \tau(\alpha, n, x, z)) \tag{3.28}$$

Consider now that the center of the array is positioned at $x = L/2$ and we wish to image with a width x_d and depth z_d. If we want to discretize the imaged medium in the lateral direction with N_x points and the depth direction with N_z points, the lateral and depth discretization steps are given by:

$$\begin{aligned} dx &= \frac{x_d}{n_x} \\ dz &= \frac{z_d}{n_z} \end{aligned} \tag{3.29}$$

Given this gridded discretization, the points in which the medium is reconstructed are given by:

$$\begin{aligned} s(k,m) \equiv s(x = \frac{L}{2} - \frac{x_d}{2} + kdx, z = mdz) \\ k = 0,\ 1,\ ...,\ n_x \\ m = 0,\ 1,\ ...,\ n_z \end{aligned} \tag{3.30}$$

The full equation for reconstruction is given by:

$$s(k,m) = \sum_{k=0}^{n_x-1} \sum_{m=0}^{n_z-1} \sum_{n=0}^{N-1} RF(n, \tau(\alpha, n, \frac{L}{2} - \frac{x_d}{2} + kdx, mdz)) \tag{3.31}$$

Note that the points in the space where the image is reconstructed may not result in a time τ that matches a time discretization. To ensure accuracy, interpolation is performed in the RF data.

3.4 Transmission sequences with coded transmission

Coherent compounding can be used in conjunction with coded transmission with PI and AM. There are two possible types of transmission in contrast mode.

One of the ways multipulse contrast imaging can be integrated with coherent compounding is acquiring two/three pulses per angle for PI/AM, respectively. Figure 3.8 shows this transmission sequence for the case of pulse inversion using diverging waves.

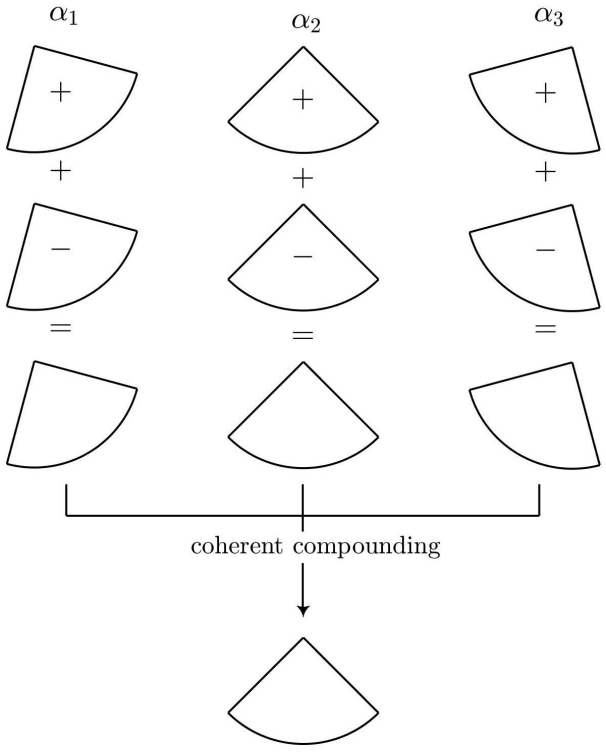

Figure 3.8: Coherent compounding with multiple pulses per angle and pulse inversion. For each angle α, two consecutive pulses in opposite phase are transmitted. These are summed to get a higher-contrast LRI, and only then are the LRIs summed for a coherently compounded image.

The provided example is for PI, but the same principle can be applied in AM.

A different way to acquire contrast images is by integrating the coded transmissions directly in the angle sequence. For PI, that would be transmitting the first angle as a positive pulse and the second angle as a negative pulse, and so on. This imposes the condition of the number of angles being a multiple of two for PI and a multiple of three for AM. Figure 3.9 illustrates a typical alternated angle contrast sequence using pulse inversion and diverging waves.

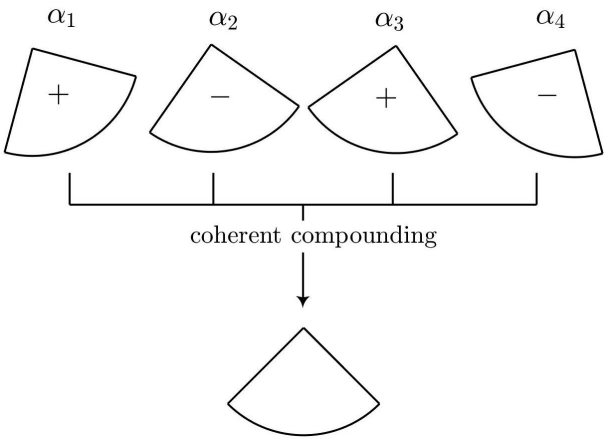

Figure 3.9: Coherent compounding with alternated angle pulse inversion. For each angle α, a single positive or negative pulse is transmitted. The phase of each angled transmission is alternated.

To differentiate between the two types of transmissions, the names angled multipulse contrast coherent compounding and alternated contrast coherent compounding are introduced. The name "contrast" can be substituted by the appropriate technique, namely PI and AM - angled multipulse PI/AM (MultiPI/MultiAM) and alternated PI/AM (AltPI/AltAM). All the possibilities of compensation between LRIs are explored in the next subsections for both types of transmissions.

To perform the simulations, a total of 12 tilted diverging wave transmissions were used, as that number has been shown to be sufficient to achieve good image quality and SNR [10, 46]. The angle spacing was chosen according to Denarie et al. (2013), who proposed the usage of the following expression to determine the angle spacing [4]:

$$\alpha_{step} = \arcsin \frac{\lambda}{L} \tag{3.32}$$

where λ denotes the transmitted pulse wavelength and L the width of the transducer aperture. This angle spacing ensures a resolution similar to conventional US imaging methods.

Three different frequencies were tested in transmission to evaluate the effect of frequency on motion compensation: 1.25 MHz, 1.75 MHz and 2.5 MHz. RF pulses with these frequencies were generated with 4 cycles. The angle spacing thus depends on the transmit frequency. Using $\lambda = c/f$, the corresponding angle spacings using the simulated P4-1 transducer and a reference speed of sound of 1540 m/s are 2.53° , 1.81° and 1.26° , respectively.

Table 3.2 summarizes the transmission parameters used in simulation with diverging waves.

Note that while the usage of 12 angles is equivalent to saying 12 transmissions in the alternated contrast sequence, that is not the case for the angled multipulse contrast sequence since 2/3 pulses

Table 3.2: Summary of the simulated transmission parameters.

Property	Value
Transmit frequency	1.25/ 1.75/ 2.50 MHz
Number of cycles of RF pulse	4
Number of angles	12
Angle step [4]	2.53° /1.81° /1.26°

are used per angle for coded transmission. In MultiPI, a total of 24 transmissions are used, and 36 for MultiAM.

3.5 Motion compensation

To maintain the ability to image at high frame rates, choosing a computationally inexpensive motion compensation scheme is of interest. Given this need, a Doppler motion compensation scheme was evaluated.

3.5.1 The Doppler autocorrelator

The Doppler effect can be described as a frequency shift due to the relative motion between the emitter and the scatterer. In pulsed transmissions, in contrast with continuous ones, determining the frequency shift directly is challenging because of the short duration of the pulses. Instead, if the motions are small enough, the frequency shift can be determined indirectly from the phase shifts between pulses, which themselves can be determined from a lag-one autocorrelator. The Doppler autocorrelator is the most-widely used method to estimate axial velocities in ultrasound imaging. It was first proposed by Kasai et al. in 1985 for conventional ultrasound [76], but has since been adapted for HFR ultrasound imaging too [11].

A derivation of the Doppler autocorrelator for HFR imaging is now presented. Consider the idealized continuous RF data $s(x, z, t)$. Here, x and z are the spatial coordinates. Consider also that each set of RF data can be acquired instantaneously such that at each time instant t there is one image.

The autocorrelator in the time coordinate is written as:

$$r(x, z, t) = s(x, z, t) * s^*(x, z, -t) = \int_{-\infty}^{+\infty} s(x, z, \tau) s^*(x, z, \tau - t) \mathrm{d}\tau \tag{3.33}$$

where the symbol $*$ denotes the convolution operation. When used as a superscript though, it denotes the complex conjugate. The power spectrum of s, $P(\omega)$, is precisely the Fourier transform of its autocorrelator. To prove it, consider the Fourier transform of s to be $S(\omega) = \mathcal{F}\{s(t)\}$, where from now on the dependence on the space coordinates will be made implicit.

$$
\begin{aligned}
P(\omega) &= |S(\omega)|^2 \\
&= S(\omega)S^*(\omega) \\
&= \mathcal{F}\{s(t)\}\mathcal{F}\{s^*(-t)\} \\
&= \mathcal{F}\{s(t) * s^*(-t)\} \\
&= \mathcal{F}\{r(t)\}
\end{aligned}
\tag{3.34}
$$

The mean frequency in the power spectrum is given by the following expression:

$$
\hat{\omega} = \frac{\int_{-\infty}^{+\infty} \omega P(\omega) \mathrm{d}\omega}{\int_{-\infty}^{+\infty} P(\omega) \mathrm{d}\omega} \tag{3.35}
$$

The previous expression can be rewritten in a form where its usefulness is more easily understood:

$$
\hat{\omega} = \frac{\int_{-\infty}^{+\infty} j\omega P(\omega) e^{2\pi j\omega 0} \mathrm{d}\omega}{j\int_{-\infty}^{+\infty} P(\omega) e^{2\pi j\omega 0} \mathrm{d}\omega} \tag{3.36}
$$

The denominator is the inverse Fourier transform of $P(\omega)$ evaluated at $t = 0$, and using the Fourier transform derivative theorem the numerator is the derivative of the inverse Fourier transform of $P(\omega)$ evaluated at $t = 0$. Since the inverse Fourier transform of $P(\omega)$ is $r(t)$:

$$
\bar{\omega} = \frac{\int_{-\infty}^{+\infty} j\omega P(\omega) e^{2\pi j\omega 0} \mathrm{d}\omega}{j\int_{-\infty}^{+\infty} P(\omega) e^{2\pi j\omega 0} \mathrm{d}\omega} = -j\frac{\dot{r}(0)}{r(0)} \tag{3.37}
$$

where dot notation has been introduced to denote differentiation in the time coordinate for simplicity. Let r be written in its polar form:

$$
r(t) = \rho(t)e^{j\phi(t)},\ \rho(t) = \sqrt{\mathrm{Re}\{r(t)\}^2 + \mathrm{Im}\{r(t)\}^2},\ \phi(t) = \arctan\frac{\mathrm{Im}\{r(t)\}}{\mathrm{Re}\{r(t)\}} \tag{3.38}
$$

The derivative of r is written in the following way:

$$
\dot{r}(t) = \left(\dot{\rho}(t) + j\rho(t)\dot{\phi}(t)\right) e^{j\phi(t)} \tag{3.39}
$$

When both $r(t)$ and $\dot{r}(t)$ are evaluated at $t = 0$ they yield:

$$
r(0) = \rho(0)e^{j\phi(0)} \tag{3.40}
$$

$$
\dot{r}(0) = \left(\dot{\rho}(0) + j\rho(0)\dot{\phi}(0)\right) e^{j\phi(0)} \tag{3.41}
$$

Because the autocorrelation, r, is an even function of time, its magnitude, ρ, is also an even function of

time, while its argument ϕ is odd[3]. The derivative of an even function is an odd function, which means $\dot{\rho}$ is odd. Since odd functions are equal to zero at the origin, $\dot{\rho}(0) = 0$. Thus, the mean frequency $\bar{\omega}$ is given by:

$$\bar{\omega} = -j\frac{\dot{r}(0)}{r(0)} = -j\frac{j\rho(0)\dot{\phi}(0)e^{j\phi(0)}}{\rho(0)e^{j\phi(0)}} = \dot{\phi}(0) \tag{3.42}$$

Consider now the more realistic approach where the signal s is sampled in time at integer multiples of the pulse repetition period, which is the inverse of the pulse repetition frequency, $T = 1/\mathrm{PRF}$. From now on, the index n is used to denote the discrete sampling of the signal s at times $t = nT$:

$$s(n) \equiv s(t = nT) \tag{3.43}$$

where n is an integer number. Using the finite difference approximation that the phase of the autocorrelator remains constant between each pulse acquisition, the discrete approximation of $\bar{\omega}$ is:

$$\bar{\omega} \cong \frac{\phi(T) - \phi(0)}{T - 0} \tag{3.44}$$

The fact that r is even imposes that its argument, ϕ, is an odd function of time, indicating that $\phi(0) = 0$, and therefore:

$$\bar{\omega} \cong \frac{\phi(T)}{T} \tag{3.45}$$

For simplicity, everything was derived in angular frequencies. However, it is more practical to use the quantities in ordinary frequencies.

$$\bar{f} = \frac{\bar{\omega}}{2\pi} \cong \frac{\phi(T)}{2\pi T} = \frac{\mathrm{PRF}\phi(T)}{2\pi} \tag{3.46}$$

An expression for the mean frequency in the power spectrum has now been derived. Since the RF signals $s(n)$ are real-valued, from the properties of the Fourier transform, the power spectrum of s is even, and the mean across the entire domain of an even function is zero. Additionally, for a central transmission frequency of f_0, the mean positive frequency of the power spectrum is f_0 as that is the carrier frequency of the information in ultrasound imaging. In order to extract the information from the carrier frequency such that the mean positive frequency of the power spectrum is instead the Doppler shift, the waveforms must be I/Q demodulated at the central frequency f_0. I/Q demodulation is a type of conversion into the analytic signal[4]. The spectrum of the analytic signal has two important features:

1. The amplitude of the spectrum in the negative frequencies is zero;
2. The amplitude of the spectrum in the positive frequencies is doubled.

When the spectrum has these features, the mean frequency across the entire spectrum is the mean positive frequency - which, due to the extraction from the carrier frequency f_0, will be the mean Doppler

[3]Refer to Appendix B.2 for a proof regarding the evenness of complex functions.
[4]Refer to Appendix B.1 for a comprehensive explanation of I/Q demodulation, the analytic signal and the Hilbert transform.

frequency shift. Using I/Q demodulation of s, when N transmissions are used:

$$s(n) = I(n) + jQ(n),\ n = 0, 1, ..., N-1 \tag{3.47}$$

The discrete version of the autocorrelator of s is given by:

$$r(l) = \sum_{n=0}^{N-2} s(n)s^*(n+l) \tag{3.48}$$

From equation 3.45, the phase of the autocorrelator only needs to be evaluated at $t = T$. Given the sampling in 3.43, that is equivalent to $t = nT$ when $n = 1$:

$$\phi(n = 1) \equiv \phi(t = T) \tag{3.49}$$

Evaluating the autocorrelator at $l = 1$ yields the following expression:

$$r(1) = \sum_{n=0}^{N-2} s(n)s^*(n+1) \tag{3.50}$$

The previous expression is named the lag-one autocorrelator. In the context of Doppler ultrasound, this term is synonymous with the term "Doppler autocorrelator". The notation $r_D \equiv r(1)$ is now introduced to denote the lag-one autocorrelator, where the subscript D stands for Doppler. Similarly, $\phi_D \equiv \phi(1)$. Substituting now $s(n)$ by its I/Q demodulated version from equation 3.47:

$$\begin{aligned} r_D &= \sum_{n=0}^{N-2} (I(n) + jQ(n))(I(n+1) + jQ(n+1))^* \\ &= \sum_{n=0}^{N-2} (I(n) + jQ(n))(I(n+1) - jQ(n+1)) \\ &= \sum_{n=0}^{N-2} I(n)I(n+1) + Q(n)Q(n+1) + j(Q(n)I(n+1) - I(n)Q(n+1)) \end{aligned} \tag{3.51}$$

The phase of the lag-one autocorrelator is thus given by:

$$\phi_D = \arctan \frac{\mathrm{Im}\{r_D\}}{\mathrm{Re}\{r_D\}} = \arctan \frac{\sum_{n=0}^{N-2} Q(n)I(n+1) - I(n)Q(n+1)}{\sum_{n=0}^{N-2} I(n)I(n+1) + Q(n)Q(n+1)} \tag{3.52}$$

Equation 3.52 is a close-form approximated solution to the Doppler phase-shift. The axial velocity of the scatterers that produces the frequency shifts can be computed using the classical Doppler equation:

$$v_D = \frac{c\Delta f}{2f_0} \tag{3.53}$$

where Δf is the Doppler frequency shift. Because the mean frequency of the I/Q demodulated power spectrum represents this frequency shift ($\bar{f} = \Delta f$), combining equations 3.46 and 3.53, the Doppler

velocity is given by:

$$v_D = \frac{c\mathrm{PRF}\phi_D}{4\pi f_0} \tag{3.54}$$

Early on in the derivation of the Doppler velocity, the space coordinates were omitted as they were not necessary for the derivation. However, the Doppler autocorrelator is a function of the two space coordinates x and z, and consequently so is its phase, $\phi_D \equiv \phi_D(x,z)$ and the velocity, $v_D \equiv v_D(x,z)$. Hence, axial velocity is estimated at all space points. Of course that in practice, s is a discrete function of the space coordinates as well, and not only time:

$$s(k,m,n) \equiv s(x = kp, z = m\frac{c_0}{f_s}, t = nT) \tag{3.55}$$

where p represents the transducer pitch and c_0/f_s the spatial sampling frequency in the depth direction, with f_s being the sampling frequency of the receiver system. If additional spatial interpolation (or decimation) is needed, then the sampling frequencies shown here might change, but these are the ones as they are receive-beamformed.

Since the entire derivation was carried out without dependence on the space coordinates, it follows that axial velocity estimation does not depend on the type of grid that is used (i.e., Cartesian, polar, etc). However, the term "axial" does have different meanings depending on the geometry of the transmission that is used. The axial velocity is the component of the velocity parallel to the direction of transmission, so axial velocity profiles of the same motion may be different if different transmissions are used.

3.5.2 Doppler motion compensation

Motion compensation in coherent compounding aims at estimating motion between LRIs and correcting each of them before summation, ensuring coherence.

Given a set of N LRIs, each acquired with an unfocused transmission at a different transmit angle, the axial velocity can be estimated using equations 3.52 and 3.54. The axial velocity is estimated with the assumption that the phase of the autocorrelator remains constant during a pulse repetition period, which is equivalent to saying that the axial velocity profile remains constant throughout the acquisition. Using this approximation, the axial displacement amplitude is itself constant between acquisitions and is given by the product of the axial velocity and the time between each acquisition:

$$u_D = \frac{v_D}{\mathrm{PRF}} = \frac{c\phi_D}{4\pi f_0} \tag{3.56}$$

Under the same assumption, the motion between one LRI and a different LRI in the same sequence is an integer multiple of u_D. There are two steps to ensure a coherent sum [4]:

1. Axial displacement compensation;
2. Phase correction.

By picking one of the LRIs for reference, such as the middle one, axial displacement compensation can be performed as a spatial shift in the axial coordinate, z, and the phase correction as a product with a complex exponential of the Doppler phase shift:

$$\widetilde{s}(x,z,n) = s\left(x, z + \left(n - \frac{N}{2}\right) u_D, n\right) e^{jn\phi} \tag{3.57}$$

Compounding with built-in MoCo can be written in the form:

$$S(x,z) = \sum_{n=0}^{N-1} \widetilde{s}(x,z,n) = \sum_{n=0}^{N-1} s\left(x, z + \left(n - \frac{N}{2}\right) u_D, n\right) e^{jn\phi} \tag{3.58}$$

$$f_{dem} = 2f_0 \tag{3.59}$$

3.5.3 Multiple angle transmit sequence ordering

The ordering of the transmit sequence has a significant impact on the coherently compounded images [4, 11]. Because a triangular transmit sequence ordering suppresses sidelobes the most, that is the sequence that is used. The angle sequence ordering is illustrated in Figure 3.10. The triangular

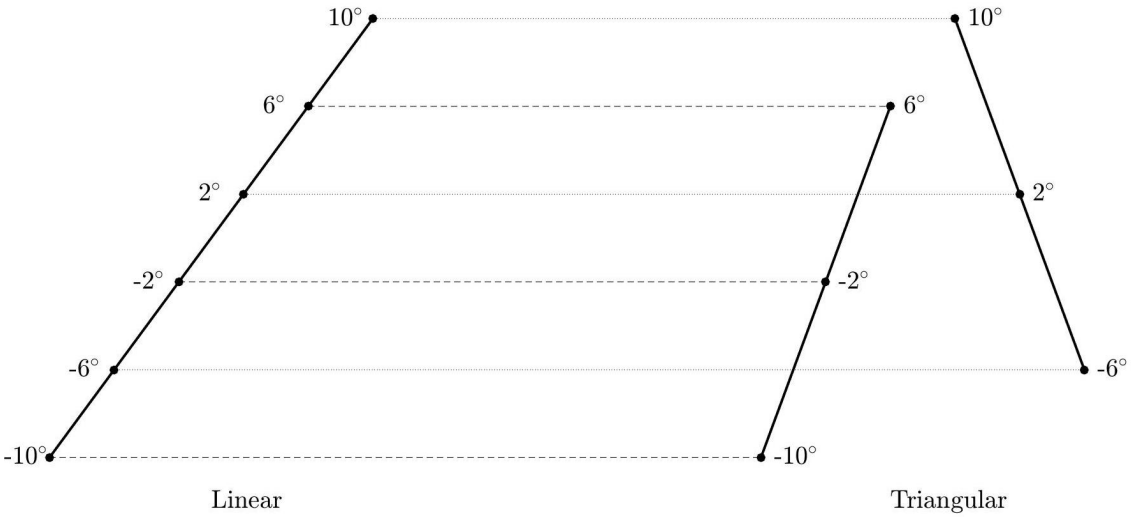

Figure 3.10: Standard linear angle sequence compared with a triangular sequence. The same angles are used, bur ordered in a different manner.

sequence can be interpreted as two consecutive sequences of angles: the first one ascending and the second one descending. This ordering is preferential for Doppler motion compensation schemes, as side lobe influence is suppressed [11] during motion estimation. Motion estimation is adjusted by using one lag-one autocorrelator for the ascending sequence of images and another one for the second sequence. The estimated Doppler phase shift is the mean of the ascending and descending autocorrelator phases, ϕ_D^A and ϕ_D^D:

$$\phi_D = \frac{\phi_D^A + \phi_D^D}{2} \tag{3.60}$$

A disadvantage of this approach is that aliasing occurs at half the classical Doppler velocity limit, making this methodology more prone to aliasing.

3.5.4 Compensation in contrast mode

Motion compensation in angled multipulse contrast mode

Given the pulse sequence of angled multipulse contrast mode, there are three possibilities for Doppler MoCo between LRIs:

1. Sum the contrast pulses without compensating and compensate motion only between the angled transmissions - MoCo C;
2. Compensate between contrast pulses, sum them, and then compensate the resulting angled transmissions separately - MoCo B;
3. Compensate between all the LRIs directly - MoCo A.

The letter notation (i.e., MoCo A/B/C) is introduced to refer to each motion compensation scheme in a more compact form. Figures 3.11-3.13 show the simplified pipelines of the motion compensation schemes.

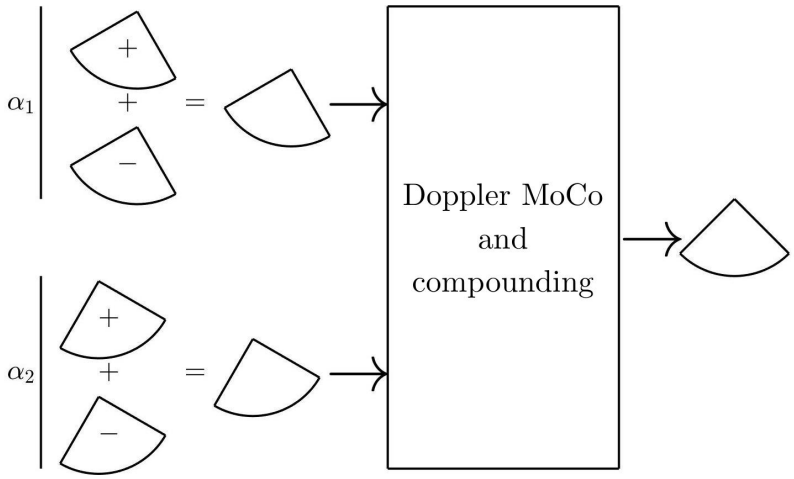

Figure 3.11: MoCo C: The coded transmission pulses are summed and compensation is performed between the compounding angles.

Motion compensation in alternated contrast mode

The alternated contrast mode sequence can be treated as a non-contrast sequence and compensated using Doppler MoCo. Since coded transmission is embedded directly in the angle sequence, no additional processing is required. Figure 3.14 summarizes the motion compensation pipeline.

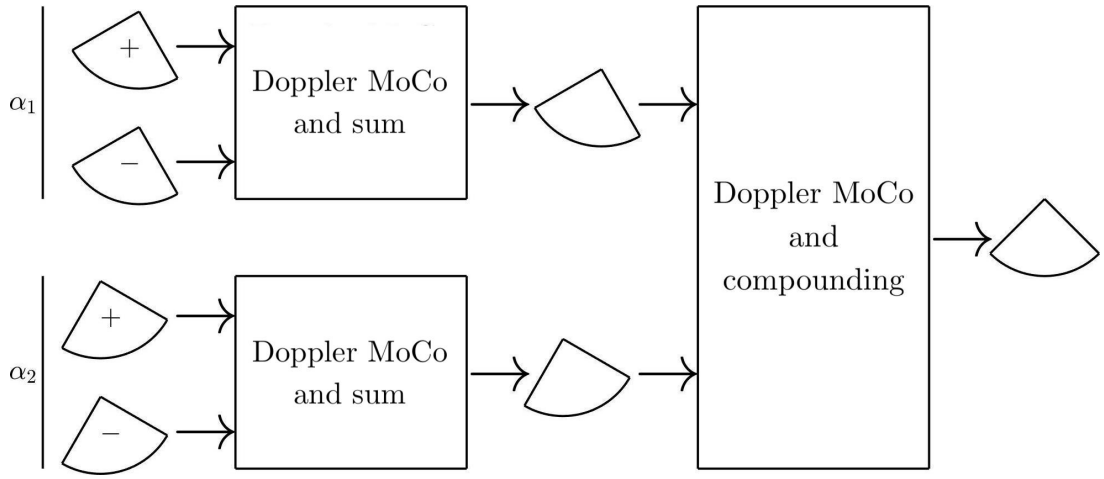

Figure 3.12: MoCo B: Motion is compensated between coded transmission pulses and then between the compounding angles.

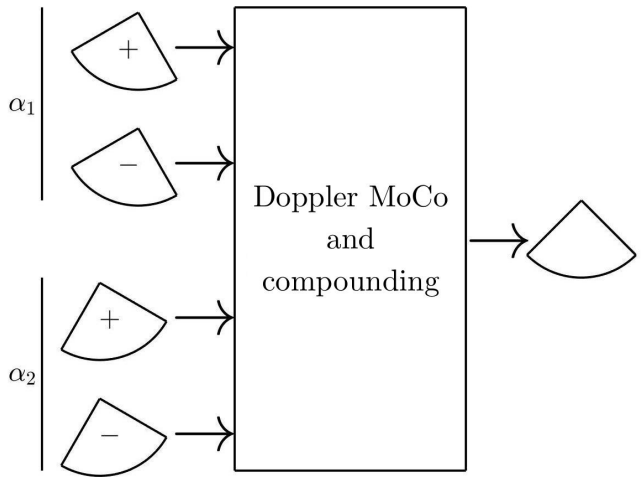

Figure 3.13: MoCo C: Motion compensation is performed between all pulses directly, independently of the angle at which they were transmitted.

3.6 Image display

3.6.1 Envelope detection

Because the acquired RF data is zero-mean, if images are generated for display directly with RF data, the negative half cycles of high-amplitude echoes would appear as dark and the the corresponding positive half-cycles would appear as bright, despite being generated from a strong scatterer. The oscillatory behaviour of RF data inherently makes it unfit for display. Instead, if the positive envelope of the data is used, then dark regions will correspond to weak or absent scatterers and bright regions to strong scatterers.

If a signal is amplitude modulated into another signal of higher frequency (as is the case of US imaging), the envelope of the full waveform can be determined using the absolute value of the analytic signal of the waveform [77].

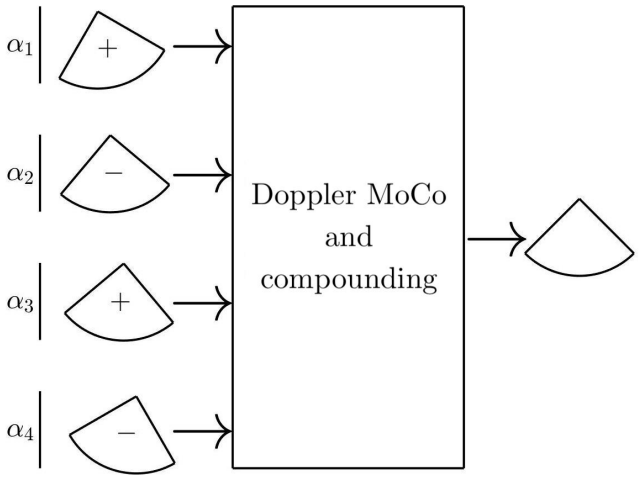

Figure 3.14: Alternated contrast motion compensation scheme.

Given an amplitude modulated signal $s(t)$, its corresponding analytic signal, $\hat{s}(t)$ is given by:

$$\hat{s}(t) = s(t) - j\mathcal{H}\{s(t)\} \tag{3.61}$$

where the operator $\mathcal{H}\{\cdot\}$ denotes the Hilbert transform. The envelope of $s(t)$ is given by:

$$\text{envelope}\{s(t)\} = |\breve{s}(t)| = \sqrt{\breve{s}(t)\breve{s}^*(t)} \tag{3.62}$$

Further insights on the Hilbert transform and analytic signals can be found in Appendix B.1.

3.6.2 Log-compression

To increase the dynamic range of the images, they were converted to decibel scale, using the convention of $20\log_{10}(e(x,z))$, where $e(x,z)$ represents the envelope of the beamformed RF data. The logarithm in the dB scale reduces the differences in intensities in the image. The original amplitudes can be in very different orders of magnitude (up to 10^5 factors of differences) and these are reduced to tens of dB in this scale.

3.7 Evaluation metrics

3.7.1 Disc measurements

To validate the accuracy of simulation, the radii of the disc and cysts must be measured. To ensure no compounding or motion artefacts influence the measurements, they are performed directly on LRIs in a static condition, and the mean across all of them is computed. Measurements are performed by counting the number of pixels that belong to a certain region. The number of pixels can be converted to centimeters, since the dimensions of the pixels corresponds to the dimensions of grid points used in beamforming, which are known.

MATLAB has a built-in function which makes measurements easier, the `drawcircle` function. By providing one image and the corresponding sizes, in centimeters, of the depth and lateral axes, one can manually draw a circle on top of the region to be measured, and the radii is automatically computed given the size of the FOV.

3.7.2 Contrast-to-noise ratio

Contrast-to-noise ratio is used to evaluate the level of contrast between regions of different echogeneity. In the case of the rotating disc with anechoic inclusions, CNR is computed between the region of the disc and the region of the cysts. The equation used for computation of CNR is the one presented below:

$$\text{CNR (dB)} = 20 \log_{10} \frac{|\mu_{cyst} - \mu_{disc}|}{\frac{1}{2}\sqrt{\sigma_{cyst}^2 + \sigma_{disc}^2}} \tag{3.63}$$

where μ represents the mean in the region and σ the standard deviation in the same region.

To ensure a fair estimation of CNR, the contrast between the cysts and the disc must be evaluated in regions with the same total area. The map for computation of CNR is shown in Figure 3.15.

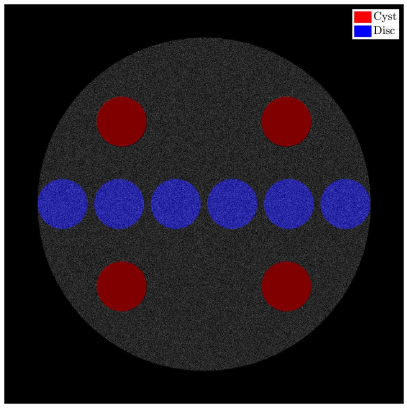

Figure 3.15: Location map for computation of CNR. The red regions correspond to the cysts and the blue regions correspond to the disc.

CNR is computed between each cyst and the six disc regions across the lateral dimension, generating a total of 24 CNR measurements, for which the mean is taken. Since signal loss occurs along the lateral direction due to the higher axial velocities, measuring the CNR along multiple regions is more sensible than choosing a region in the center, for example.

3.7.3 Lateral evaluation of loss of intensity

In coherent compounding, signal intensity is lost where motion is present. The larger the velocity of motion, the higher the loss in signal intensity. Since the axial velocity increases in the lateral direction, a way to evaluate loss of signal intensity with increasing velocity is by evaluating the mean intensity in the disc in the lateral axis. To perform this, the lines of the image corresponding to the disc are averaged in the depth direction. For each image line, one point of mean intensity intensity is obtained. The points

are plotted according to their location in the lateral axis, producing a mean plot of mean lateral intensity. Figure 3.16 illustrates this type of plot.

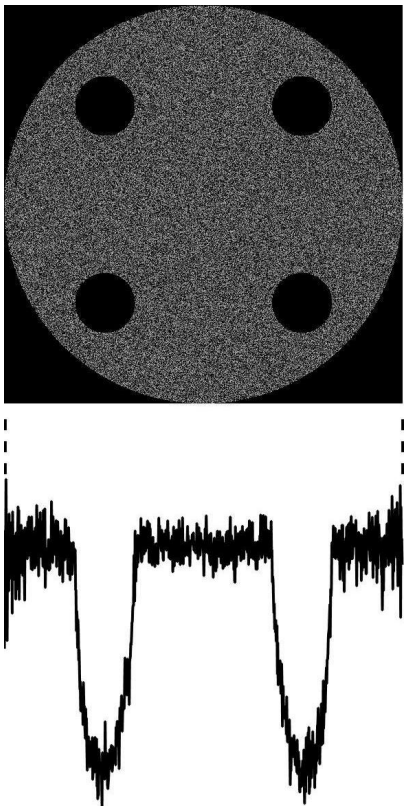

Figure 3.16: Rotating disc (Top) and mean intensity plot across the lateral axis (Bottom)

3.7.4 Doppler velocity maps

Using the Doppler equation 3.54, the velocity of the disc can be evaluated at all points in space. Given the rotation motion, the theoretical axial velocity profile for a diverging wave transmission is the one presented in Figure 3.17.

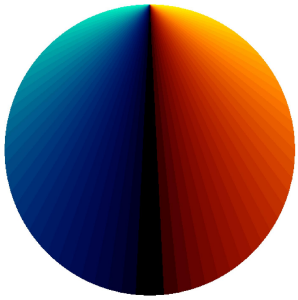

Figure 3.17: Axial velocity profile in a rotating disc using a diverging wave transmission. Cold colours signify negative velocities and warm colours positive ones.

The velocity profiles provide a direct measurement of the accuracy of the motion compensation method, since the ground truth is known.

The normalized mean square error was computed between the estimated velocity profiles and the theoretical one using the following expression:

$$\text{NRMSE } (\%) = 100 \frac{\sqrt{\frac{1}{N_x N_z} \sum_{k=1}^{N_x - 1} \sum_{m=1}^{N_z - 1} (v_D(k,m) - v_T(k,m))^2}}{v_{max}} \tag{3.64}$$

where N_x and N_z are the number of pixels in the axial and depth directions, respectively, v_D is the estimated Doppler velocity, v_T the theoretical velocity profile and v_{max} the theoretical maximum axial velocity in the disc.

Chapter 4

Results

In this section the motion compensation results are presented first for MultiPI/MultiAM and second for AltPI/AltAM, including the evaluation metrics. Afterwards, a comparison of the Doppler velocity maps of all MoCo schemes is presented.

4.1 Disc and cyst measurements

The disc and cysts were measured according to section 3.7.1. Measurements were performed for all acquisitions in static condition. Table 4.1 displays the mean measured dimensions of the disc, the top cysts and the bottom cysts across all LRIs:

The simulation disc phantom had a radius of 25 mm and the cysts a radius of 3.75 mm. The percent differences in relation to the real dimensions were calculated and are presented in Table 4.2:

4.2 Angled multipulse contrast motion compensation

The rotating disc phantom acquired with an angled multipulse PI/AM sequence was motion compensated with schemes A, B and C. Figures 4.1 and 4.2 show the finalized images after envelope detection and log-compression for MultiAM and MultiPI, respectively. The first column of images represent the static disc, for which no compensation was performed. The second, third and fourth columns represent

Table 4.1: Mean radii measurements of the disc and cysts in different simulation conditions. Measurements in millimeters.

	Frequency	Disc	Top Cysts	Bottom Cysts
AM	1.25 MHz	24.92 ± 0.02	3.10 ± 0.05	3.40 ± 0.03
	1.75 MHz	24.94 ± 0.02	3.21 ± 0.04	3.51 ± 0.02
	2.50 MHz	24.96 ± 0.01	3.29 ± 0.02	3.70 ± 0.02
PI	1.25 MHz	24.97 ± 0.02	3.26 ± 0.02	3.71 ± 0.01
	1.75 MHz	24.99 ± 0.02	3.56 ± 0.01	3.72 ± 0.01
	2.50 MHz	25.00 ± 0.01	3.69 ± 0.01	3.74 ± 0.01

Table 4.2: Mean radii measurements of the disc and cysts in different simulation conditions. Measurements in centimeters.

	Frequency	Disc	Top Cysts	Bottom Cysts
AM	1.25 MHz	0.32 %	17.33 %	9.33 %
	1.75 MHz	0.24 %	14.40 %	6.40 %
	2.50 MHz	0.16 %	12.27 %	1.33 %
PI	1.25 MHz	0.12 %	13.07 %	1.07 %
	1.75 MHz	0.04 %	5.07 %	0.80 %
	2.50 MHz	0.00 %	1.60 %	0.27 %

the moving disc compensated with MoCo schemes A, B and C, respectively. The fifth column shows the same moving disc with no motion compensation applied. The static and uncompensated images serve as controls. Each row in the figure represents a MultiPI/MultiAM acquisition using a certain transmit frequency. The first and second rows represent acquisitions at 1.25 MHz, the third and fourth at 1.75 MHz and the fifth and sixth at 2.5 MHz.

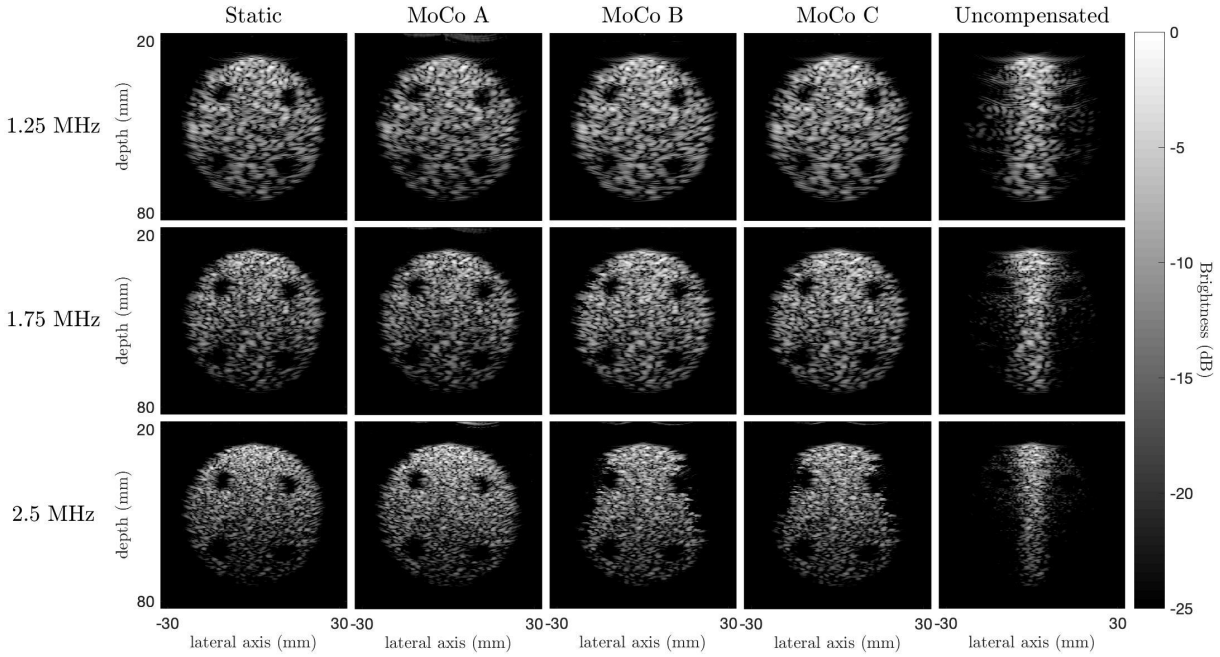

Figure 4.1: Motion compensation in a rotating disc acquired using a MultiAM contrast sequence at multiple transmit frequencies.

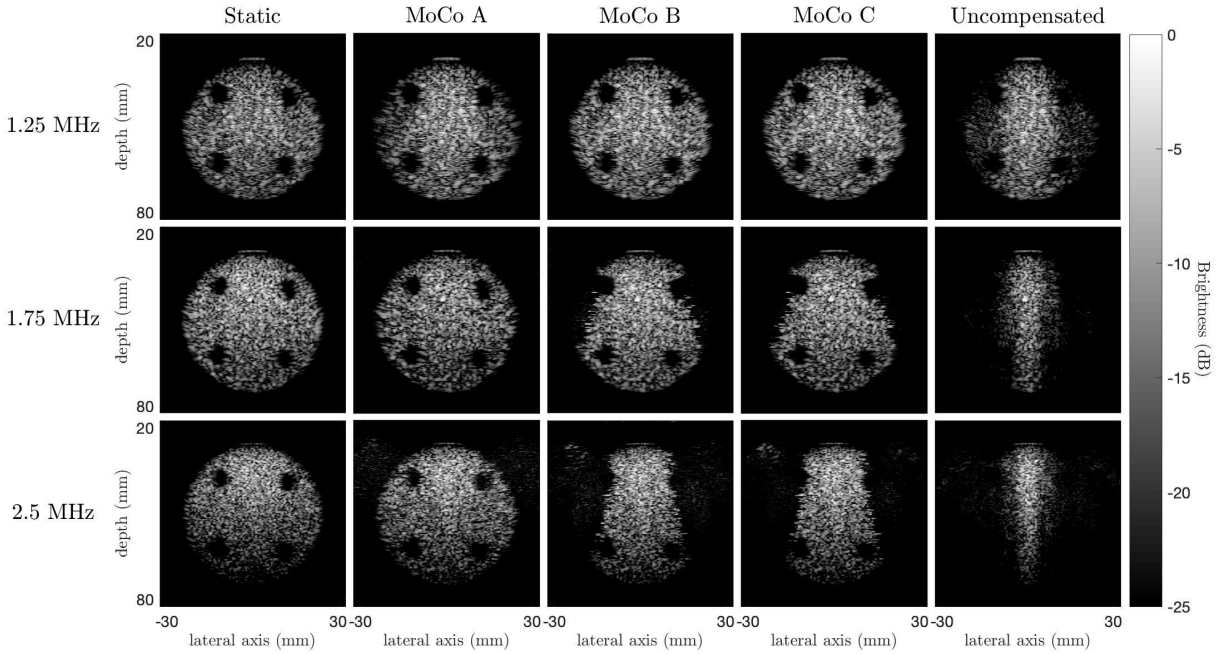

Figure 4.2: Motion compensation in a rotating disc acquired using a MultiPI contrast sequence at multiple transmit frequencies.

Figure 4.3 shows the computed CNRs for all simulated cases in the form of a bar chart. There are six groups of bars, one for each combination of frequencies and contrast modes (MultiPI/MultiAM). For each group, five CNR bars are presented. From left to right, these are: Static, MoCo A, MoCo B, MoCo C and Uncompensated.

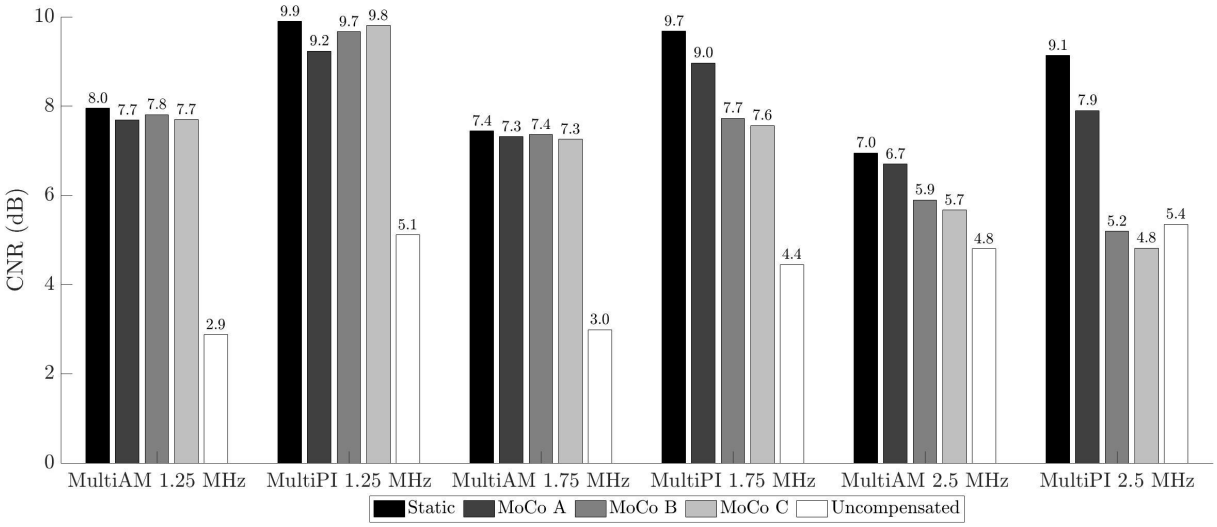

Figure 4.3: CNR measurements in angled multipulse contrast mode for the static condition, motion compensated conditions A,B and C, and the uncompensated condition at multiple transmit frequencies.

Lateral intensity loss/recovery was evaluated and results are presented in Figure 4.4. Each row of plots represents a transmit frequency and each columns represents a contrast mode. Each subplot includes the mean lateral intensity of the static condition, motion compensated conditions A, B and C, and the uncompensated condition.

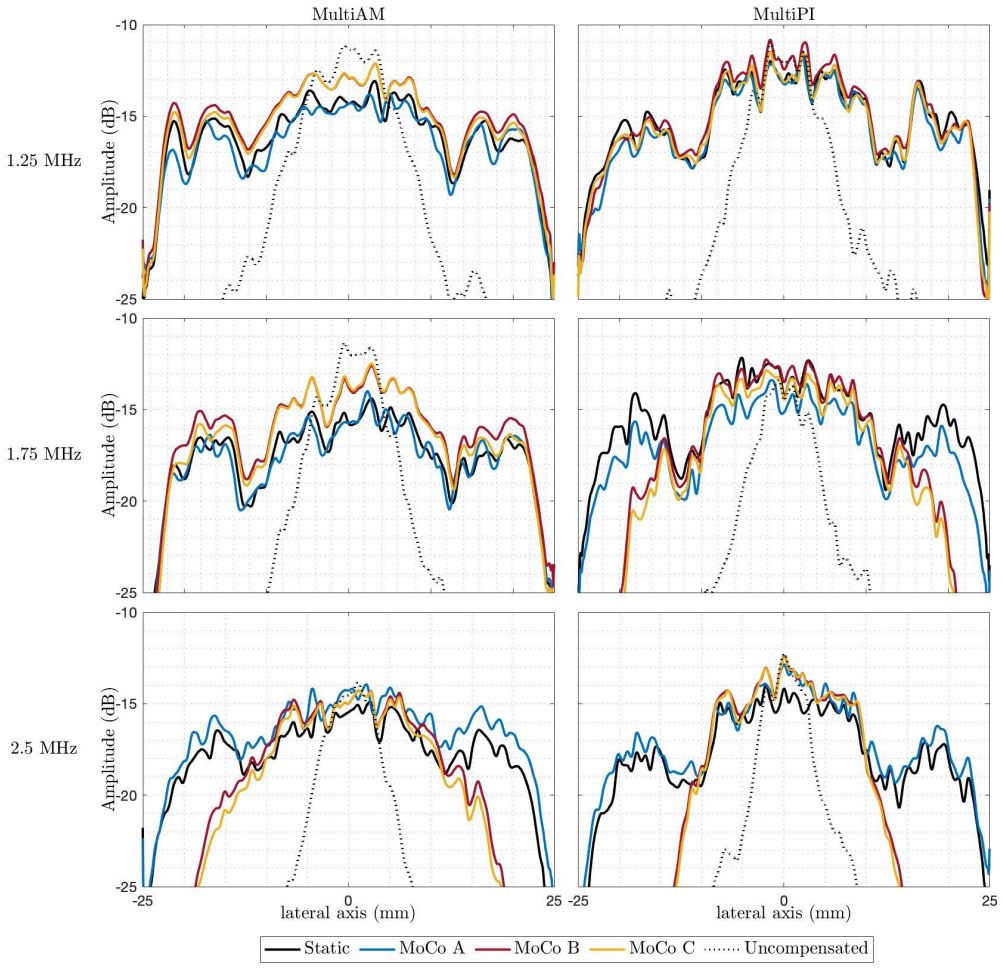

Figure 4.4: Mean lateral intensity in angled multipulse contrast mode for the static condition, motion compensated conditions A,B and C, and the uncompensated condition at multiple transmit frequencies.

4.3 Alternated contrast motion compensation

Using an alternated contrast sequence, several acquisitions using different transmit frequencies were performed. Similarly to Figures 4.1-4.2 for the angled multipulse contrast sequence, Figures 4.5-4.6 shows the finalized images for the alternated contrast mode in the static condition, the motion compensated condition and the uncompensated condition.

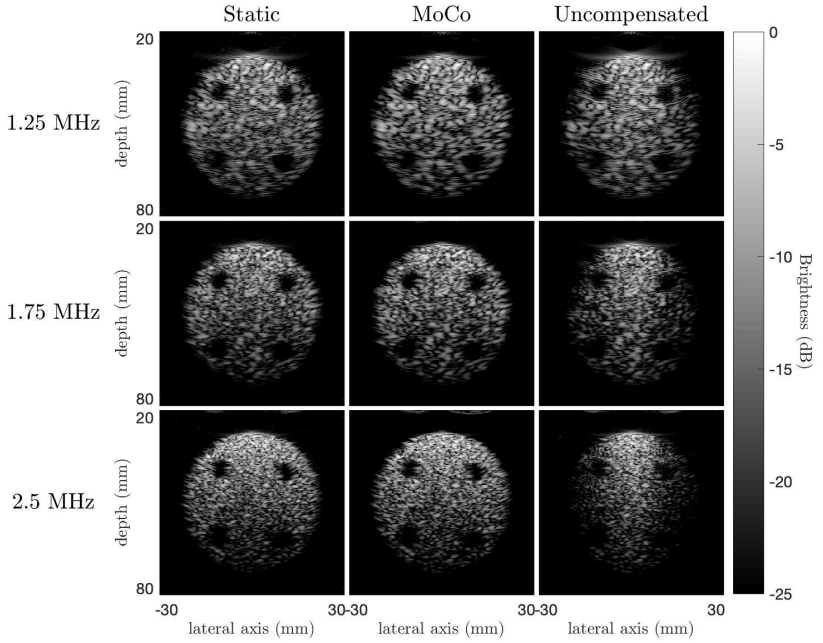

Figure 4.5: Motion compensation in a rotating disc acquired using an alternated contrast sequence at multiple transmit frequencies.

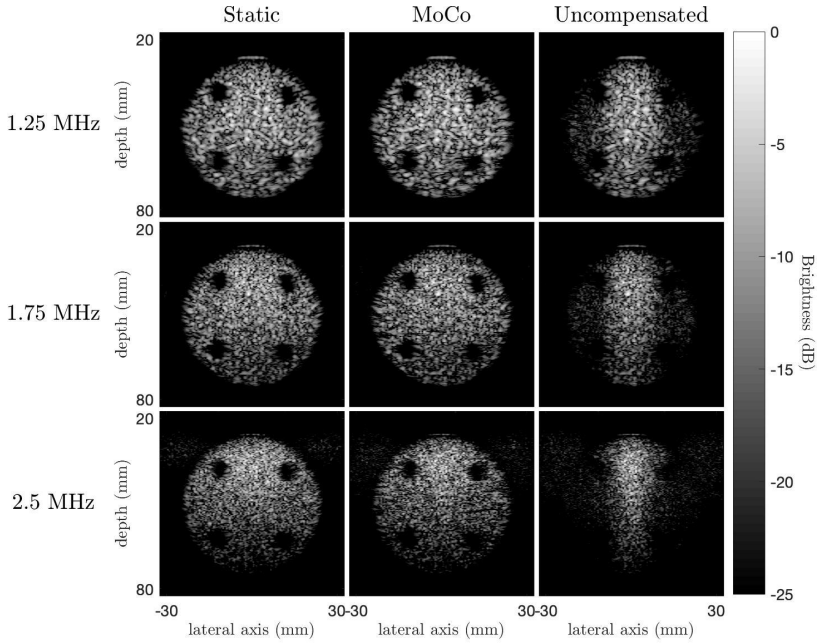

Figure 4.6: Motion compensation in a rotating disc acquired using an alternated contrast sequence at multiple transmit frequencies.

CNR measurements and mean lateral intensity measurements for the alternated contrast sequences were performed the same way as the angled multipulse contrast sequences and are presented in Figures 4.7 and 4.8, respectively.

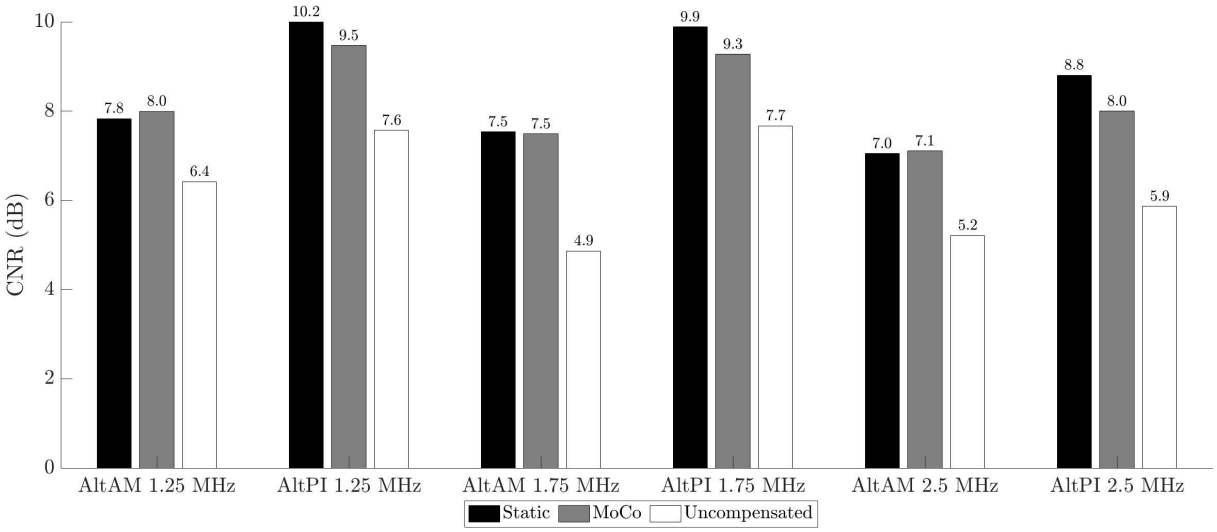

Figure 4.7: CNR measurements in alternated contrast mode for the static condition, motion compensated condition, and the uncompensated condition at multiple transmit frequencies.

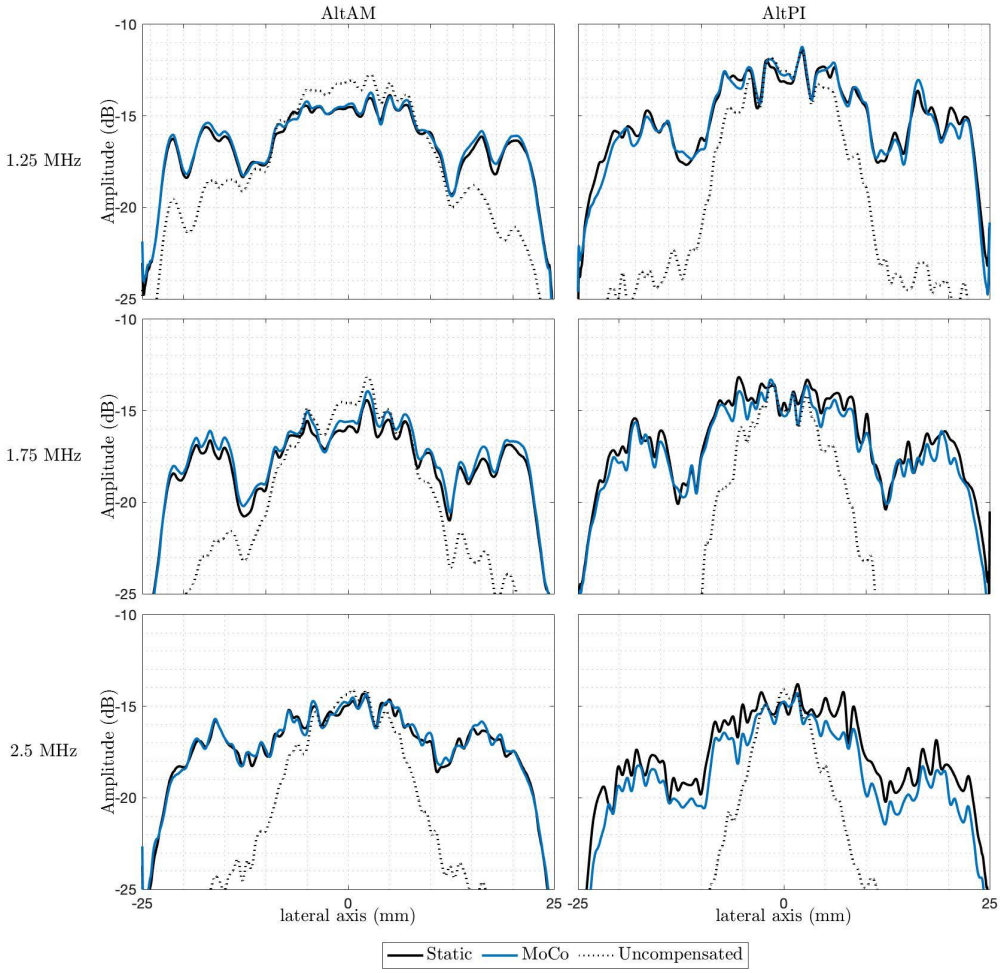

Figure 4.8: Mean lateral intensity in alternated contrast mode for the static condition, motion compensated condition, and the uncompensated condition at multiple transmit frequencies.

4.4 Doppler velocity maps

The rotating disc velocity maps computed with the Doppler equation, 3.53, are shown in Figure 4.9 for all motion compensation methods explored - all three methods in angled multipulse contrast and the one method in alternated contrast, with both PI and AM transmissions at three different transmit frequencies.

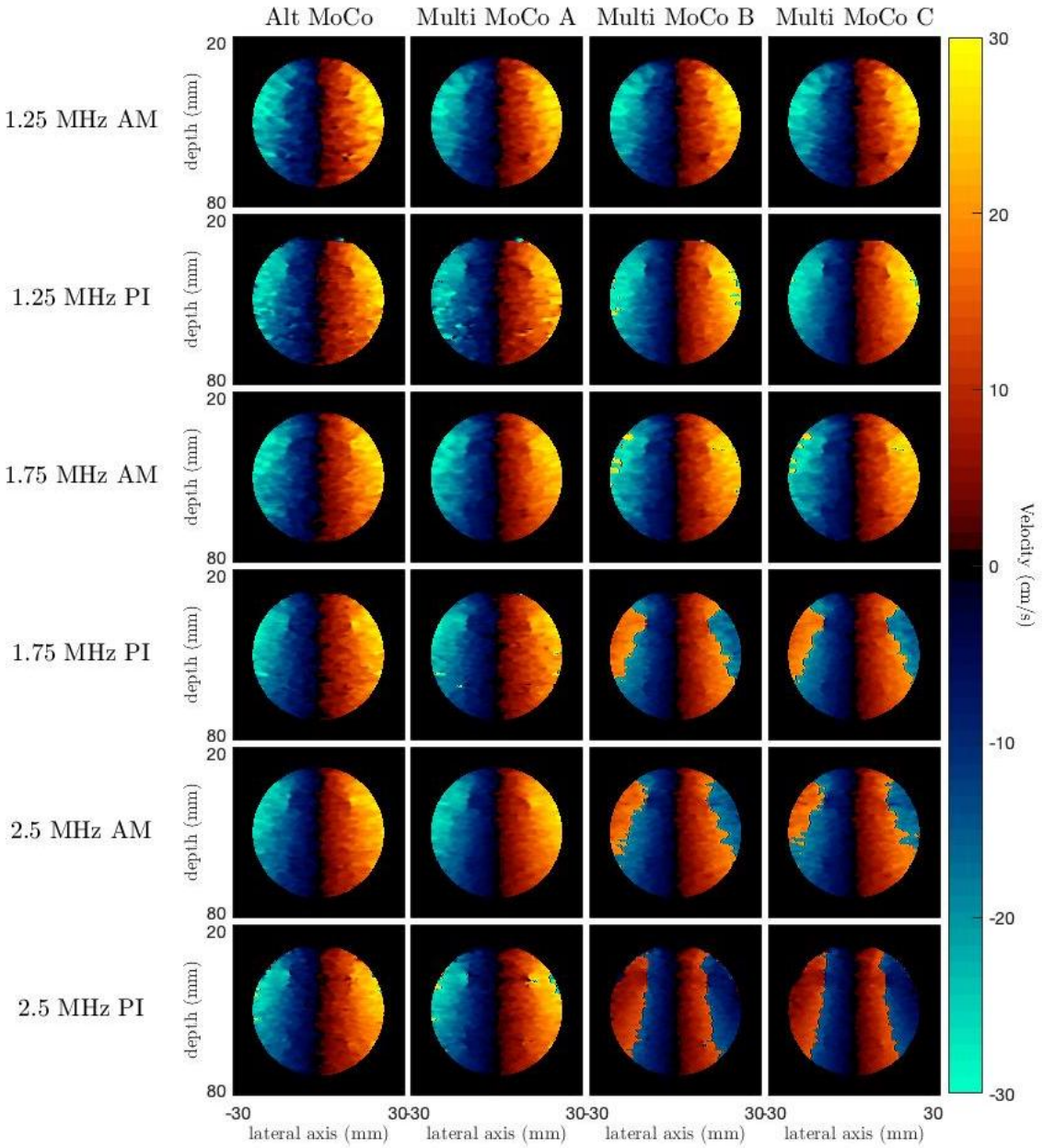

Figure 4.9: Axial velocity profiles for different transmit frequencies, contrast modes and motion compensation methods.

The percent normalized root mean square errors computed in reference with the theoretical velocity profiles are presented in Table 4.3:

Table 4.3: NRMSE of the Doppler velocity measurements in all simulations.

	Alt MoCo	Multi MoCo A	Multi MoCo B	Multi MoCo C
1.25 MHz AM	5.44 %	5.53 %	4.94 %	4.97 %
1.25 MHz PI	6.48 %	9.73 %	12.79 %	8.99 %
1.75 MHz AM	4.52 %	4.34 %	14.13 %	12.63 %
1.75 MHz PI	5.07 %	6.89 %	41.51 %	41.42 %
2.50 MHz AM	4.44 %	4.16 %	40.63 %	38.72 %
2.50 MHz PI	8.97 %	15.25 %	42.04 %	41.70 %

Chapter 5

Discussion

During this chapter the results presented in Chapter 4 will be discussed. Observations will be made about all the results and explanations for the observations will be provided based on the existing literature regarding the topic or, in case of unsatisfactory or missing information in current literature, conjectures will be formed.

This chapter begins with a validation of the simulation data to ensure the results gathered from said data are meaningful. Next, the motion compensation schemes for both transmission sequences will be discussed in detail, explaining the differences between them and highlighting their advantages and disadvantages. Afterwards, special care is taken to analyse the influence of Doppler aliasing in the results, how it affects motion compensation and what schemes are favourable and why. This chapter is finalized with a concise comparison of all investigated motion compensation methods, highlighting in what circumstances each should or could be used, followed by the limitations of this work.

5.1 Simulation accuracy and validation

The results which will provide a baseline for evaluation of simulation accuracy and subsequent validation will be the measurements of the disc and cysts in Tables 4.1 and 4.2, and the images in Figures 4.1 - 4.2 and 4.5 - 4.6 corresponding to the static disc. These should resemble the sound speed map phantom shown in Figure 3.1.

The dimensions and location of the disc match the medium phantom with deviations from the real value lower than 1 %. However, the dimensions of the cysts have varying errors depending on the conditions of the simulation. In fact, the relative errors in the dimension of the cysts seem to decrease with increasing transmit frequency, are lower for the bottom cysts and are also lower in PI when compared to AM. All three of these factors can be explained by the effect of sidelobes. Sidelobe signal is generated most prominently in boundaries between regions with large differences in echogeneity, which is the case in the disc/cyst boundary. Figure 4.1 support this hypothesis, as some sidelobe signal from the disc can be seen "bleeding" into the cyst region, mainly in the lateral direction. This explains why the bottom cysts' radius suffer less from this effect and their measurements are closer to reality. Sidelobe signals

are weaker than mainlobe signals, and just like mainlobe signals these are attenuated as they propagate [78]. An already weak signal like the sidelobe is greatly attenuated as it reaches the depth of the lower cysts, so much so that the dynamic range of -25 dB is not enough for it to appear in the image. Furthermore, attenuation also increases with the transmit frequency, hence why the errors at larger frequencies are smaller, and why errors in PI are smaller than errors in AM - PI uses the 2^{nd} harmonic frequency, so for the same transmit frequency, the imaged frequency in PI is double the imaged frequency in AM.

From the static images, it is clear that the image brightness is higher at lower depths and lower at higher depths. This is a result of ultrasound signal attenuation. A property of ultrasound signal attenuation is that it is frequency dependent: the larger the frequency, the larger the attenuation [79]. Consider the static rows in Figure 4.1. As the frequency increases, the brightness of the images is lower at the same depth, illustrated by the intensity of each image at the bottom of the disc (highest for 1.25 MHz, lowest for 2.5 MHz). This effect is also visible in the PI images in Figure 4.2

Another property of images acquired with ultrasound that is frequency dependent is the resolution [80]. Again, by analysing the static case in Figures 4.1 and 4.2, it is apparent that single scatterers are more easily resolved for the higher frequencies. Specifically, the resolution of PI images is always higher than AM images at the same transmit frequency due to the usage of the second harmonic.

Taking now attention to the uncompensated rotating disc images in Figures 4.1 and 4.2, it is observed that image intensity is lost at the edges of the disc and maintained in the center. This is in line with motion studies performed with similar in-vitro phantoms [11, 51]. Since the axial velocity increases laterally from the center, the regions where loss of intensity is higher are the regions where the axial velocity is higher - the lateral edges of the disc.

The previous analysis demonstrates that well known properties of ultrasound propagation in tissue apply to the simulated medium phantom, explaining any observed differences between the phantom and the images. It also validates the simulated data as sufficiently close to similar in-vitro phantoms, allowing one to gather conclusions from motion studies performed with the simulation data that can translate to real data, whether it is in-vitro or in-vivo.

5.2 Overview of angled multipulse contrast motion compensation

The MultiAM/MultiPI sequences for HFR CEUS provide three distinct ways of compensating motion, which are now discussed.

From Figures 4.1 and 4.2, one finds that the images compensated using all three methods yield similar motion compensation results for 1.25 and 1.75 MHz in MultiAM and 1.25 MHz in MultiPI. For the higher frequencies in the corresponding contrast method, significant motion artefacts can be observed in images compensated with MoCo B and C, while the MoCo A scheme remains robust independent of frequency. This phenomenon is most easily observed in Figure 4.4, where the mean lateral intensity is plotted. It is clear that at 2.5 MHz in MultiAM and 1.75-2.5 MHz in MultiPI the lateral intensity nearer the edges is not recovered for MoCo B/C, while the lateral intensity profile of MoCo A is very similar to the static disc.

Burden of Doppler aliasing

The phenomenon that leads to poor intensity recovery in motion compensation schemes B and C is Doppler aliasing. This phenomeon is characterized by a "wrapping around" of the estimated velocities. To better illustrate how it occurs, consider the Doppler autocorrelator in its complex exponential form:

$$r_D(x,z) = |r_D(x,z)|e^{j\phi_D(x,z)} \tag{5.1}$$

The phase of the autocorrelator has values in the interval $[-\pi, \pi]$. The Doppler velocity equation can be rewritten in terms of the wavelength, by making the substitution $\lambda = c/f_0$:

$$v_D = \frac{c\mathrm{PRF}\phi_D}{4\pi f_0} = \frac{\mathrm{PRF}\phi_D\lambda}{4\pi} \tag{5.2}$$

The previous equation is maximized when the Doppler phase is $\phi_D = \pi$:

$$v_{D\max} = \frac{\mathrm{PRF}\lambda}{4} \tag{5.3}$$

Or, in terms of the displacement, $u_D = v_D/\mathrm{PRF}$:

$$u_{D\max} = \frac{\lambda}{4} \tag{5.4}$$

Equation 5.4 highlights the physical limits of the Doppler autocorrelator as a phase-domain method. It tells us that displacements larger than a fourth the wavelength within one pulse repetition period are not susceptible to be correctly estimated by the Doppler autocorrelator. When that happens, the estimated phase surpasses π, and due to the periodicity of the complex exponential in equation 5.1 the phase wraps around by an amount equal to the difference between the estimated phase and π. For example, if for a given PRF and f_0 the maximum Doppler velocity is 30 cm/s (corresponding to a phase of π), and there is motion in the medium with velocity of 45 cm/s, the measured phase of this larger velocity will be 1.5π. In the interval $[-\pi, \pi]$, that corresponds to a phase of -0.5π, which using the Doppler equation will yield a velocity of -15 cm/s.

Due to this wrapping around effect of Doppler aliasing, aliasing is easily identifiable in the velocity maps in Figure 4.9 by looking for large discontinuities. In fact, large discontinuities can be found in the velocity maps of the images where lateral intensity recovery is poor, as initially postulated. For MoCo B and C, when aliasing occurs, the NRMSE is extremely high - with values on the order of 40% - and also increases with frequency.

Since the maximum Doppler velocity decreases with frequency, the effects of aliasing become more drastic as frequency increases. Doppler aliasing leads to destructive sums since each LRI is often compensated according to velocities in the opposite direction of the actual motion, further contributing to incoherence.

Why does aliasing occur in MoCo B and C but not in MoCo A? In MoCo A, motion is estimated directly between all the consecutive pulses, while in MoCo B/C that is not the case. In MoCo B, the LRIs corresponding to the coded transmission are corrected first, and only then is correction performed

between the angled transmissions. After compensation of the coded transmissions, one LRI per angle is obtained. Coded transmission is compensated using one of the pulses as a reference (the positive pulse for PI or the middle pulse for AM). Since this is performed for all angles, the obtained LRIs after the first stage of MoCo are equivalent to the corresponding postive pulse/middle pulse in its sequence. The time between transmission of two positive pulses in a PI sequence is $2/\mathrm{PRF}$, and two middle pulses is $3/\mathrm{PRF}$, so in essence the PRF is reduced for the second stage of motion compensation. For MoCo B/C, the maximum Doppler velocity is reduced by a factor of 2/3 in PI/AM, respectively, hence the differences in the velocity maps between MoCo A and MoCo B/C.

Additionally, the MultiPI sequence aliases more drastically than the MultiAM sequence for the same transmit frequency. That is because the frequency at which motion compensation is performed is the second harmonic for PI, further reducing the maximum Doppler velocity by a factor of 2. The limits for Doppler aliasing, adjusted for each method, are thus given by:

$$v_{D\max}\left(\mathrm{MultiAM\ B/C}\right) = \frac{\mathrm{PRF}}{3}\frac{c}{4f_0} = \frac{c\mathrm{PRF}}{12f_0} \tag{5.5}$$

$$v_{D\max}\left(\mathrm{MultiPI\ B/C}\right) = \frac{\mathrm{PRF}}{2}\frac{c}{4\times 2f_0} = \frac{c\mathrm{PRF}}{16f_0} \tag{5.6}$$

Note that the maximum Doppler velocity is further reduced by half by the usage of the two-autocorrelator approach combined with the triangular transmit sequence.

Contrary to MoCo schemes B and C, MoCo A keeps a high PRF by using a single motion compensation stage that estimates motion using all pulses in the sequence. No aliasing can be observed in the velocity maps of MoCo A in Figure 4.9. This leads to up to 5 dB higher lateral intensity recovery in MultiAM and up to 8 dB increases in MultiPI according to Figure 4.4. Moreoever, the CNR of MoCo A is 0.8/1 dB larger than aliased MoCo B/C, respectively in MultiAM, and 2.7/3.1 dB larger than aliased MoCo B/C, respectively in MultiPI.

While aliasing is the phenomenon that explain most of the observed differences between the MoCo schemes in MultiPI/AM, there are a few more observations that should be taken into account. More specifically, the number of LRIs that are used to estimate motion greatly influence the success of motion compensation.

The derivation of the Doppler autocorrelator for motion estimation in section 3.5.1 was carried out assuming infinite duration signals. The expression for the mean Doppler frequency in equation 3.45 only holds for infinite duration signals. In practice the signals used must have finite duration, but sufficiently good approximations can be achieved with a finite number of time points. The more time points are used, the closer the approximation will be. In this case, one time point corresponds to one transmitted pulse. It follows that the accuracy of Doppler MoCo increases with the number of pulses used for motion estimation.

MoCo A estimates motion between a total of 24 LRIs for PI and 36 for AM, while MoCo B estimates

motion in the first stage between 2/3 pulses for PI/AM, respectively, and between 12 LRIs in the second stage for both. MoCo B estimates motion between only 12 LRIs. A few predictions can be gathered from these numbers directly:

1. Since MoCo A always used a larger number of pulses to estimate motion, it should compensate it more accurately than MoCo B/C;
2. Because the first MoCo stage of MoCo B uses a very small number of pulses for estimation, this step should result in almost negligible compensation; While it should compensate better than MoCo C, these methods should be very similar;
3. For MoCo A, compensation in MultiAM should be superior to compensation in MultiPI due to it using a larger number of pulses.

The first prediction is corroborated by the results of mean lateral intensity in Figure 4.4. The mean lateral intensity of MoCo A follows the static control more closely than the remaining methods. In the regions where aliasing does not occur, the lateral intensity of MoCo B and C are higher than MoCo C, but with larger differences from the static reference.

The second point is also verified in the lateral intensity recovery plots. The mean intensity of the discs compensated with MoCo B and C coincide across most of the lateral axis, with MoCo B being slightly closer to the static disc - differences no larger than 1 dB.

The third and final point is also verified: for the same transmit frequency, the mean lateral intensity of the disc compensated with MoCo A is closer to the static configuration in MultiAM when compared to MultiPI. This is also true for the CNR, as the differences in contrast are no larger than 0.3 dB across all frequencies in MultiAM, but can be as large as 1.2 dB in MultiPI.

To finalize the analysis of the angled multicontrast sequence, sidelobe suppression is noteworthy. Indeed, in the MultiAM acquisitions at 1.25 MHz and 1.75 MHz, large sidelobe signal can be observed at the top of the static discs, and to a lesser degree at the top of the static discs. These sidelobes are greatly suppressed during motion compensation, especially when MoCo A is used. This is in agreement with Porée et al. (2016), who demonstrated that the usage of a two-autocorrelator approach in conjuction with a triangular transmit sequence greatly reduces sidelobes [11]. The presented results demonstrate that it still applies in CEUS. Furthermore, the obtained results show that the negative effects of sidelobes is generally reduced as the transmit frequencies increase. The 2.5 MHz AltAM sequence has barely visible sidelobes only in the uncompensated disc (on top) and top sidelobes are simply absent in AltPI acquisitions. Sidelobes within the disc region are harder to identify, but the absence of large sidelobes on top suggests larger suppression as the transmit frequency increases due to the larger attenuation as the wave propagation [78].

5.3 Overview of alternated contrast motion compensation

The AltPI/AltAM sequences for HFR CEUS provides a way to compensate motion equivalent to non-contrast HFR ultrasound imaging.

In Figures 4.5 and 4.6, which show the contrast images in static, compensated and uncompensated conditions, we first turn our eyes to the uncompensated images. It is clear that loss of intensity is not as drastic compared to MultiPI/MultiAM. That can be attributed to the fact that a much smaller number of total pulses are used in AltPI/AltAM. The fewer the number of pulses, the less incoherence accumulates due to motion.

Similarly to MoCo A in MultiPI/MultiAM, the motion compensated discs are qualitatively very similar to the corresponding static ones, with approximately equal brightness distributions across the depth and the lateral axis for MultiAM. In MultiPI, despite the full disc being visible, small brightness discrepancies can be observed near the lateral edges of the disc between the static configuration and the compensated configuration.

The CNR comparisons provided in Figure 4.8 highlight the full contrast recovery of the motion compensated disc in AltAM, where the CNR of the MoCo disc are at least as high as the CNR in the static disc. In the AltPI acquisitions the contrast recovery is not total, with differences to the static disc ranging from 0.6 to 0.8 dB. However, the level of contrast that is recovered is on the order of 2 dB, when compared to the uncompensated discs. This level of recovery matches the level of recovery achieved in MultiAM in absolute terms, but since the base contrast of AltPI is up to 2 dB higher too, the recovered contrast in MultiPI is not as high relatively. The measured CNR of the alternated contrast sequences are on the same level of the angled multipulse contrast sequences despite the much smaller number of total transmitted pulses. This can be attributed to the fact that all pulses in AltPI/AltAM are acquired at a different angle. Pulses acquired with transmissions in slightly different directions further decorrelate noise distributions during compounding. Not only does this generate better CNR directly by reducing the level of noise, but can also aid in more precise motion estimation using the Doppler autocorrelator, which improves contrast indirectly by correctly aligning the anatomical structures such that they sum coherently.

Figure 4.8 exhibits the mean lateral intensity for the AltPI/AltAM acquisitions. The plots corresponding to the motion compensated disc are almost coincident with the static disc, with the maximum observed differences to be around 1 dB (albeit rare) for all acquisitions except the 2.5 MHz AltPI one, which is the largest imaged frequency with the second harmonic at 5 MHz. This larger frequency is the one that is most attenuated, and thus the level of signal is the lowest of all acquisitions. As the signal decreases, the SNR increases, especially in PI since the second harmonic signal is weaker. This hypothesis can be is supported by the noise observable in the images of the AltPI acquisition at 2.5 MHz. Significant random noise is observed in the background region. Since the same level of noise was added to the phantom independently of location, it is expected that the same level of noise is present in the disc region, but it is harder to identify it. Noise can lead to imperfect motion estimation and ultimately motion artefacts with loss of intensity and contrast. Indeed, independently of the type of sequence used (angled multipulse contrast/alternated contrast), the CNR is consistently worse as the frequency increases. The mean lateral intensity of the motion compensated discs also increasingly deviate from the static disc as the transmit frequency increases. The frequency range at which the acquisitions were performed are too limited to gather any further conclusions about the poorer performance of the motion compensation

schemes with larger transmit frequencies. Further dedicated research on the topic with a wider range of frequencies is necessary to reach meaningful conclusions. High frequency ultrasounds have very limited applications due to their poor penetration, and thus comparative studies on the SNR of low and high frequency ultrasounds are still lacking.

On the topic of noise, it is important to note that the larger the number of pulses summed, the lower the level of noise due to averaging. Notably, despite the alternated sequence always having a smaller number of total pulses than the angled multipulse contrast sequence, the achieved contrast in AltPI/AltAM is on the same level of MultiPI/MultiAM, even in static conditions. This characteristic can be attributed to the fact that all AltPI/AltAM pulses are acquired at different angle, which is not the case for MultiPI/MultiAM. Acquiring all LRIs at a different angle ensures sidelobe incoherence across all pulses. The Doppler motion compensation approach tends to rephase sidelobes [4, 11], so keeping them largely incoherent ensures the intensity in the compensated image is as close as possible to the static image. Additionally, transmitting all pulses in different transmit angles further decorrelates random noise, improving the CNR and SNR [2, 40].

The measured axial velocities are in line with what is expected in a rotating disc phantom acquired with diverging wave transmissions. [11, 35, 45, 51]. The NRMSE of Doppler velocity estimates is always under 10%, and seems to decrease with frequency in AltAM, while no clear pattern can be seen in MultiPI. The NRMSE is also slightly lower in AM, highlighting the more accurate compensation in this mode, which is also line with the other evaluation metrics. It is worth noting that an 8.97 % NRMSE is oberved in AltPI at 2.5 MHz. This increased error arises from a very small degree of aliasing that occurs at that frequency. Using the Doppler velocity estimation limit in equation 5.3, and taking into account that this limit is halved by the usage of the two-autocorrelator approach, we determine that the maximum detectable velocity is 29.6 cm/s. Since the maximum velocity in the disc is in fact 30 cm/s, a very small level of aliasing occurs in this acquisition. For the same transmit frequency, an abnormally high error can also be observed in MultiPI, further corroborating this hypothesis.

The alternated contrast motion compensation scheme bears many similarities with the MoCo approach by Porée et al. (2016), which was implemented in non-contrast mode with very positive results [11]. While compensating motion in contrast-mode presents more challenges than B-mode imaging, comparing the results of the two is still relevant, especially because the motion phantoms used are analogous. The achieved results are very similar - motion compensation was successful with intensity recovery across the entire lateral direction of the disc, axial velocity profiles congruent with the theoretical expectations, and contrast recovery close to the levels of the static case. The computed NRMSE are also extremely close. From this preliminary study with simulated data, we take that Doppler MoCo using contrast agents may thus be as accurate as Doppler MoCo in B-mode images if the transmissions sequences are optimized. Further investigation in in-vitro data is necessary to fully validate this methodolody.

5.4 Overview of the evaluated parameters and comparisons

This section intends to summarize the differences, advantages and disadvantages of the studied parameters: contrast sequences (Multi/Alt), contrast modes (PI/AM), transmit frequency, and motion compensation methods.

Motion compensation schemes for angled multipulse CEUS - A, B and C

From the previous analysis, it became clear that one of the motion compensation schemes is superior - MoCo A. The Doppler aliasing limit for MoCo A is much higher than both MoCo B and C due to the preserved PRF, making this scheme ideal for imaging regions with high velocity motions. When no aliasing occurs, all schemes have similar CNRs, but that quickly breaks down once aliasing exists. Additionally, because compensation is performed between all LRIs directly, the infinite signal approximation applies better to MoCo A, yielding intensity recovery very close to the static level. Since the sequence used for transmission is the same for all these methods and the only thing that changes is the motion compensation scheme, there is no advantage to using MoCo B or C, as MoCo A is superior in every way.

Angled multipulse contrast sequence *versus* Alternated contrast sequence

Having established that MoCo A is the preferred scheme in MultiAM/MultiPI, we now compare MoCo A in its contrast mode with the MoCo scheme used in AltAM/AltPI. Both methods possess the same Doppler aliasing limit and yield similar levels of CNR. The MoCo scheme in alternated contrast has the advantage of reaching a mean lateral intensity closer to its corresponding static condition when compared to MoCo A and its respective static condition. More importantly, in alternated contrast the number of ultrasound transmissions is a fraction of the transmissions used in angled multipulse contrast as it integrates coded transmission directly in the angle sequence. Using a smaller number of transmissions increases the frame rate by 2-fold in PI and 3-fold in AM, making it very attractive for imaging regions with fast displacements.

Amplitude Modulation *versus* Pulse Inversion

Both pulse inversion and amplitude modulation yield very good motion compensation results. However, amplitude modulation has one key advantage: it retains the fundamental signal of the contrast agents, which is stronger than the second harmonic. The fundamental frequency has the advantage of suffering less from attenuation, which helps maintain a high SNR. Moreover, compensation is generally more accurate in amplitude modulation. Pulse inversion on the other hand has much greater resolution and the CNR is consistently higher than amplitude modulation to an appreciable level. Qualitatively, the images acquired with PI resemble the imaged object more due to the higher resolution. Using the second harmonic has the additional advantage of greatly weakening sidelobe signal. There is no clear superior contrast method. AM may be more appropriate to image deeper regions due to lower attenua-

tion and also structures with very fast motions due the higher aliasing limit. Otherwise, images acquired PI seem to be higher quality and more resembling of the anatomical structure.

5.5 Limitations

To conclude the discussion chapter, the limitations of the implemented methods will be examined. Two classes of limitations will be discussed in this section:

1. Limitations of using simulation data compared to in-vitro/in-vivo data;
2. Limitations of the motion compensation methods.

Limitations of simulation data

One of the biggest challenges in contrast-enhanced ultrasound imaging is the accurate modelling of microbubbles and their interactions. While many models relying on the Rayleigh-Plesset equation have been proposed to accurately describe asymmetric microbubble expansion, contraction and rupture in liquids [7, 60–62], the existing models are only able to model interactions of a single microbubble. The complexity of the existing models makes inter-microbubble interactions a very big challenge. Keeping this in mind, the best approximation that currently exists to simulate signal generating from microbubbles is the non-linear wave equations by adjusting the non-linearity parameter B/A to the measured values of microbubbles in high concentrations. While comparative studies of the accuracy of this approach in generating signals emulating microbubbles are lacking, the largely unpredictable behaviour of microbubbles leads us to believe that this methodology cannot fully grasp microbubble signal [81]. For this very reason, one must be cautious before making parallels between simulation data and real acquisitions in contrast-enhanced ultrasound imaging.

Another limitation of the simulation data is the fact that all simulations were carried out in two-dimensions. While ultrasound images are reconstructed to achieve a 2D dataset, acquisitions are carried out in 3D volumes. The presence of additional scatterer outside the imaging plane generates unwanted signal components which can reduce image quality. Additionally, the presence of out-of-plane motions provides an additional challenge for motion compensation [10, 52], and axial velocity Doppler methods are not suitable to compensate these types of motions [46].

Limitations of the motion compensation methods

While Doppler motion compensation using axial velocity estimation can greatly reduce the prevalence of motion artefacts, there are several limitations to this approach.

The first and least important source of inaccuracy arises from the fact that only the axial component of the velocity is compensated, while the lateral component remains uncompensated. Full 2D motion compensation provides an additional level of compensation, which can enhance coherence in compounding

methods [10, 51, 55]. However, it has been extensively demonstrated that axial velocity estimation is sufficient to achieve accurate motion compensation [4, 11, 82].

The factor that does influence the results of motion compensation tremendously is the average-motion estimation approach. The assumption that the velocity profile remains constant throughout the acquisition implies that Doppler methods estimate the average motion in a sequence of images. While this assumption is generally reasonable in most cases, it quickly breaks down in the presence of of rapidly changing motion patterns. One case where this occurs is echocardiography, where two distinct phases of motion of the heart can be considered - systole and diastole [83]. To ensure that motion compensation is accurate in echocardiography, acquisitions must be performed synchronized with the heart beat, making sure that there is no overlap of the two phases of motion during a full angle sequence in the acquisition.

Chapter 6

Conclusions

In this chapter, the main conclusions drawn from the obtained results are discussed, and possible future developments to optimize the performance of the methods are outlined.

6.1 Achievements

This work investigated unfocused ultrasound coded transmission sequences with the goal of optimizing Doppler motion compensation schemes in coherent compounding HFR CEUS. Within this scope, two types of transmission sequences were formulated: angled multipulse contrast, and alternated contrast. In angled multipulse contrast three motion compensation schemes were investigated: MoCo A, B and C, while a single motion compensation scheme was evaluated in alternated contrast mode. Many conclusions drawn from the results are shared among the two transmission sequences. First, the accuracy of motion compensation is dependent on the transmission frequency. For the investigated frequencies of 1.25, 1.75 and 2.5 MHz, the results of motion compensation were better at the lower frequencies, highlighted by the higher CNRs and lower differences of mean lateral intensity when compared with the static configuration. Additionally, motion compensation is consistently more accurate in AM when compared to PI, as lateral intensity and CNR recover to levels closer to the static configuration. Despite this, the baseline contrast in PI is higher than AM, likely due to the diminished influence of sidelobes. The results suggest that using lower transmit frequency enhances Doppler motion compensation, and also that motion compensation is more accurate in AM when compared to PI.

In angled multipulse contrast, the Doppler aliasing limits are considerably lower when compensation is not performed between all LRIs directly due to the effective PRF being a fraction of the transmission PRF. Contrary to MoCo B and C, MoCo A maintains a high PRF by compensating between all LRIs. This allows the aliasing limit to be 2/3 times higher than B and C in PI/AM, respectively. Despite the improved aliasing limit of MoCo A, the angled multipulse contrast sequence is inferior to the alternated contrast sequence. Not only is the motion compensation slightly more accurate, with slightly higher CNR and lateral intensity recovery, but the number of necessary transmissions is a fraction of the number used in angled multipulse contrast. The lower number of transmissions allows a higher frame rate which in turn

enables the visualization of anatomical structures with higher temporal resolution.

The employed motion compensation schemes were shown to perform similarly to Doppler motion compensation schemes in non-contrast mode, fulfilling the main objective of this work, which was to adapt existing Doppler motion compensation schemes to HFR CEUS.

6.2 Future Work

Despite the fulfilment of the objectives of this work, several steps need to be taken before it can be used in in-vivo data. Given that this study was performed exclusively in simulation data, the first step would be to reproduce the same acquisitions in-vitro. The rotating disc phantom with anechoic inclusions can be reproduced with tissue-mimicking materials [11]. The transmission sequences used here would be recreated in-vitro using the same parameters, and receive-beamforming, motion compensation and evaluation need to be beamformed in the same way. If the same findings are identified, accounting for the limitations of the simulation data, then the transmission sequences and corresponding motion compensation schemes stand fully validated. After validation in-vitro, the same studies can be performed in more challenging motion compensation problems in-vivo, such as echocardiography, from which the feasibility of the motion compensation schemes in that context can be evaluated.

Another area in which the implementation can be improved is code optimization for real-time imaging. The motion compensation scheme was implemented using MATLAB's built-in `gpuarray` memory structures, which allow GPU-accelerated computations of many MATLAB functions. However, the code can be further optimized by writing it to take it account the GPU architecture. In this case, a NVIDIA GeForce GTX 980 Ti GPU was used, and thus writing the motion compensation code in optimized CUDA code[1] can lead to a significant increase in computation times, which consequently may enable the usage of the motion compensation scheme in real-time.

While the main purpose of this work was not to evaluate the effect of the transmit frequency on motion compensation schemes, several connections between the transmit frequency and the performance of Doppler motion compensation schemes were identified. To further understand and describe these connections, additional studies must be performed, ideally with a larger range of transmit frequencies and also at multiple imaging depths, such that the effects of frequency-dependent attenuation in the performance of motion compensation are also identified.

Finally, this study avoided the effects of Doppler aliasing using lower transmit frequencies and optimizing the transmission sequences and motion compensation methods such that the effective pulse repetition frequency remained high. However, in some cases, Doppler aliasing can still have destructive effects in motion compensation. Anti-aliasing methods inspired in staggered-PRF radar have been investigated in HFR US [35], but are yet to be implemented in HFR CEUS. Anti-aliasing methods can help acquire high-quality images of blood vessels with fast flows and it would hence be interesting to investigate their performance wehn applied to HFR CEUS.

[1] CUDA is a parallel computing platform and programming model developed by NVIDIA for usage with their GPUs. CUDA takes advantage of the GPU architecture to optimize parallelizable code such that it runs as fast as possible.

Bibliography

[1] R. Smith-Bindman, M. L. Kwan, E. C. Marlow, M. K. Theis, W. Bolch, S. Y. Cheng, E. J. A. Bowles, J. R. Duncan, R. T. Greenlee, L. H. Kushi, J. D. Pole, A. K. Rahm, N. K. Stout, S. Weinmann, and D. L. Miglioretti. Trends in Use of Medical Imaging in US Health Care Systems and in Ontario, Canada, 2000-2016. *JAMA*, 322(9):843–856, 09 2019. ISSN 0098-7484. doi: 10.1001/jama.2019.11456. URL `https://doi.org/10.1001/jama.2019.11456`.

[2] G. Montaldo, M. Tanter, J. Bercoff, N. Benech, and M. Fink. Coherent plane-wave compounding for very high frame rate ultrasonography and transient elastography. *IEEE Transactions on Ultrasonics, Ferroelectrics, and Frequency Control*, 56(3):489–506, 2009. doi: 10.1109/TUFFC.2009.1067.

[3] C. Papadacci, M. Pernot, M. Couade, M. Fink, and M. Tanter. High-contrast ultrafast imaging of the heart. *IEEE Transactions on Ultrasonics, Ferroelectrics, and Frequency Control*, 61(2):288–301, 2014. doi: 10.1109/TUFFC.2014.6722614.

[4] B. Denarie, T. A. Tangen, I. K. Ekroll, N. Rolim, H. Torp, T. Bjastad, and L. Lovstakken. Coherent plane wave compounding for very high frame rate ultrasonography of rapidly moving targets. *IEEE Transactions on Medical Imaging*, 32(7):1265–1276, 2013. ISSN 02780062. doi: 10.1109/TMI.2013.2255310.

[5] M. Toulemonde, W. C. Duncan, A. Stanziola, V. Sboros, Y. Li, R. J. Eckersley, S. Lin, M. Tang, and M. Butler. Effects of motion on high frame rate contrast enhanced echocardiography and its correction. In *2017 IEEE International Ultrasonics Symposium (IUS)*, pages 1–4, 2017. doi: 10.1109/ULTSYM.2017.8092362.

[6] A. Stanziola, M. Toulemonde, Y. O. Yildiz, R. J. Eckersley, and M. Tang. Ultrasound imaging with microbubbles [life sciences]. *IEEE Signal Processing Magazine*, 33(2):111–117, 2016. doi: 10.1109/MSP.2015.2496914.

[7] M.-X. Tang and R. J. Eckersley. Nonlinear propagation of ultrasound through microbubble contrast agents and implications for imaging. *IEEE transactions on ultrasonics, ferroelectrics, and frequency control*, 53(12):2406–2415, 2006.

[8] M. Couade, M. Pernot, M. Tanter, E. Messas, A. Bel, M. Ba, A. Hagège, and M. Fink. Ultrafast imaging of the heart using circular wave synthetic imaging with phased arrays. In *2009 IEEE International Ultrasonics Symposium*, pages 515–518, 2009. doi: 10.1109/ULTSYM.2009.5441640.

[9] M. E. Toulemonde, R. Corbett, V. Papadopoulou, N. Chahal, Y. Li, C. H. Leow, D. O. Cosgrove, R. J. Eckersley, N. Duncan, R. Senior, and M.-X. Tang. High frame-rate contrast echocardiography: In-human demonstration. *JACC: Cardiovascular Imaging*, 11(6):923–924, 2018. doi: 10.1016/j.jcmg.2017.09.011. URL https://www.jacc.org/doi/abs/10.1016/j.jcmg.2017.09.011.

[10] A. Stanziola, M. Toulemonde, Y. Li, V. Papadopoulou, R. Corbett, N. Duncan, R. J. Eckersley, and M. X. Tang. Motion Artifacts and Correction in Multi-Pulse High Frame Rate Contrast Enhanced Ultrasound. *IEEE Transactions on Ultrasonics, Ferroelectrics, and Frequency Control*, 2018. ISSN 15258955. doi: 10.1109/TUFFC.2018.2887164.

[11] J. Poree, D. Posada, A. Hodzic, F. Tournoux, G. Cloutier, and D. Garcia. High-Frame-Rate Echocardiography Using Coherent Compounding with Doppler-Based Motion-Compensation. *IEEE Transactions on Medical Imaging*, 35(7):1647–1657, 2016. ISSN 1558254X. doi: 10.1109/TMI.2016.2523346.

[12] T. L. Szabo. *Diagnostic ultrasound imaging: inside out*. Academic Press, 2004.

[13] R. T. Beyer. *Nonlinear acoustics*. US Department of Defense, Department of the Navy, Naval Sea Systems Command, 1974.

[14] F. A. Duck. Nonlinear acoustics in diagnostic ultrasound. *Ultrasound in Medicine & Biology*, 28 (1):1 – 18, 2002. ISSN 0301-5629. doi: https://doi.org/10.1016/S0301-5629(01)00463-X. URL http://www.sciencedirect.com/science/article/pii/S030156290100463X.

[15] A. L. Klibanov and J. A. Hossack. Ultrasound in radiology: From anatomic, functional, molecular imaging to drug delivery and image-guided therapy. *Investigative radiology*, 50(9):657–670, 09 2015. doi: 10.1097/RLI.0000000000000188. URL https://pubmed.ncbi.nlm.nih.gov/26200224.

[16] A. Genc, M. Ryk, M. Suwała, T. Żurakowska, and W. Kosiak. Ultrasound imaging in the general practitioner's office - a literature review. *Journal of ultrasonography*, 16(64):78–86, 03 2016. doi: 10.15557/JoU.2016.0008. URL https://pubmed.ncbi.nlm.nih.gov/27104005.

[17] A. G. Webb. *Introduction to Biomedical Imaging*. John Wiley & Sons, 2002.

[18] P. Hoskins, K. Martin, and a. thrush. *Diagnostic Ultrasound, Third Edition: Physics and Equipment*. Taylor & Francis Group, 05 2019. ISBN 9781138892934.

[19] R. Torguet, C. Bruneel, E. Bridoux, J. M. Rouvaen, and B. Nongaillard. *Ultrafast Echotomographic System Using Optical Processing of Ultrasonic Signals*, pages 79–85. Springer US, Boston, MA, 1977. ISBN 978-1-4757-0653-6. doi: 10.1007/978-1-4757-0653-6_6. URL https://doi.org/10.1007/978-1-4757-0653-6_6.

[20] B. Delannoy, R. Torguet, C. Bruneel, E. Bridoux, J. M. Rouvaen, and H. Lasota. Acoustical image reconstruction in parallel-processing analog electronic systems. *Journal of Applied Physics*, 50(5):3153–3159, 1979. doi: 10.1063/1.326397. URL https://doi.org/10.1063/1.326397.

[21] D. P. Shattuck, M. D. Weinshenker, S. W. Smith, and O. T. von Ramm. Explososcan: A parallel processing technique for high speed ultrasound imaging with linear phased arrays. *The Journal of the Acoustical Society of America*, 75(4):1273–1282, 1984. doi: 10.1121/1.390734. URL https://doi.org/10.1121/1.390734.

[22] M. Tanter, J. Bercoff, A. Athanasiou, T. Deffieux, J.-L. Gennisson, G. Montaldo, M. Muller, A. Tardivon, and M. Fink. Quantitative assessment of breast lesion viscoelasticity: Initial clinical results using supersonic shear imaging. *Ultrasound in Medicine & Biology*, 34(9):1373–1386, 2008. doi: https://doi.org/10.1016/j.ultrasmedbio.2008.02.002. URL http://www.sciencedirect.com/science/article/pii/S0301562908000720.

[23] J. M. Chang, W. K. Moon, N. Cho, A. Yi, H. R. Koo, W. Han, D.-Y. Noh, H.-G. Moon, and S. J. Kim. Clinical application of shear wave elastography (swe) in the diagnosis of benign and malignant breast diseases. *Breast Cancer Research and Treatment*, 129(1):89–97, 2011. doi: 10.1007/s10549-011-1627-7. URL https://doi.org/10.1007/s10549-011-1627-7.

[24] K. Jung and S. Kim. Clinical applications of transient elastography. *Clinical and molecular hepatology*, 18:163–73, 06 2012. doi: 10.3350/cmh.2012.18.2.163.

[25] R. M. S. Sigrist, J. Liau, A. E. Kaffas, M. C. Chammas, and J. K. Willmann. Ultrasound elastography: Review of techniques and clinical applications. *Theranostics*, 7(5):1303–1329, 03 2017. doi: 10.7150/thno.18650. URL https://pubmed.ncbi.nlm.nih.gov/28435467.

[26] L. Sandrin, S. Catheline, M. Tanter, X. Hennequin, and M. Fink. Time-resolved pulsed elastography with ultrafast ultrasonic imaging. *Ultrasonic Imaging*, 21(4):259–272, 1999. doi: 10.1177/016173469902100402. URL https://doi.org/10.1177/016173469902100402. PMID: 10801211.

[27] M. Tanter, J. Bercoff, L. Sandrin, and M. Fink. Ultrafast compound imaging for 2-d motion vector estimation: application to transient elastography. *IEEE Transactions on Ultrasonics, Ferroelectrics, and Frequency Control*, 49(10):1363–1374, 2002. doi: 10.1109/TUFFC.2002.1041078.

[28] W. F. Walker and G. E. Trahey. Real-time synthetic receive aperture imaging: experimental results. In *1994 Proceedings of IEEE Ultrasonics Symposium*, volume 3, pages 1657–1660 vol.3, 1994. doi: 10.1109/ULTSYM.1994.401908.

[29] S. Holm and H. Yao. Improved framerate with synthetic transmit aperture imaging using prefocused subapertures. In *1997 IEEE Ultrasonics Symposium Proceedings. An International Symposium (Cat. No.97CH36118)*, volume 2, pages 1535–1538 vol.2, 1997. doi: 10.1109/ULTSYM.1997.661868.

[30] R. Y. Chiao and L. J. Thomas. Synthetic transmit aperture imaging using orthogonal golay coded excitation. In *2000 IEEE Ultrasonics Symposium. Proceedings. An International Symposium (Cat. No.00CH37121)*, volume 2, pages 1677–1680 vol.2, 2000. doi: 10.1109/ULTSYM.2000.921644.

[31] M. Berson, A. Roncin, and L. Pourcelot. Compound scanning with an electrically steered beam. *Ultrasonic Imaging*, 3(3):303 – 308, 1981. ISSN 0161-7346. doi: https://doi.org/10.1016/0161-7346(81)90162-0. URL http://www.sciencedirect.com/science/article/pii/0161734681901620.

[32] S. K. Jespersen, J. E. Wilhjelm, and H. Sillesen. Multi-angle compound imaging. *Ultrasonic Imaging*, 20(2):81–102, 1998. doi: 10.1177/016173469802000201. URL https://doi.org/10.1177/016173469802000201. PMID: 9691367.

[33] R. R. Entrekin, B. A. Porter, H. H. Sillesen, A. D. Wong, P. L. Cooperberg, and C. H. Fix. Real-time spatial compound imaging: Application to breast, vascular, and musculoskeletal ultrasound. *Seminars in Ultrasound, CT and MRI*, 22(1):50 – 64, 2001. ISSN 0887-2171. doi: https://doi.org/10.1016/S0887-2171(01)90018-6. URL http://www.sciencedirect.com/science/article/pii/S0887217101900186.

[34] Z. Izadifar, P. Babyn, and D. Chapman. Mechanical and biological effects of ultrasound: A review of present knowledge. *Ultrasound in Medicine & Biology*, 43(6):1085 – 1104, 2017. ISSN 0301-5629. doi: https://doi.org/10.1016/j.ultrasmedbio.2017.01.023. URL http://www.sciencedirect.com/science/article/pii/S0301562917300522.

[35] D. Posada, J. Porée, A. Pellissier, B. Chayer, F. Tournoux, G. Cloutier, and D. Garcia. Staggered multiple-prf ultrafast color doppler. *IEEE transactions on medical imaging*, 35, 01 2016. doi: 10.1109/TMI.2016.2518638.

[36] I. Ekroll, M. Voormolen, Ø. Standal, J. Rau, and L. Løvstakken. Coherent compounding in doppler imaging. *Ultrasonics, Ferroelectrics, and Frequency Control, IEEE Transactions on*, 62:1634–1643, 09 2015. doi: 10.1109/TUFFC.2015.007010.

[37] C. Errico, J. Pierre, S. Pezet, Y. Desailly, Z. Lenkei, O. Couture, and M. Tanter. Ultrafast ultrasound localization microscopy for deep super-resolution vascular imaging. *Nature*, 527, 11 2015. doi: 10.1038/nature16066.

[38] J. Zhu, E. M. Rowland, S. Harput, K. Riemer, C. H. Leow, B. Clark, K. Cox, A. Lim, K. Christensen-Jeffries, G. Zhang, et al. 3d super-resolution us imaging of rabbit lymph node vasculature in vivo by using microbubbles. *Radiology*, 291(3):642–650, 2019.

[39] O. Couture, M. Fink, and M. Tanter. Ultrasound contrast plane wave imaging. *IEEE Transactions on Ultrasonics, Ferroelectrics, and Frequency Control*, 59(12):2676–2683, 2012. doi: 10.1109/TUFFC.2012.2508.

[40] M. Correia, J. Provost, S. Chatelin, O. Villemain, M. Tanter, and M. Pernot. Ultrafast harmonic coherent compound (uhcc) imaging for high frame rate echocardiography and shear-wave elastography. *IEEE transactions on ultrasonics, ferroelectrics, and frequency control*, 63(3):420–431, 2016.

[41] A. Athanasiou, A. Tardivon, M. Tanter, B. Sigal-Zafrani, J. Bercoff, T. Deffieux, J.-L. Gennisson, M. Fink, and S. Neuenschwander. Breast lesions: quantitative elastography with supersonic shear imaging—preliminary results. *Radiology*, 256(1):297–303, 2010.

[42] E. Bavu, J.-L. Gennisson, M. Couade, J. Bercoff, V. Mallet, M. Fink, A. Badel, A. Vallet-Pichard, B. Nalpas, M. Tanter, et al. Noninvasive in vivo liver fibrosis evaluation using supersonic shear imaging: a clinical study on 113 hepatitis c virus patients. *Ultrasound in medicine & biology*, 37(9): 1361–1373, 2011.

[43] H. Hasegawa and H. Kanai. High-frame-rate echocardiography using diverging transmit beams and parallel receive beamforming. *Journal of Medical Ultrasonics*, 38(3):129–140, 2011. doi: 10.1007/s10396-011-0304-0. URL `https://doi.org/10.1007/s10396-011-0304-0`.

[44] O. Couture, V. Hingot, B. Heiles, P. Muleki-Seya, and M. Tanter. Ultrasound localization microscopy and super-resolution: A state of the art. *IEEE Transactions on Ultrasonics, Ferroelectrics, and Frequency Control*, 65(8):1304–1320, 2018. doi: 10.1109/TUFFC.2018.2850811.

[45] P. Joos, J. Porée, H. Liebgott, D. Vray, G. Cloutier, B. Nicolas, and D. Garcia. High-frame-rate velocity vector imaging echocardiography: An in vitro evaluation. *IEEE International Ultrasonics Symposium, IUS*, 2016-November, 2016. ISSN 19485727. doi: 10.1109/ULTSYM.2016.7728784.

[46] M. Toulemonde and M. X. Tang. Motion correction for high-frame-rate contrast enhanced echocardiography. *25th European Symposium on Ultrasound Contrast Imaging*, Rotterdam, 16-17 January, 2020.

[47] V. Hingot, C. Errico, M. Tanter, and O. Couture. Subwavelength motion-correction for ultrafast ultrasound localization microscopy. *Ultrasonics*, 77:17–21, 2017. ISSN 0041624X. URL `http://dx.doi.org/10.1016/j.ultras.2017.01.008`.

[48] B. Brekke, L. C. Nilsen, J. Lund, H. Torp, T. Bjastad, B. H. Amundsen, A. Stoylen, and S. A. Aase. Ultra-high frame rate tissue doppler imaging. *Ultrasound in Medicine and Biology*, 40(1):222–231, 2014. ISSN 1879291X. doi: 10.1016/j.ultrasmedbio.2013.09.012.

[49] I. Z. Apostolakis, J. L. Robert, J. Shin, C. Meral, and F. Vignon. Dual Aperture Motion Compensation (DAMoCo). *IEEE International Ultrasonics Symposium, IUS*, 2019-October:2015–2018, 2019. ISSN 19485727. doi: 10.1109/ULTSYM.2019.8926216.

[50] K. L. Gammelmark and J. A. Jensen. 2-D tissue motion compensation of synthetic transmit aperture images. *IEEE Transactions on Ultrasonics, Ferroelectrics, and Frequency Control*, 61(4):594–610, 2014. ISSN 08853010. doi: 10.1109/TUFFC.2014.2948.

[51] L. Nie, D. M. Cowell, T. M. Carpenter, J. R. McLaughlan, A. A. Cubukcu, and S. Freear. High Frame-Rate Contrast-Enhanced Echocardiography using Diverging Waves: 2-D Motion Estimation and Compensation. *IEEE Transactions on Ultrasonics, Ferroelectrics, and Frequency Control*, 66 (2):359–371, 2018. ISSN 15258955. doi: 10.1109/TUFFC.2018.2887224.

[52] S. Harput, K. Christensen-Jeffries, J. Brown, Y. Li, K. J. Williams, A. H. Davies, R. J. Eckersley, C. Dunsby, and M. X. Tang. Two-Stage Motion Correction for Super-Resolution Ultrasound Imaging in Human Lower Limb. *IEEE Transactions on Ultrasonics, Ferroelectrics, and Frequency Control*, 65(5):803–814, 2018. ISSN 08853010. doi: 10.1109/TUFFC.2018.2824846.

[53] S. Bakas, M. Doulgerakis-Kontoudis, G. J. Hunter, P. S. Sidhu, D. Makris, and K. Chatzimichail. Evaluation of Indirect Methods for Motion Compensation in 2-D Focal Liver Lesion Contrast-Enhanced Ultrasound (CEUS)Imaging. *Ultrasound in Medicine and Biology*, 45(6):1380–1396, 2019. ISSN 1879291X. doi: 10.1016/j.ultrasmedbio.2019.01.023.

[54] D. Rueckert. Nonrigid registration using free-form deformations: Application to breast mr images. *IEEE Transactions on Medical Imaging*, 18(8):712–721, 1999. ISSN 02780062. doi: 10.1109/42.796284.

[55] L. Nie, D. M. Cowell, T. M. Carpenter, J. R. McLaughlan, A. A. Cubukcu, and S. Freear. Motion Compensation for High-Frame-Rate Contrast-Enhanced Echocardiography Using Diverging Waves: Image Registration Versus Correlation-Based Method. *IEEE International Ultrasonics Symposium, IUS*, 2019-October:380–383, 2019. ISSN 19485727. doi: 10.1109/ULTSYM.2019.8925638.

[56] B. B. Goldberg, J.-B. Liu, and F. Forsberg. Ultrasound contrast agents: A review. *Ultrasound in Medicine & Biology*, 20(4):319 – 333, 1994. ISSN 0301-5629. doi: https://doi.org/10.1016/0301-5629(94)90001-9. URL http://www.sciencedirect.com/science/article/pii/0301562994900019.

[57] L. Xia. Analysis of acoustic nonlinearity parameter b/a in liquids containing ultrasound contrast agents. *The Journal of the Acoustical Society of America*, 146(2):1394–1403, 2019. doi: 10.1121/1.5123486. URL https://doi.org/10.1121/1.5123486.

[58] J. Wu and J. Tong. Measurements of the nonlinearity parameter ba of contrast agents. *Ultrasound in Medicine & Biology*, 24(1):153 – 159, 1998. ISSN 0301-5629. doi: https://doi.org/10.1016/S0301-5629(97)00207-X. URL http://www.sciencedirect.com/science/article/pii/S030156299700207X.

[59] N. de Jong. *Acoustic properties of ultrasound contrast agents*. (Doctoral dissertation, Erasmus University, Rotterdam, Netherlands), 1993. URL https://repub.eur.nl/.

[60] E. Stride and N. Saffari. Microbubble ultrasound contrast agents: a review. *Proceedings of the Institution of Mechanical Engineers, Part H: Journal of Engineering in Medicine*, 217(6):429–447, 2003.

[61] G. L. Chahine and C.-T. Hsiao. Modeling microbubble dynamics in biomedical applications. *Journal of Hydrodynamics*, 24(2):169–183, 2012.

[62] Q. Wang, K. Manmi, and M. L. Calvisi. Numerical modeling of the 3d dynamics of ultrasound contrast agent microbubbles using the boundary integral method. *Physics of Fluids*, 27(2):022104, 2015. doi: 10.1063/1.4908045. URL https://doi.org/10.1063/1.4908045.

[63] O. Couture, S. Bannouf, G. Montaldo, J.-F. Aubry, M. Fink, and M. Tanter. Ultrafast imaging of ultrasound contrast agents. *Ultrasound in Medicine & Biology*, 35(11):1908 – 1916, 2009. ISSN 0301-5629. doi: https://doi.org/10.1016/j.ultrasmedbio.2009.05.020. URL http://www.sciencedirect.com/science/article/pii/S0301562909002464.

[64] J. Viti, H. J. Vos, N. d. Jong, F. Guidi, and P. Tortoli. Detection of contrast agents: Plane wave versus focused transmission. *IEEE Transactions on Ultrasonics, Ferroelectrics, and Frequency Control*, 63 (2):203–211, 2016. doi: 10.1109/TUFFC.2015.2504546.

[65] J. Zhu, S. Lin, S. Harput, M. Toulemonde, C. H. Leow, and M. Tang. High frame rate contrast enhanced ultrasound imaging of lymphatic vessel phantom. In *2017 IEEE International Ultrasonics Symposium (IUS)*, pages 1–4, 2017. doi: 10.1109/ULTSYM.2017.8092326.

[66] A. Stanziola, M. Toulemonde, Y. Li, V. Papadopoulou, R. Corbett, N. Duncan, R. J. Eckersley, and M. X. Tang. Motion artifacts and correction in multipulse high-frame rate contrast-enhanced ultrasound. *IEEE Transactions on Ultrasonics, Ferroelectrics, and Frequency Control*, 66(2):417–420, 2019. doi: 10.1109/TUFFC.2018.2887164.

[67] M. Toulemonde, W. C. Duncan, C. Leow, V. Sboros, Y. Li, R. J. Eckersley, S. Lin, M. Tang, and M. Butler. Cardiac flow mapping using high frame rate diverging wave contrast enhanced ultrasound and image tracking. In *2017 IEEE International Ultrasonics Symposium (IUS)*, pages 1–4, 2017. doi: 10.1109/ULTSYM.2017.8091924.

[68] B. Treeby, B. Cox, and J. Jaros. *k-Wave User Manual*. Available online at http://www.k-wave.org/manual/k-wave_user_manual_1.1.pdf, 2016.

[69] B. E. Treeby and B. T. Cox. k-wave: Matlab toolbox for the simulation and reconstruction of photoacoustic wave fields. *Journal of biomedical optics*, 15(2):021314, 2010.

[70] B. E. Treeby, J. Jaros, A. P. Rendell, and B. Cox. Modeling nonlinear ultrasound propagation in heterogeneous media with power law absorption using ak-space pseudospectral method. *The Journal of the Acoustical Society of America*, 131(6):4324–4336, 2012.

[71] W. Law, L. Frizzell, and F. Dunn. Determination of the nonlinearity parameter b/a of biological media. *Ultrasound in Medicine & Biology*, 11(2):307 – 318, 1985. ISSN 0301-5629. doi: https://doi.org/10.1016/0301-5629(85)90130-9. URL http://www.sciencedirect.com/science/article/pii/0301562985901309.

[72] R. A. Nishimura, F. A. J. Miller, M. J. Callahan, R. C. Benassi, J. B. Seward, and A. J. Tajik. Doppler echocardiography: theory, instrumentation, technique, and application. *Mayo Clin Proc*, 60(5): 321–343, May 1985. ISSN 0025-6196 (Print); 0025-6196 (Linking). doi: 10.1016/s0025-6196(12)60540-0.

[73] C.-C. Shen, Y.-H. Chou, and P.-C. Li. Pulse inversion techniques in ultrasonic nonlinear imaging. *Journal of Medical Ultrasound*, 13(1):3 – 17, 2005. ISSN 0929-6441. doi: https://doi.org/

10.1016/S0929-6441(09)60073-4. URL http://www.sciencedirect.com/science/article/pii/S0929644109600734.

[74] D. Zwillinger. *CRC standard mathematical tables and formulae*. CRC press, 2002.

[75] R. Eckersley. *Contrast Media, Ultrasound, Amplitude Modulation*, pages 522–522. Springer Berlin Heidelberg, Berlin, Heidelberg, 2008. ISBN 978-3-540-35280-8. doi: 10.1007/978-3-540-35280-8_621. URL https://doi.org/10.1007/978-3-540-35280-8_621.

[76] C. Kasai, K. Namekawa, A. Koyano, and R. Omoto. Real-time two-dimensional blood flow imaging using an autocorrelation technique. *IEEE Transactions on Sonics and Ultrasonics*, 32(3):458–464, 1985. doi: 10.1109/T-SU.1985.31615.

[77] T. Ulrich. Envelope calculation from the hilbert transform. 03 2006.

[78] P. Y. Barthez, R. Léveillé, and P. V. Scrivani. Side lobes and grating lobes artifacts in ultrasound imaging. *Vet Radiol Ultrasound*, 38(5):387–393, Sep-Oct 1997. ISSN 1058-8183 (Print); 1058-8183 (Linking). doi: 10.1111/j.1740-8261.1997.tb02104.x.

[79] V. R. Amin. *Ultrasonic attenuation estimation for tissue characterization*. Digital Repository@ Iowa State University, http://lib. dr. iastate. edu/, 1989.

[80] A. Ng and J. Swanevelder. Resolution in ultrasound imaging. *Continuing Education in Anaesthesia, Critical Care & Pain*, 11:186–192, 09 2011. doi: 10.1093/bjaceaccp/mkr030.

[81] M.-X. Tang, H. Mulvana, T. Gauthier, A. Lim, D. Cosgrove, R. Eckersley, and E. Stride. Quantitative contrast-enhanced ultrasound imaging: a review of sources of variability. *Interface focus*, 1(4): 520–539, 2011.

[82] T. Loupas, J. Powers, and R. Gill. An axial velocity estimator for ultrasound blood-flow imaging, based on a full evaluation of the doppler equation by means of a 2-dimensional autocorrelation approach. *Ultrasonics, Ferroelectrics and Frequency Control, IEEE Transactions on*, 42:672 – 688, 08 1995. doi: 10.1109/58.393110.

[83] L. Husmann, S. Leschka, L. Desbiolles, T. Schepis, O. Gaemperli, B. Seifert, P. Cattin, T. Frauenfelder, T. G. Flohr, B. Marincek, P. A. Kaufmann, and H. Alkadhi. Coronary artery motion and cardiac phases: dependency on heart rate – implications for ct image reconstruction. *Radiology*, 245(2):567–576, Nov 2007. ISSN 0033-8419 (Print); 0033-8419 (Linking). doi: 10.1148/radiol.2451061791.

Appendix A

Additional material on acoustic wave physics

A.1 Pressure fields as solutions to the wave equation

In section 2.1 the relationship between a pressure field and a corresponding velocity potential was introduced. This relationship is reintroduced here, as a repetition of equation 2.3:

$$p = -\rho \frac{\partial \phi}{\partial t} \tag{A.1}$$

We can rewrite this equation in terms of the velocity potential, ϕ, in the following way:

$$\phi(t, \mathbf{x}) = -\frac{1}{\rho} \int_0^t p(t, \mathbf{x})\, dt$$

Introducing this result into equation 2.1 we obtain:

$$\nabla^2 \left(-\frac{1}{\rho} \int_0^t p(t, \mathbf{x})\, dt \right) - \frac{1}{c^2} \frac{\partial^2}{\partial t^2} \left(-\frac{1}{\rho} \int_0^t p(t, \mathbf{x})\, dt \right) = 0$$

Because the integration limits do not depend on the space coordinates, the double gradient can be evaluated inside the integral. Furthermore, one of the derivatives in time cancels the second pressure integral to obtain:

$$-\frac{1}{\rho} \int_0^t \nabla^2 p(t, \mathbf{x})\, dt + \frac{1}{\rho c^2} \frac{\partial p(t, \mathbf{x})}{\partial t} = 0$$

If we now perform a time differentiation on both sides and multiply the equation by a factor of $-\rho$ we achieve our final result:

$$\nabla^2 p - \frac{1}{c^2} \frac{\partial^2 p}{\partial t^2} = 0$$

Which is precisely the wave equation as presented in 2.1 and where the time and space dependence on the pressure has been made implicit.

This result proves that if velocity potentials solve the wave equation, then their corresponding pressure fields also solve it.

Appendix B

Additional material on signal processing

B.1 The analytic signal, Hilbert transform and I/Q demodulation

The analytic signal was introduced in equation 3.61 and its expression is reintroduced here:

$$\hat{s}(t) = s(t) - j\breve{s}(t) \tag{B.1}$$

Where $\breve{s}(t)$ is the Hilbert transform of $s(t)$. The Hilbert transform is defined as:

$$\breve{s}(t) = \mathcal{H}\{r(t)\} = -\frac{1}{\pi t} * r(t) = -\frac{1}{\pi}\int_{-\infty}^{\infty}\frac{r(\tau)}{t-\tau}\mathrm{d}\tau \tag{B.2}$$

An interesting property of the Hilbert transform is that it inverts the sign of the negative part of the frequency domain of the signal it is applied to, as well as multiplying it by a factor of j. In other words, if we define $R(\omega)$ to be the Fourier transform of $r(t)$, the following is true:

$$\mathcal{F}\{\mathcal{H}\{r(t)\}\} = j\,\mathrm{sgn}(\omega)R(\omega) = \begin{cases} jR(\omega) & \omega \geq 0 \\ -jR(\omega) & \omega < 0 \end{cases} \tag{B.3}$$

The Fourier transform of the analytic signal, as given by equation 3.61 is thus:

$$\begin{aligned} \mathcal{F}\{\hat{r}(t)\} &= \mathcal{F}\{r(t)\} - j\mathcal{F}\{\breve{r}(t)\} \\ &= \begin{cases} R(\omega) - j^2R(\omega) & \omega \geq 0 \\ R(\omega) + j^2R(\omega) & \omega < 0 \end{cases} \\ &= \begin{cases} 2R(\omega) & \omega \geq 0 \\ 0 & \omega < 0 \end{cases} \end{aligned} \tag{B.4}$$

The analytic signal of $r(t)$, seen in the frequency domain, is equivalent to turning to zero all the

negative frequency components of its Fourier transform while doubling the positive frequency ones.

I/Q demodulated signals are a type of analytic signal, verifying the same properties in the frequency domain. I/Q demodulation can be performed by first downmixing the RF signal at the carrier frequency, shifting the positive frequency content of the band towards zero, followed by low-pass filtering at the same frequency to eliminate the negative frequency components that were shifted by the same amount. Given a carrier frequency f_0, I/Q demodulation of a real signal $s(t)$ is computed as:

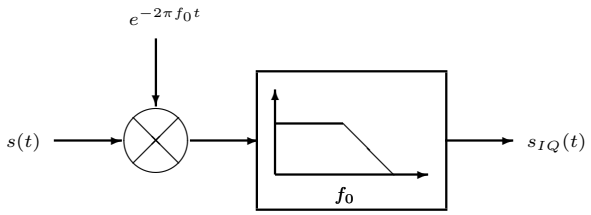

Figure B.1: The process of I/Q demodulation. Downmixing at the carrier frequency is followed by lowpass filtering at the same frequency

B.2 Parity of magnitude and argument of even complex functions

Let $s(t) : \mathbb{R}_0^+ \to \mathbb{C}$ be an even function of time:

$$s(t) = s(-t)^* \tag{B.5}$$

The polar form of $s(t)$ is given by the following equation:

$$s(t) = \rho(t)e^{j\phi(t)},\ \rho(t) = \sqrt{\mathrm{Re}\{r(t)\}^2 + \mathrm{Im}\{r(t)\}^2},\ \phi(t) = \arctan\frac{\mathrm{Im}\{r(t)\}}{\mathrm{Re}\{r(t)\}} \tag{B.6}$$

where both $\rho(t)$ and $\phi(t)$ are, by definition, real equations of time. We now expand equation B.5 using the polar form of $s(t)$ in equation B.6:

$$\begin{aligned} s(t) &= s^*(-t) \\ \rho(t)e^{j\phi(t)} &= \rho^*(-t)\left(e^{j\phi(-t)}\right)^* \\ \rho(t)e^{j\phi(t)} &= \rho(-t)e^{-j\phi(-t)} \end{aligned} \tag{B.7}$$

where on the last step the complex conjugate of $\rho(-t)$ was omitted because ρ is real-valued. The evenness of $s(t)$ imposes the following relations on its magnitude and phase:

$$\rho(t) = \rho(-t) \tag{B.8}$$

$$\phi(t) = -\phi(-t) \tag{B.9}$$

Relations B.8 and B.9 are precisely the definitions of real-valued even and odd functions, respectively. In conclusion, an even complex-valued function necessarily has even magnitude and odd argument.